学位論文

Investigation of Interstellar Dust Emission in the Infrared-Microwave Range with All-sky Surveys

(全天サーベイによる赤外線マイクロ波帯での星間ダスト放射の研究)

平成29年12月博士(理学)申請

東京大学大学院理学系研究科天文学専攻

ベル アーロン クリストファー

Bell, Aaron Christopher

Contents

List of Figures

Abstract

The anomalous microwave emission (AME) still lacks a conclusive explanation. This excess of emission, roughly between 10 and 50 GHz, tends to defy attempts to explain it as synchrotron or free-free emission. The overlap with frequencies important for cosmic microwae background explorations, combined with a strong correlation with interstellar dust, drive cross-disciplinary collaboration between interstellar medium and obervational cosmology. The apparent relationship with dust has prompted a "spinning dust" hypothesis: electric dipole emission by rapidly rotating, small dust grains. Magnetic dipole emission by grains with magnetic inclusions ("magnetic dust"), while less suppported, has not been ruled out. Even assuming a spinning dust scenario, we are far from concluding which category of dust contributes. The typical peak frequency range of the AME profile implicates grains on the order of 1nm. This points to polycyclic aromatic hydrocarbon molecules (PAHs). We use data from the AKARI/Infrared Camera (IRC; Onaka et al. (2007)), due to its thorough PAH-band coverage, to compare AME from the Planck Collaboration et al. (2016b). astrophysical component separation product) with infrared dust emission. We look also at infrared dust emission from other mid IR and far-IR bands. The results and discussion contained here apply to an angular scale of approximately $1°$. In general, our results support an AME-from-dust hypothesis. We look both at λ Orionis, a region highlighted for strong AME, and find that certainly dust mass correlates with AME, and that PAH-related emission in the AKARI/IRC 9 μm band may correlate slightly more strongly. These results are compared to an all-sky analysis, where we find that potential microwave emission component separation imperfections among other issues, make an all-sky, delocalized comparsion very challenging. In any case the AME-to-dust correlation persists even in the all-sky case, but tests of relative variations from different dust SED components are largely inconclusive. We emphasize that future efforts to understand AME should focus on individual regions, and a detailed comparsion of the PAH features with the variation of the AME SED. Further all-sky analyses seem unlikely to help resolve this issue. Non-PAH carriers

of the AME, such as nanosilicates, cannot be ruled out either.

IRC

Chapter 1

Introduction

"It is now plain that about 75% of the data we would like to have can be obtained from good ground-based sites"

-H. Johnson, 1966

1.1   All-sky Astronomy

All-sky astronomy is not new. Indeed, the notion of capturing a particular "object" or "source" with a camera and saving it for later investigation would be completely alien to the first astronomers and astronavigators. Absence of telescopes forced us to describe the sky in terms of its larger patterns, brightest characters. What is new however is the notion of preparing an archive of the sky itself for not only the research whims of a single investigator, team, institute, or even a single nation— rather, all-sky surveys tend to be international endeavors in their production, and even more so in their utilization.

1.2   Infrared astronomy

Infrared astronomy was essentially non-existant as recently as the 1920s, if we judge by the first IR observations (Pettit & Nicholson 1922, 1928). Mainstream IR astronomy is perhaps much younger, only really taking off — literally — in the post-war era, via ballon and rocket borne experiments (Johnson 1966). Compare this to visible wavelengths, a field so old we name it after the bio-evolutionary advent of sight, itself. Even radio astronomy with its own logistical and technological challenges, has been around since at least 1932.

Astronomers have not been content to be constrained by atmospheric IR windows, even

TABLE 1.1 Timeline of all-sky surveys

Year	Survey	Reference
1983	IRAS	Neugebauer et al. (1984)
1989	COBE	Boggess et al. (1992)
1990	ROSAT	Truemper (1982)
2001	WMAP	Bennett et al. (2003b)
2003	2MASS	Skrutskie et al. (2006)
2003	GALEX	Martin et al. (2005)
2006	AKARI	Murakami et al. (2007)
2008	Fermi	Atwood et al. (2009)
2009	Planck	Planck Collaboration et al. (2011a)
2009	WISE	Wright et al. (2010)

from the best of ground-based sites. Or perhaps interests have shifted so dramatically since 1966, that all of the investigations enabled by rocket-based, space-based, even Boeing 747-based IR astronomy (e.g. SOFIA, the Stratospheric Observatory for Inrared Astornomy, Young et al. (2012)) would have bored 75% of astronomers in the '60s. The meaning of "far infrared" has even redshifted, so to speak, from the Johnson (1966) definition of "4 to 22 μm" — consider the "Far Infrared Surveyor" instrument onboard the AKARI satellite (Murakami et al. 2007), which observed from 50 to 180 μm (Kawada et al. 2007a)

For our purposes, we consider the far infrared (FIR) to cover 60 to 550 μm, partially out of convenience- FIR bands, in this paper, means the Infrared Astronomical Satellite (IRAS) 60 and 100 μm (Neugebauer et al. 1984), all four FIS bands, and the Planck Observatory's High Frequency Instrument (HFI) 857 GHz and 545 GHz bands (Planck Collaboration et al. 2011a, 2014b). The two AKARI IRC (Onaka et al. 2007; Ishihara et al. 2010) bands and the IRAS 12 and 25 μm bands we will refer to collectively as the MIR bands.

1.3   Multi-wavelength investigations

The ability to map and archive the sky with satellites – not only in the optical and infrared, but well into the microwave regime – has enabled interdisciplinary research of the interstellar medium (ISM). The ISM pervades the galaxy and either surrounds or intervenes basically any object one may wish to study. The ISM is enriched as matter is processed and flows back into space. We can describe the ISM as a mixture of gas and dust. An early estimate by Knapp &

Kerr (1974) puts the mass of dust in the galaxy at about 1% that of interstellar gas.

A wealth of data is now available not only in the IR, but on into the sub-millimeter range and the interpretation of this data has become a serious priority. This is especially true for the last ten years as new, much higher resolution surveys have been carried out such as the Spitzer Space Telescope (SST) Werner et al. (2004), Herschel Space Observatory (Herschel) (Pilbratt et al. 2010) by National Aeronautics and Space Administration (NASA) and the European Space Agency (ESA) respectively, and the AKARI telescope (Murakami et al. 2007), by JAXA. AKARI especially, produced a wealth of data spanning the entire sky. It was equipped with IRC (Onaka et al. 2007) to study the MIR, and FIS (Kawada et al. 2007b) to study cooler dust and gas, and conduct spectroscopy in the FIR via its Fourier Transform Spectrometer (FTS). In this thesis we use these AKARI surveys in a comparison with other cutting edge all-sky maps from the Planck Observatory in a multi-wavelength study of yet another part of the ISM puzzle, the AME and its connection to interstellar dust.

The merits of multiwavelength based investigations arise from the simple fact that the ISM is very complex— both in terms of the myriad forms of matter present, from plasmas to dust grains — and in countless physical processes at play. Consider the complex case of a supernova remnant influencing surrounding ISM: through a combined analysis of radio, mid-far infrared, and X-ray data, Lau et al. (2015) were able to characterize the history of dust production, heating, and destruction within the Sgr A East supernova remnant.

1.4 Interstellar Dust

The study of interstellar dust has been connected to mainstream astrophysics research, and recognized as an integral player in the evolution of the interstellar medium. This has been shown by early sounding rocket experiments (Wolstencroft & Rose 1967; Soifer et al. 1971), and balloon experiments (Muehlner & Weiss 1970; Emerson et al. 1973), and dust has been more profoundly exposed by the advent of all-sky infrared surveys like the Cosmic Background Explorer (COBE)'s Diffuse Infrared Background Experiment (DIRBE) (Sodroski et al. 1994) and IRAS (Neugebauer et al. 1984). With space-borne long-term IR mapping finally available on an all-sky scale, we could move past the interplanetary medium and into the interstellar.

The role of dust in the interstellar medium has expanded beyond simply an intervening,

stellar light obstructing material. Theoretical models and observations have shown that dust grains act as a catalyst for the formation of molecular hydrogen and other molecules, providing a substrate upon which hydrogen and other atoms can meet (Iglesias 1977; Burke & Hollenbach 1983). With infrared observations we are able to study dust directly via its vibrational emission, rather than relying only on inference from visible reddening and polarization effects (Davis & Greenstein 1951; Platt 1956; Carrasco et al. 1973). The question of the composition of dust has grown from a single thread of investigation into a network of questions. Many pieces in this dusty puzzle are missing. For example, the presence of dust grains containing silicates, and amorphous carbon is very strongly supported by comparisons of infrared spectroscopy with laboratory studies (Hagen et al. 1979; Joblin et al. 2009). But many questions remain about which silicate and carbonaceous species may be present, and in what proportions, and in what distribution of sizes. The question also remains, is there more to dust than simply carbonaceous and silicate grains? The exact size distribution of dust grains is also an open question. The composition of extremely small grains / large molecules is a particularly challenging mystery, as well as the role of interstellar ices in the evolution dust and gas.

1.4.1 Silicate grains

One of the first materials proposed to exist as interstellar dust were silicates, with the first evidence being UV absorption features (Knacke et al. 1969). More recently, specific species of silicates are being identified via absorption spectroscopy (Olofsson et al. 2012). However some doubt has been cast recently on the structure of the grains. For example, in Jones et al. (2013) and Jones (2014) an updated model is proposed wherein dust grains may be composed of a mixture of silicate and amorphous carbon material, such as a silicate core with an amorphous carbon envelope, representing the first comprehensive model of continuous grain evolution. In other words, the first model to consider dust grain morphology beyond the discrete categories of silicate grains, carbonaceous grains, and PAH. An additional feature of this model is that silicates having iron inclusions are expected, which would be similar to the Fe form of olivine. This is an update from the conventional "astronomical silicates" assumed in earlier dust SED models such as Li & Draine (2001) or Compiègne et al. (2011).

1.4.2   Carbonaceous grains

As with silicates, the existance well-established that carbonaceous material, primarily amorphous carbon, exists in the ISM (Aitken 1981; Tielens & Allamandola 1987). This is material commonly called "soot" or the fuel we know on earth as coal. Some non-amorphous carbonaceous material is also speculated to exist, such as graphite (Zhou et al. 2006) or "buckyonions" (concentric-shell-graphite) (Li et al. 2008).

1.4.3   Polycyclic Aromatic Hydrocarbons and the Unidentified Infrared Bands

From the mid-to-near IR however, spectroscopic observations enabled and required the simple two-populations model of larger and smaller dust (e.g. Mathis et al. (1977)), to be expanded. "Unidentified IR bands" from 3 to 11 μm (hereafter, UIR bands), demonstrate another divergence from the canonical dust emission story. The UIR bands were first reported at 8 to 13 μm in planetary nebulae and HII regions by Gillett et al. (1973, 1975) in ground-based observations. Observations by Merrill et al. (1975) noted another unexplained feature at 3.27 μm, noting: "there are [...] similarities in the 8-13 μm spectra of NGC 253, NGC 7027, and BD +30°3639 Gillett et al. (1975)". Features at 6.2 and 7.7 μm were reported by Russell et al. (1977) using the first airplane-mounted IR telescope and predecessor to SOFIA, the Kuiper Airborne Observatory. Sellgren et al. (1983) reported features at 3.3 and 3.4 μm being detected in reflection nebulae.

Moving into the 1990s, the UIR bands become much less of property of select objects in targeted observations, are seen observed throughout the Milky Way. Balloon-based observation by Giard et al. (1994) confirmed that the 3.3 μm feature pervades throughout the Galactic plane. The first-ever airborne IR observatory, Kuiper Several years later, space-based spectroscopy with the Infrared Telescope in Space (IRTS)(Murakami et al. 1996) and Infrared Space Observatory (ISO)(Kessler et al. 1996) enabled confirmation by Onaka et al. (1996) and Mattila et al. (1996) that the mid-infrared UIR features are not limited to a few objects, but are present even in the diffuse galactic ISM. Dwek et al. (1997) even reported that photometric excess in the COBE/DIRBE 12 μm band may be caused by the UIR bands, in and suggested they may be from these UIR features have come to be explained via PAH, a possibility which had been con-

sidered earlier by Allamandola et al. (1985); Puget et al. (1985). PAHs are a class of molecules composed primarily of fused carbon rings such as corranulene. PAHs and/or similar amalgems containing aromatic structures (e.g. quenched carbonaceous composites (QCCs), Sakata et al. (1984)) have been incorporated into dust mixture SED models over the last two decades (Draine & Li 2001, 2007a; Hony et al. 2001; Compiègne et al. 2011; Galliano et al. 2011; Jones et al. 2013, 2017).

With the appearance of high powered computers with an ability to perform rigorous calculations, many attempts have been made to simulate the expected emission from PAHs. Density functional theory (DFT) (Hohenberg & Kohn 1964) has become available as a tool for simulating molecular emission features using a quantum approach. DFT calculations has become a subfield of ISM astrophysics. Many attempts are being made to fit particular emission features of PAHs, and other molecular and grain species, to observed ISM features (Hammonds et al. 2009; Hirata et al. 1999). While it is difficult to reproduce the exact interstellar conditions in a laboratory setting, DFT simulations have yielded some evidence that the UIR bands can be explained as PAH vibrational emission features (Pathak & Rastogi 2005; Ricca et al. 2011; Yu & Nyman 2012).

"PAH" or "UIR"? We should note however that PAHs are not the only proposed explanation for the UIR features, despite being the most widely accepted. Zhang & Kwok (2014) propsed theoretically that mixtures of non-PAH carbonaceous and silicate spectra could also fit theoretically calculated PAH emission features. However the PAH-UIR hypothesis is still widely supported (Tielens 2008; Rastogi et al. 2013). The way that PAHs might be produced or evolve from other species is not understood however. Though there are efforts underway to model potential formation pathways. As far as the evolution of larger aromatics form smaller PAHs, there is one proposed pathway wherein a benzene could grow into a larger aromatic molecule such as naphthalene (Ghesquière et al. 2014). In any case, the terms "PAH features" and "UIRs" are too often used interchangably in the literature. In the following sections, we will define PAHs as the general class of aromatic-ring-containing molecules, and not explicitly to "pure" PAH species such as benzene, corronene, or corranulene, etc. From this point we will also abandon the term "UIRs", and use "PAH features" instead. We do so while acknowledging that interstellar PAHs is by no means a closed book.

1.4.4 Metrics of Interstellar Dust

Carefully describing or parameterizing the SED of interstellar dust emission can be somewhat involved. Over the years a few conventions have arisen, when referring to dust SED properties.

Interstellar Radiation Field U Throughout this work we will discuss the ISRF in terms of U, which is a conventional measure normalized to the ISRF of the solar neighborhood. In otherwords, a U of 1 indicates a "Habing unit", or $1.6 \times 10^{-3} erg s^{-1} cm^{-2}$, a value given by Habing (1968). More correctly, U is referring to the integration of the ISRF flux density from the far-UV to the nearIR, or $\lambda = 0.09$ to $\lambda = 0.8$. The ISRF is sometimes indicated in the literature as G_0, instead of U, when integrated only from ~0.09 μm to 0.2μm. As long as we are assuming a spatially constant SED for the ISRF, it is not so important which one we use, and does not affect the results or discusison in this thesis. U will be used in the following chapters, except when referring to previous works which used G_0.

Total dust abundance This is the total mass of all dust components contributing to the observed SED. It is often indicated either as the dust mass M_{dust}, in units of $M_\odot$, as in Galliano et al. (2008). The dust abundance can be determined when both the luminosity of the dust, and the local interstellar radiation field heating the dust, U are known, as in the following relation:

$$M_{dust} \propto L_{dust}/U \tag{1.4.1}$$

Some caution must be excercised, as M_{dust} may sometimes indicated only the mass of dust which is emitting thermall, in the FIR, excluding VSGs or PAHs. Throughout this thesis however, we consider that M_{dust} includes emisison from both the thermal equilibirum grains, and small stochastically emitting dust and PAHs.

PAH Fraction $qPAH$ $qPAH$, sometimes indicated as χ_{PAH}, is defined as the fraction of the total dust mass which is in the form of PAHs, or:

$$qPAH = \frac{M_{PAH}}{M_{dust}} \tag{1.4.2}$$

This parameter can be especially difficult to fit, relative to the total dust mass, for the reason that there a many more all-sky photometric data points in the far infrared, where thermal emission from dust grains dominates. In the mid infrared, where PAH features are observed, we have fewer observational constraints on an all-sky basis. This is discussed further in Ch. 2.

PAH Ionization Fraction $fPAH$ $fPAH$ tells us the fraction of the total PAH mass which are ionized. Thus:

$$fPAH = \frac{M_{PAHion}}{M_{PAH}} \tag{1.4.3}$$

1.5   Microwave foregrounds

Moving on from the infrared dust SED, into the Rayleigh-Jeans regime of thermal dust emission, multi-wavelength observations have opened up a new discipline: the disentagnlement of interstellar dust emission from non-dust emission components. Most notably, separating temperature fluctuations in the cosmic microwae background (CMB) from the microwave extent of thermal dust emission. Those studying the Milky Way itself, from the far IR into microwave and radio frequencies, are now collaborating closely with those interested in the precise nature of the CMB.

Much of the motivation between recent galactic microwave emission research has little to do with galactic ISM astronomy itself. Rather, our galaxy presents an inconvenience to observational cosmology in that it 'contaminates' observations of the CMB. The avereage SED of the CMB is simple enough to model, with a 2.725 K blackbody function. This temperature however means that the peak occurs between several microwave foreground components, from interstellar dust and gas, as displayed in Fig. 1.1. The difficulty of decomposing the microwave sky into galactic ISM, extragalactic, and CMB temperature fluctuation components has brought the detailed decomposition of the microwave-radio regime of ISM to the forefront of Planck Collaboration paper titles (Planck Collaboration et al. 2011a, 2014a, 2016a). Without extragalactic research, there would be no need for the word "foreground" in describing galactic microwave emission.

The ISM has intruded into cosmological studies perhaps most prominently with the first claimed detection of B-mode polarization (Hanson et al. 2013; BICEP2 Collaboration et al. 2014; Flauger et al. 2014), and multiple response papers. The main consensus being that the

validation of CMB-related claims require a careful estimate of the contribution, in intensity and polarization, from interstellar dust and the subsequent counter-claim that this detection arose from galactic dust(Planck Collaboration et al. 2017; Sheehy & Slosar 2017). More recently AMI Consortium et al. (2012) had noted a peculiar Sunyaev-Zeldovich effect based galaxy cluster detection, AMI-CL J0300+2613. Perrott et al. (2018) have since proposed that this may in fact arise from high galactic latitude dust via AME.

1.6 Anomalous Microwave Emission

In our efforts to decompose and understand galactic microwave emission itself, there remains a constant antagonist. Galactic foregrounds had been broken down into 3 dominant components: free-free emission from ionized regions, synchrotron emission generated by relativistic electrons moving around the Milky Way's magnetic field, and the microwave extent of thermal dust emission (Bennett et al. 2003a; Leach et al. 2008; Planck Collaboration et al. 2014c). Deviations from this understanding began to appear in the early 1990s, with efforts by Kogut et al. (1996); Leitch et al. (1997) to carefully investigate the CMB. They had found a component of the microwave sky which implied unlikely spectral indices for free-free or synchrotron emission. AME generally takes the form of an 'excess' continnuum emission source, having a peak somewhere between 10 to 40 GHz (see Fig. 1.1). This excess defies predictions for known microwave emission mechansisms. AME still lacks a concrete physical explanation. Also, the term itself can be a bit confusing, as the word "anomalous" tends to imply localized outlier. The AME is shown to be more than an isolated anomaly, but an added component of microwave emission appearing throughout the galaxy (de Oliveira-Costa et al. 1997; Bennett et al. 2003a; Dickinson et al. 2013). Fig 1.2 shows two prominent AME regions, ρ Ophiuchus and the Persues Molecular Cloud investigated by Tibbs et al. (2011); Planck Collaboration et al. (2011b), as they appear in AKARI/IRC 9μm all-sky map (Ishihara et al. 2010). In this section we will explain that while there is indeed much mystery as to the exact mechanism(s) producing the AME, what causes its spectral variations, and what might be its physical carrier(s) - it is by now, perhaps less than anomalous. Following subsections will discuss the history of AME and the produced physical explanations, as well comparisons between the AME and infarred emission from interstellar dust.
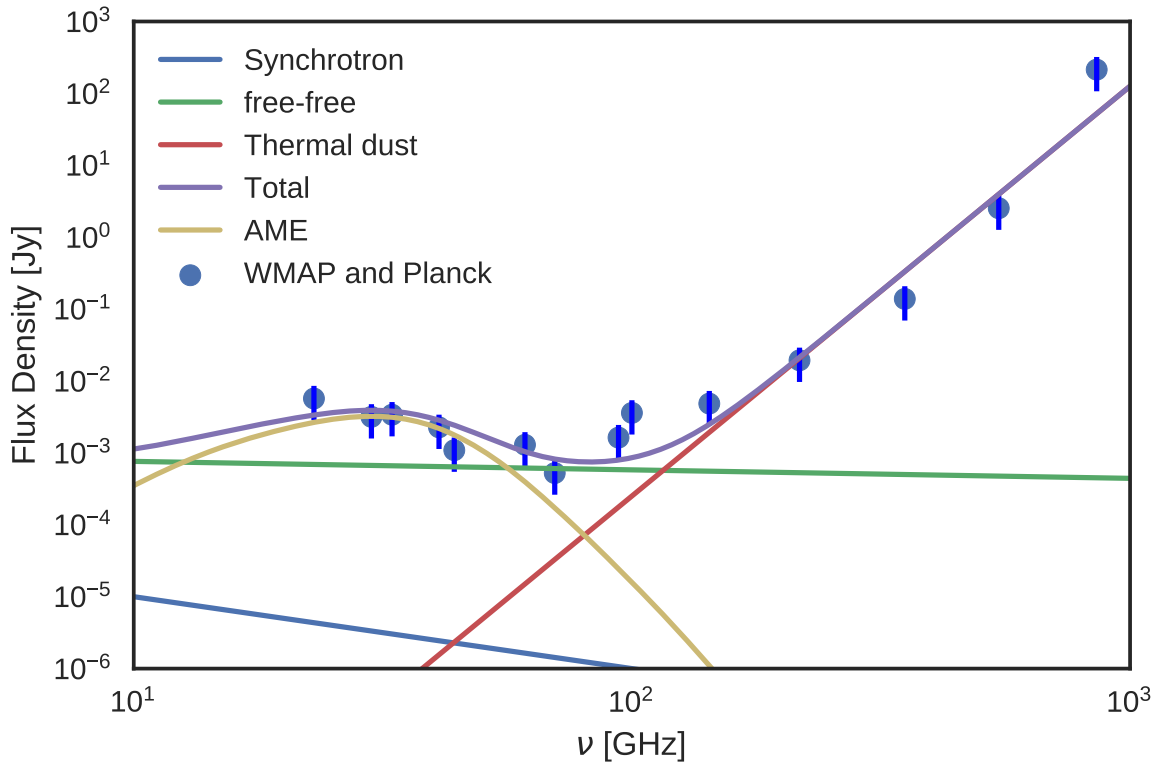
Figure 1.1: An example of a potential makeup of microwave emission components. Photometry points are extracted from the Planck and WMAP all-sky maps (Planck Collaboration et al. 2014b), for a part of the region well-known for prominant AME, ρ Ophiuchus (Planck Collaboration et al. 2011b). The AME curve is produced from a warm neutral medium spinning dust template (Ali-Haïmoud et al. 2009), with a frequency-shift applied to approximately fit the microwave data in Planck Collaboration et al. (2016b)
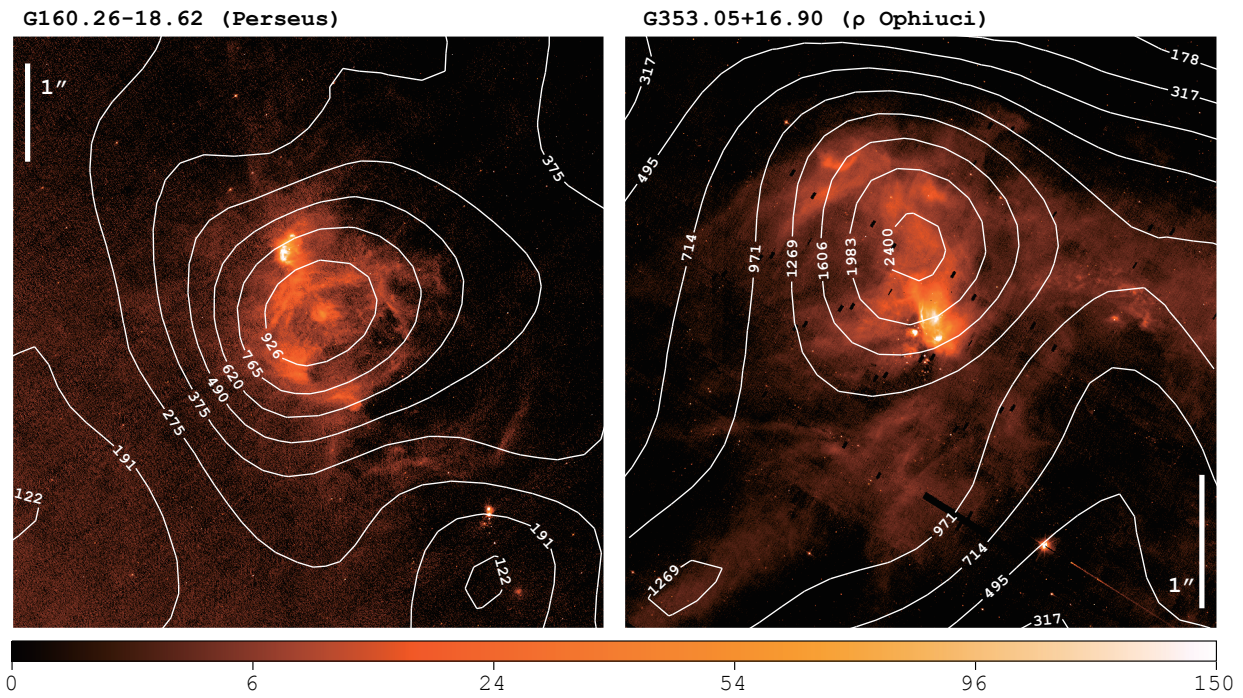
Figure 1.2: Two AME prominent regions investigated by Planck Collaboration et al. (2011b); Tibbs et al. (2011), ρ Ophiuchus and Perseus, as they appear in the PAH-feature-tracing AKARI/IRC 9μm all-sky data at native resolution (Ishihara et al. 2010). White contours show AME at 1° resolution, extracted from the map by Planck Collaboration et al. (2016b). The IRC data shown here is of a much finer resolution than the AME data, at around 10", demonstrating the critical gap in resolvability of all-sky AME-tracing data itself vs. the IR dust tracers we hope to compare it to.

1.6.1 Correlation with dust

Since its first detection in early microwave observations, AME has been found to be a widespread feature of the microwave Milky Way (see the review Dickinson et al. (2013), and an updated state-of-play of AME research by Dickinson et al. (2018). Kogut et al. (1996); de Oliveira-Costa et al. (1997) showed that the AME correlates very well with infrared emission from dust, via COBE/DIRBE and IRAS FIR. Finkbeiner et al. (2002) reported the first detection of a "rising spectrum source at 8 to 10 GHz" in an observation targeting galactic ISM cloud. de Oliveira-Costa et al. (2002) furher argued that this emission is in fact "ubiquitous". The exact mechanism and carrier/s remain mysterious however. More recent works, employing observations by the Wilkinson Microwave Anisotropy Probe (WMAP), SST, the latest infrared (IR) to microwave all-sky maps by Planck, and various ground based radio observations have strongly confirmed a relationship between interstellar dust emission and AME (Ysard & Verstraete 2010; Tibbs et al. 2011; Hensley et al. 2016). Exactly which physical mechanisms produces the AME however is still an open question, even if we assume a dusty AME origin. We equally puzzled as to the chemical composition and morphology of the carrier(s). We also lack an all-sky constraint on the emissivity of the AME spectrum at frequencies short of the WMAP cut-off, around 23 GHz. The typical peak frequency of AME, in those cases where it is constrained, does give us a clue.

1.6.2 Proposed explanations

From the observed spatial correlation between AME and dust emerged two prevailing hypotheses:

1) Electric dipole emission by spinning small dust grains, a mechanism proposed in Erickson (1957) and Hoyle & Wickramasinghe (1970), with further discussion in Ferrara & Dettmar (1994). Draine & Lazarian (1998b) give the earliest thorough theoretical prediction of a spinning dust spectrum. A decade later Ali-Haïmoud et al. (2009) contributed substantial updates, expanded modeling of grain excitation mechanisms and adoption of an updated grain size distribution by Weingartner & Draine (2001). Ysard & Verstraete (2010) introduced the first model of a spinning dust spectrum based on rotational emission from PAH, which are implicated due to their size. Draine & Lazarian (1998b), gives the expected rotational frequency of spinning

dust oscillators ω, as follows:

$$\frac{\omega_T}{2\pi} = \langle\nu^2\rangle^{1/2} \approx 5.60 \times 10^9 a_{-7}^{-5/2}\xi^{-1/2}T_2^{1/2} \quad \text{Hz}, \tag{1.6.1}$$

where T is the gas temperature, a is the grain size, and ξ represents the deviation from a spherical moment of intertia. For example, we can take a typical peak frequency of the AME of ~20 GHz, a gas temperature of 100 K, roughly spherical grains, and a dipole moment on the order of 1 debye, and get:

$$\frac{\omega_T}{2\pi} = 20 \; GHz(\frac{T}{100K})^{1/2}(\frac{\rho}{3gcm^{03}})^{-1/2}(\frac{a}{5\text{Å}})^{-5/2} \tag{1.6.2}$$

implying an oscillator size of approximately 1 nm. Thus PAHs, as considered by Ysard & Verstraete (2010), are a primary candidate spinning dust carrier, due to their expected size range.

2) Magnetic dipole emission, caused by thermal fluctuations in grains with magnetic inclusions, proposed by Draine & Lazarian (1999). More recently, modeled spectra for potential candidate carriers have appeared in the literature: PAHs, grains with magnetic inclusions (Draine & Hensley 2013; Ali-Haïmoud 2014; Hoang et al. 2016).

3) Though not widely accepted, another possible explanation for AME is discussed in Jones (2009). They have suggested that the emissivity of dust, in the spectral range related to AME, could contain features caused by low temperature solid-state structural transitions.

1.6.3 Spinning dust

Spinning dust need not be the only emission mechanism, a convention as arisen in AME observational works. The photometric signature of the AME is frequently interepreted via spinning dust parameters (Ysard et al. 2011; Ali-Haimoud 2010). Archival all-sky AME data products exclusively assume a spinning dust SED templates. Both WMAP and Planck used a base template with 30 GHz peak frequency, and an assumed cold neutral medium environment. Using the "spdust" spinning dust SED model code to fit excess microwave foreground emission has become analagous fitting a modified blackbody function to the FIR.

We explore the case that the AME signature arises from spinning dust emission. If the AME is carried by spinning dust, the carrier should be small enough that it can be rotationally

excited to frequencies in the range of 10-40 GHz, and must have a permanent electric dipole. Within contemporary dust SED models, only the PAH family of molecules, or nanoscale amorphous carbon dust fit these criteria. Those PAHs which have a permanent electric dipole (i.e. coranulene, but not symmetric molecules like coronene), can emit rotationally. However the carrier need not be carbon-based.

1.6.4 Spinning PAHs?

Assuming the rotational emission model of Draine & Lazarian (1998b), the AME signature (consistent with peaked, continuum emission having a peak between 15 and 50 GHz) implies very small oscillators (~1 nm).

In any case, the PAH class of molecules are the only spinning dust candidate so far which show both:

1) Evidence of abundance in the ISM at IR wavelengths, and

2) A predicted range of dipole moments (on order of 1 debye), to produce the observed AME signature (Draine & Lazarian 1998b; Lovas et al. 2005; Thorwirth et al. 2007).

However, it should be noted that although nanosilicates have not yet been detected in the ISM, Hensley & Draine (2017) propose that an upper bound on the abundance of nanosilicates by Li & Draine (2001) (based on Infrared Telescope in Space (IRTS) observations by Onaka et al. (1996)), allow such small spinning grains to be composed primarily of silicates. This followed an earlier claim by Hensley et al. (2016) that the absence of a conclusive PAH-AME link suggested the possibility of AME-from-nanosilicates.

While neither nanosilicates nor any particular species of PAHs have been conclusively identified in the ISM, there is far more empiracal evidence for PAH-like dust than for nanosilicates. Mid-infrared features associated with PAH-like aromatic materials have been observed. In fact, "the PAH features" are ubiquitous in the ISM (Giard et al. 1994; Onaka et al. 1996; Onaka 2000), such that the carriers must be abundant. Andrews et al. (2015) strongly argue for the existence of a dominant "grandPAH" class, containing 20 to 30 PAH species.

1.6.5 Excitation factors

In the spinning dust model, there are several possible excitation factors for spinning dust. For the grains to have rotational velocities high enough to create the observed AME, they

must be subject to strong excitation mechanisms. The dominant factors that would be giving grains their spin, are broken down by Draine (2011) into basically two categories: 1) Collisional excitation. 2) Radiative excitation, the sum of which could lead to sufficient rotational velocities for sufficiently small grains. However the extent of excitation will depend on environmental conditions, i.e. there will be more frequent encounters with ions and atoms in denser regions (so long as the density is not high enough to coagulate the small grains), and more excitation due to photon emission with increasing ISRF strength (Ali-Haïmoud et al. 2009; Ali-Haïmoud 2014). One of the strongest potential excitation mechansims listed in Draine (2011) is that of negatively charged grains interacting with ions. Thus not only must we consider environmental factors, grain composition and size, but also the ionization state of the carriers. (For example, ionized vs. neutral PAHs.) The dependence of the observed AME on ISM density is modeled by Ali-Haimoud (2010).

1.6.6   AME vs. IR in the literature

The overall pattern among large-scale studies seems to show that all of the dust-tracing photometric bands correlate with the AME (and each other) to first-order. On an all-sky, pixel-by-pixel basis, at 1° angular resolution, Ysard et al. (2010) find that 12 μm emission, via IRAS, correlates slightly more strongly with AME (via WMAP) than with 100 μm emission. They also find that scaling the IR intensity by the ISRF improves both correlations. They interpret this finding as evidence that AME is related to dust, and more closely related to the small stochastically emitting dust — predominantly PAHs — that is traced by 12 μm emission. The improvement of the correlations after scaling by U is expected, as long as the 12 μm band is dominated by stochastic emisson from PAHs, in other words:

$$I_{12 \ \mu m} \propto U N_{PAH}, \tag{1.6.3}$$

where N_{PAH} is the column density of emitting PAHs (Onaka 2000). Such a relationship is expected, assuming that PAHs are small enough, and their heat capacities low enough, such that their emission is indeed stochastic– a single UV photon is absorbed, immediately followed by the emission of many IR photons. Under such conditions, a the radiation field would change only the intensity of PAH features, and not affect the spectral shape. Thus Ysard et al. (2010)

implies that $I_{12\ \mu m}/U$ is giving us a measure of the column density of spinning dust.

In a similar work however Hensley et al. (2016) report a lack of support for the spinning PAH hypothesis. Finding that fluctuations in the ratio of PAH-dominated 12 μm emission (via Wide-field Infrared Survey Explorer (WISE)) to dust radiance, R, (via Planck) do not correlate with the ratio of AME intensity to R, they conclude that the AME is not likely to come from PAHs. In terms of emission intensity however, their findings are consistent with Ysard et al. (2010) in that $I_{12\ \mu m}$ correlates well with I_{AME}. Thus there remains an open question as to what the actual carrier of the AME is.

The story is no more clear when looking at the average properties of individual regions. Planck Collaboration et al. (2014d) find that among 22 high-confidence "AME regions" (galactic clouds such as the ρ Ophiuchus cloud and the Perseus molecular cloud complex) AME vs. 12 μm shows a marginally weaker correlation than AME vs. 100 μm (via IRAS). Tibbs et al. (2011) examined the AME-prominent Perseus Molecular Cloud complex, finding that while there is no clear evidence of a PAH-AME correlation, they do find a slight correlation between AME and U.

1.7 Statistical Methods

In the following chapters, various IR datasets and analysis comparing the AME to dust emission will be described, along with a discussion of results testing the "AME from spinning PAHs" hypothesis. Because this particular hypothesis is challenging to test, due to the first order correlation of different constituents of interstellar matter, we apply variety of statistical techniques to explore if PAHs show any better correlation with AME than other dust metrics. These methods range from standard correlation tests to less common techniques, like the bootstrap test, and even relatively new approaches such as HB. It may be useful to go ahead and introduce this methods from the outset.

1.7.1 Correlation tests

Pearson correlation coefficient r_p is defined as follows:

$$\rho_{X,Y} = \frac{\text{cov}(X,Y)}{\sigma_X \sigma_Y} \tag{1.7.1}$$

where X and Y are the variables of interest, *cov* is the covariance between them. σ_X is the standard deviation of X, and σ_Y that of Y. To explain this conceptually, when we use r_p, we are essentially asking the question "How well can we represent these data as having a linear trend?" This is important to remember, as r_p is often confused as being simply a measure of correlatedness. This is partly true, in that stronger r_p scores indicate a better correlation. However lower scores may simply be indicating that a trend is not linear, or even that a linear trend is being overwheled by outliers or noise. For theses reasons, we will not use r_p in the following chapters. It is described here simply to aid in the understanding of its variant, the Spearman's rank correlation coefficient.

Spearman's rank correlation coefficient r_s can be thought of as a variation of r_p, and in fact depends on r_p and can be written as follows:

$$r_s = \rho_{\mathrm{rg}_X, \mathrm{rg}_Y} = \frac{\mathrm{cov}(\mathrm{rg}_X, \mathrm{rg}_Y)}{\sigma_{\mathrm{rg}_X} \sigma_{\mathrm{rg}_Y}} \tag{1.7.2}$$

where we see that r_p appears, but note that this is r_p as it is applied to the "rank" of the variables, indicated by rg_Y and rg_X, and not the original values. Thus a sorting of the variables is needed. *cov* is again the variance, and σ the standard deviation. The logic is similar to that in r_p, but the objective here is to test more generally for a monotonic relationship, not only linear. As a simple example, a pure power-law relationship would return a perfect 1 score for r_s, but not for r_p. Both tests would return 1 (or -1) for a purely linear relationship. Throughout the following chapters, we will use r_s.

Bootstrap analysis The "Bootstrap" test was first introduced by Efron (1979). The name comes the notion of fact that, without using any external information, we estimate the variation of a statistic directly from a population, "picking oneself up by one's bootstraps". Feigelson & Babu (2013) gives an updated description of the Bootstrap test within an astronomical context. The process involves creating N random re-samples of a population P_0, where the size of the re-samples n_{resamp} equals the size n_{orig} of P_0. This is carried out such that, when a datapoint is selected from P_0 and placed in the Nth re-sample P_i, it immediately becomes eligible for re-slection. This is known as "resampling with replacement". The effect is that, within the re-sampled populations P_i, some of the original data may be omitted, while others

may be over-represented. Ideally this process would be repeated for all of the re-sampling permutations, or $N = nPn$. This quickly becomes computationally infeasible, and $n * log(n)$ resamplings has become a conventional compromise, to sufficiently sample the distribution of your statistic in a reasonable time. Bootstrap tests are often applied to the Spearman and Pearson correlation tests, described above, to place an error estimate on correlation tests as well as de-weight outliers. Such an approach is applied in Chs. 3 and 4 to assess the reliability of Spearman scores between the AME and IR dust emission.

1.7.2 Optimization/Fitting Methods

Least-squares Method Ubiqutous throughout scientific and statistical literature, least-squares method (LSM) is the conventional way by which dust SED models have been fit to observational data, as in Tibbs et al. (2011). Essentially a minimization problem, the method can be described mathematically as follows:

$$S = \sum_{i=1}^{i=n} r_i^2 \tag{1.7.3}$$

where S, the quantity being minimized, is the sum of errors or "residuals" r_i between the model and the observational data.

Bayesian analysis Wheras in LSM we include no prior information regarding the likilihood of various output parameters, there is a well established framework by which we can do so. The implementation of Bayesian analysis, so far, has not been widespread in the study of interstellar dust. The concept however is by no means new, first being described mathmatically in Bayes & Price (1763). The central principle is known today as "Baye's theorem", given as:

$$P(A \mid B) = \frac{P(B \mid A)\, P(A)}{P(B)} \tag{1.7.4}$$

where, in the context of event probabilities, $P(A \mid B)$ is the chance that A will occur, given B. Likewise, $P(B \mid A)$, is the probability that B will occur, given A. $P(A)$ and $P(B)$ are then the probability that either event would be observed, regardless of the other. In other words, to compute the probability of two events being observed together, we must consider the probability of them occuring independently. In practice, when we use Bayesian tecniques,

what we are doing is building-in to our model some prior knowledge or expectation about the distribution of our output parameters. In contrast, when we use LSM, we are implicitly assuming that any output value is equally likely. In the Bayesian framework, we consider that we always have some type of prior expectation of the output distribution, and that this must be stated or selected up-front. This forms the foundation of a method implemented in Ch. 3 to fit the dust SED properties of λ Orionis, called HB.

Hierarchical Bayesian Analysis   In Bayesian analysis, we are specifying a prior expectation for our parameters up-front. The probability distribution that we use can significantly affect our result. If we instead infer a prior distribution from the data itself, we may be able to fine-tune the fitting process, and extract patterns that may not be readily revealed by standard Bayesisn analysis or LSM. This technique is implented in Ch 3, revealing a trend between PAH emission and the AME, forming the core result of this thesis. We will show also how the result could not have been demonstrated via LSM. The major advantages of HB are as follows:

- Prior is inferred from the data

- Less vulnerable to local minima

- Avoids noise-induced correlations

- Robust error propagation

The major disadvantage however is that HB is relatively expensive, computationally, compared to LSM. Also, in the case of only a single data source, we would not be able to build a prior distribution function from the data.

1.8   Scope of this Dissertation

We attempt to add to the understanding of AME and the possibility of spinning dust emission. With ample multiwavelength data now available, and a new PAH-focused all-sky survey in preparation by AKARI, we further test the PAH hypothesis, and assess how the IR to AME correlation changes as a function of wavelength. This thesis represents the first time that AKARI IRC data, have been utilized for AME investigation. Moreover, Ch. 3 represents the first time that AKARI data, and hierarchical Bayesian dust SED fitting respectively, have been

used to investigate the λ Orionis region. The result of Ch. 3 is likewise unique in that it is the first time a link between AME and PAHs has been demonstrated in λ Orionis, and the first time that AME in any particular region has been shown to correlate better with PAH mass than with the total dust mass. Chs. 3 and 4 both utilize a greater number of mid IR to sub-mm photometric bands, than have ever been used for AME investigations. More specifically, this work represents the first use of a photometric band covering the 6.2 μm C-C stretching PAH feature, for a wide-scale galactic investigation.

1.8.1 An application of all-sky archival data

This is an astrophysical data archive based work. The primary goal is to highlight a particular application of multiwavelength (mid-IR to radio), cross-archive all-sky data analysis. We describe the interrelatedness between mid to far IR dust emission and possible microwave emission from dust. This is accomplished through an investigation of photometric all sky maps mainly from AKARI, IRAS, Planck, and DIRBE.

1.8.2 Testing the spinning PAH hypothesis

For the present work, we consider the spinning PAH hypothesis to have the highest degree of testability, due to the well-established presence of aromatic emisison features in the ISM. We do not argue against the physical plausibility of nanosilicates to produce the AME. Indeed, there is no argument to date that these potential physicalities are mutally exclusive, as long as both potential carriers are sufficiently abundant. Nor does spinning dust emission theoretically exclude magnetic dipole emission or microwave thermal dust emissivity fluctuations.

1.8.3 Limitations

We do not explore the modeling of microwave dust emission itself, rather we refer to estimates of spinning dust emisison provided in the literature (Planck Collaboration et al. 2014c; Bennett et al. 2003a) in the form of archival data and parameter maps. We consider this problem first on an all-sky basis, not focusing on any pre-selected object of the sky — in order to assess if there any general pattern between the IR and the AME, beyond the AME-dust correlation already described above. We then focus on a region highlighted by the Planck Collaboration as being especially worthy of further investigation (Planck Collaboration et al. 2016b), and

has a resolvable topology even at 1° resolution. Essentially all of the analyses and conclusions presented in this work apply to an angular scale of approximately 1°, and only for the given component separation methods (Solar system, galactic, extragalactic) used by each of the data providers.

1.8.4 Code availability

Because this work is intended to contribute working examples for future students, in addition to making a research contribution, this thesis is accompanied by a `github` repository (to be made available upon acceptance of the thesis.) [1] Most of analyses code are available in that repository, in the form of Jupyter notebooks. Most of the figures, and code used to generate them, are also included. The hierarchical Bayes dust SED fitting code used in this work was developed by Galliano (2018), and its implementation in this work was carried out in collaboration with their group. The details of the code are described in Galliano (2018), and are not included in the respository for this thesis.

---

[1] Available at: `https://github.com/aaroncnb/CosmicDust`.

Chapter 2

Data Sources

2.1 A collection of skies

This work relies completely on all-sky surveys. All of the maps utilized are photometric-band infrared maps, except for the AME data, which is an all-sky component separation analysis product, from the Planck Collaboration's efforts to separate galactic foregrounds from the CMB. Table 2.1 summarizes the observational data used in this thesis. In total, we employ

Table 2.1: Observational data sources used in this article

Instrument	Central Wavelength	FWHM	Calibration Uncertainty	Reference	Dust SED Coverage
AKARI/IRC	9 μm	~10"	<10%	[1]	6.2, 7.7, 8.6 and 11.2 μm PAH features
AKARI/IRC	18 μm	~10"	<10%	"	VSGs
AKARI/FIS	65 μm	63"	<10%	[2]	VSGs, themal eq. grains
AKARI/FIS	90 μm	78"	<10%	"	themal eq. grains
AKARI/FIS	140 μm	88"	<10%	"	themal eq. grains
AKARI/FIS	160 μm	88"	<10%	"	themal eq. grains
COBE/DIRBE	160 μm	88"	<10%	"	themal eq. grains
IRAS/IRIS	12 μm	4.0′	<5.1%	[3]	8.6, 11.2, 12.7 μm PAH features
IRAS/IRIS	25 μm	4.0′	<15.1%	"	VSGs
IRAS/IRIS	60 μm	4.2′	<10.4%	"	VSGs, themal eq. grains
IRAS/IRIS	100 μm	4.5′	<13.5%	"	themal eq. grains
Planck/HFI	345 μm	4.7′		[4]	themal eq. grains
Planck/HFI	550 μm	4.3′		"	themal eq. grains

all-sky maps from 12 photometric bands, spanning the wavelength range of 6.9 μm to 550 μm

---

[1] Ishihara et al. (2010)
[2] Doi et al. (2015); Takita et al. (2015)
[3] Miville-Deschênes & Lagache (2005)
[4] Planck Collaboration et al. (2014b)
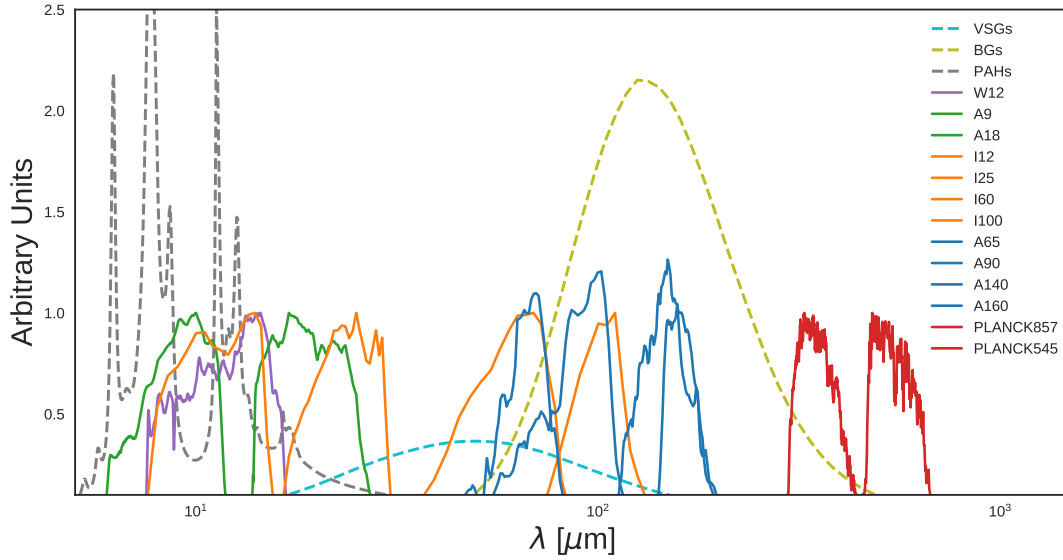
Figure 2.1: Relative spectral response curves of the bands used in this study. Expected dust emission components, assuming the dust SED model by (Compiègne et al. 2011) are also shown. The components are summarized as emission from BGs (dashed yellow line), emission from VSGs dashed blue line), and emission from PAHs (dashed grey line).

as shown in Fig. 2.1. The following sections give the details of the observational data from each instrument as well as of the parameter maps provided in Planck Collaboration et al. (2016b).[5] From this point in the thesis, we will mostly use abbreviations to refer to the different bands, as follows: 'A' indicates AKARI; 'D', DIRBE; 'I', IRAS, and 'P' Planck. The number after each letter indicates the band central nominal wavelength in microns (or frequency in GHz, in the case of the Planck bands.)

Table 2.2: Ancilliary data

Product	Relevant Freq./Wavelen	FWHM	Reference/URL
$H\alpha$	658.5 nm	$36'$	[6]
$N(H)$	21 cm	$36'$	[7]
PC R (PR1)	353 GHz	$5'$	[8]
PC τ_{353} (PR1)	353 GHz	$5'$	"
Haslam MHz	408 MHz	$56'$	[9]
PC Synchrotron (PR2)	408 MHz	$60'$	[10]
PC AME_{var} (PR2)	22.8 GHz	$60'$	[11]
PC AME_{fix} (PR2)	41.0 GHz	$60'$	"
PC free-free (PR2)	N/A	$60'$	[12]

---

[5]Planck bands are named according to their central frequency, not wavelength.

2.2 AKARI

The AKARI infrared space telescope revealed an entire sky of infrared light, from the mid to far infrared, via two instruments (Murakami et al. 2007) the IRC (Onaka et al. 2007) and the FIS (Kawada et al. 2007b). In this section we will discuss the all-sky surveys produced by these two instruments .

2.2.1 AKARI/Infrared Camera (IRC)

IRC proivded us with both spectroscopic and phometric data from the near to mid-infrared. In this work, we utilize the all-sky maps centered at 9 and 18 μm, created during the IRC's fast-scanning phase. We utilize the most recent version of the IRC data (Ishihara, et al., in prep.) This version has had an updated model of the Zodiacal light, fitted and subtracted. The details of the improved Zodi-model, which offers an improvement over that used for the IRAS all-sky maps, are given in Kondo et al. (2016).

PAH feature coverage

The A9 all-sky map demonstrates the abundance of the PAH bands carrier in the Milky Way (Ishihara et al. 2010). Figure 2.2 shows the coverage of the PAH features (from both ionized and neutral PAH components), as they are theoretically determined in Compiègne et al. (2011). The A9 band uniquely covers major ionized PAH features at 6.2 and 7.7 μm; as well as neutral PAH features at 8.6 and 11.2 μm across the entire sky (Onaka et al. 2007). The I12 band covers the 11.2 and 8.6 μm features, and the similarly-shaped W12 band covers primarily the 11.2 μm feature but do not cover the 7.7 μm completely. According to the distribution of PAH features

---

[6]Finkbeiner (2003):
`https://lambda.gsfc.nasa.gov/product/foreground/halpha_map.cfm`
[7]Kalberla, P. M. W. et al. (2005):
`https://lambda.gsfc.nasa.gov/product/foreground/fg_LAB_HI_Survey_get.cfm`
[8]):
`http://irsa.ipac.caltech.edu/data/Planck/release_1/all-sky-maps/previews/HFI_CompMap_ThermalDustModel_2048_R1.20/index.html`
[9]Haslam et al. (1982):

[10]Planck Collaboration et al. (2016b):
`http://irsa.ipac.caltech.edu/data/Planck/release_2/all-sky-maps/previews/COM_CompMap_Synchrotron-commander_0256_R2.00/index.html`
[11]`http://irsa.ipac.caltech.edu/data/Planck/release_2/all-sky-maps/previews/COM_CompMap_AME-commander_0256_R2.00/index.html`
[12]`http://irsa.ipac.caltech.edu/data/Planck/release_2/all-sky-maps/previews/COM_CompMap_freefree-commander_0256_R2.00/index.html`
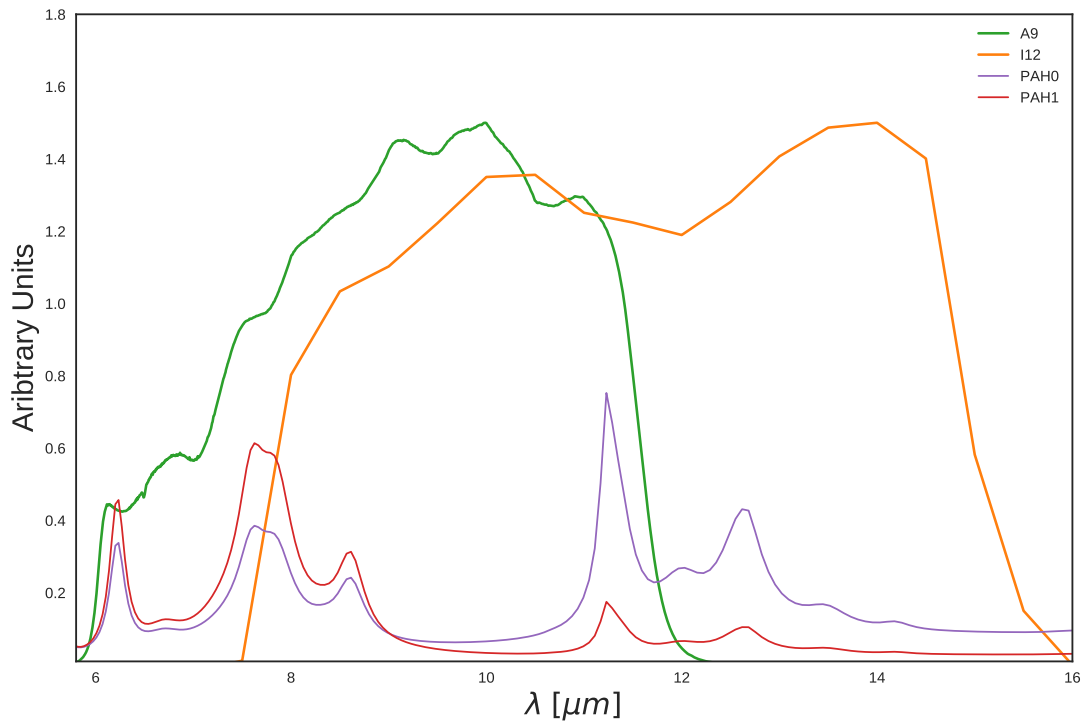
Figure 2.2: The I12 (orange) and A9 (green) filters coverage of modeled ionized (PAH1, red) and neutral (PAH0, purple)components of PAH features by Compiègne et al. (2011). The difference in the PAH feature coverage mainly comes from the 6.2 μm and the 7.7 μm feature.
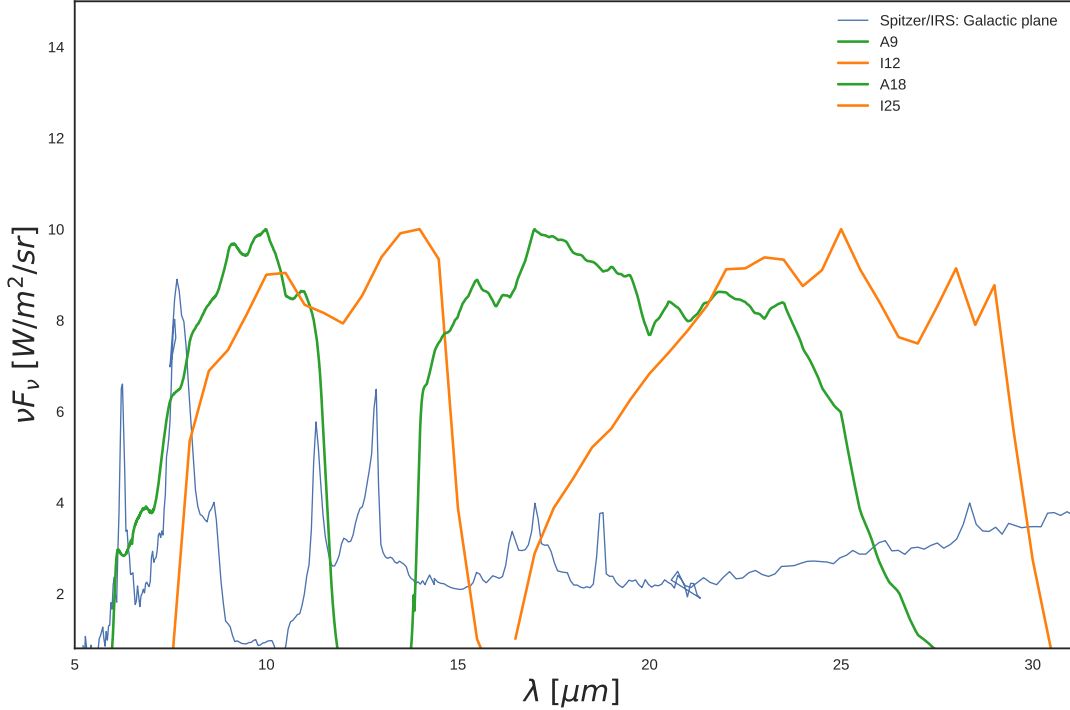
Figure 2.3: Coverage of MIR wavelengths by the filters used in this work. An Spitzer/IRS spectrum (see AOT4119040) of the galactic plane (thin blue line) demonstrates how IRC and IRAS photometric bands trace these features on an all-sky basis (Ishihara et al. 2007). Strong PAH features overlap with the A9 and I12, while the A18 and I25 micron bands only trace much weaker features.

across the response filters in Fig. 2.2, and referring back to the various dust components in Fig. 2.1 it is also expected that the A9 band is most dominated by PAH emission even with increasing U. This may seem counter-intuitive, since, as described in Ch. 1, the PAH spectral shape does not show a temperature variation. However as T increases, the MIR extent of thermal dust emission and emission from VSGs encroach on I12 and WI2 sooner than A9, diluting emission from PAHs. In some ionized reigons, I12 may also include non-significant contributions from the [NeII] line at 12.8 μm. Figure 2.3 demonstrates an example observational galactic cirrus spectrum in the MIR, from Spitzer Infrared Spectrograph (IRS) (Werner et al. 2004) data, along with filters for all of the MIR bands used in this study. It indicates that the other MIR bands, A18 and I25, do cover strong PAH features and are expected to be dominated rather by emission from very small grains (VSGs), as was indicated in Fig. 2.1.

To help demonstate how the relative contribution from PAHs will change for each band, for different ISRF strengths, Fig. 2.4 gives just such a calculation. These contributions remain relatively constant out to a U of about 100, with the contribution from warm dust becoming
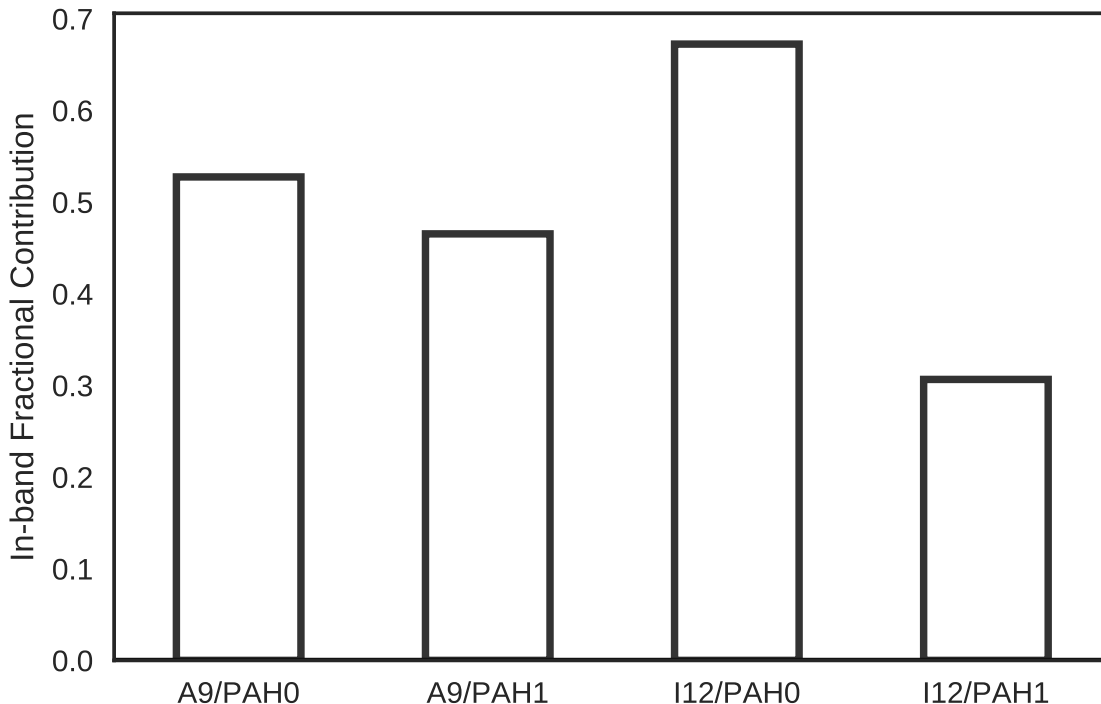
Figure 2.4: In-band contributions from charged (PAH1) neutral (PAH0) PAHs, to the emission detected by the I12 and A9 filters. These assume a model galactic cirrus spectrum simulated with the SED template of Compiègne et al. (2011).

a larger factor for the I12 and W12 bands. Thus, according to the DL01 template, A9 should have the highest contribution from PAHs out to extreme radiation fields. At least to the extent with which PAHs can endure harsh UV radiation, as PAHs are expected to evaporate in strong enough radiation fields (Allain et al. 1996a,b; Bocchio et al. 2012; Pilleri et al. 2012; Pavlyuchenkov et al. 2013).

PAH ionization

Figure 2.2 indicates that expected emission from ionized PAHs may preferentially contribute to the A9 band, even though both I12 and A9 cover ionized and neutral features. A PAH SED model calculation, using the Compiègne et al. (2011) SED template, supports that for Galactic cirrus ISM conditions, emisison detected by the A9 band would have a higher contribution from charged PAHs than the I12 band. This is demonstrated in Fig. 2.4. To be clear, both bands are sensitive to both charged and neutral PAHs, however the relative contribution from charged PAHs is expected to be higher for A9. Thus we might expect that the ratio of intensities in this two bands, for a given line of sight (towards which PAHs are not destroyed), could trace
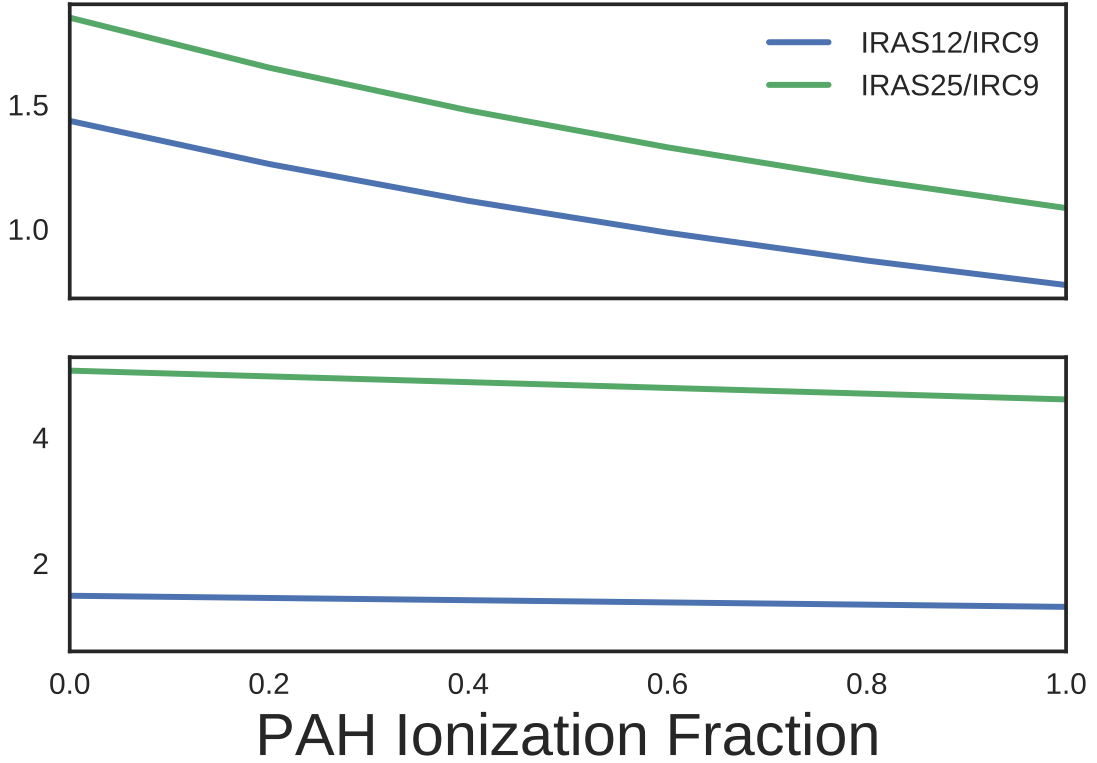
Figure 2.5: Ionization fraction of PAHs vs. band ratios of I12, I25, to A9, for two ISRF strengths: Top: $U = 1$, Bottom: $U = 10$. These ratios are determined by assuming the SED template of Compiègne et al. (2011)

the fraction of charged PAHs. Estimating the extent of this effect, Fig. 2.5 gives the results of a calculation of I12/A9 and I25/A9 band ratios for two ISRF strengths. This calculation is again based on Compiègne et al. (2011). It suggests that at least for $U <\sim 10$, the fraction of charged PAHs may be estimated as a function of the I12/A9 ratio.

Examing how this might look in the data themselves, Fig. 2.6 and Fig. 2.7 show the R(A9:I12) and R(A9:I25) ratio maps, demonstrating the relative variations in these MIR bands accross the sky— or at least the portions of the sky where S/N is sufficient. While from visual inspection the various MIR intensity all-sky maps appear to essentially trace the same stuctures of the galaxy, the ratio maps reveal that there are indeed differences to be explored. In regions where noise is dominant, ascertaining the ionization fraction will be quite difficult. This can be easily seen upon visual inspection of the ratio maps, in that there is a clear deliniation between brighter emission towards lower galactic latitudes, and the high latitude sky where the ratio shows very little discernible structure (except for the Zodi-residual patterns which differ between IRC and IRAS). Thus there may a large portion of the sky where the S/N may be high enough to allow us to trace the PAH ionization fraction. This possibility is explored in
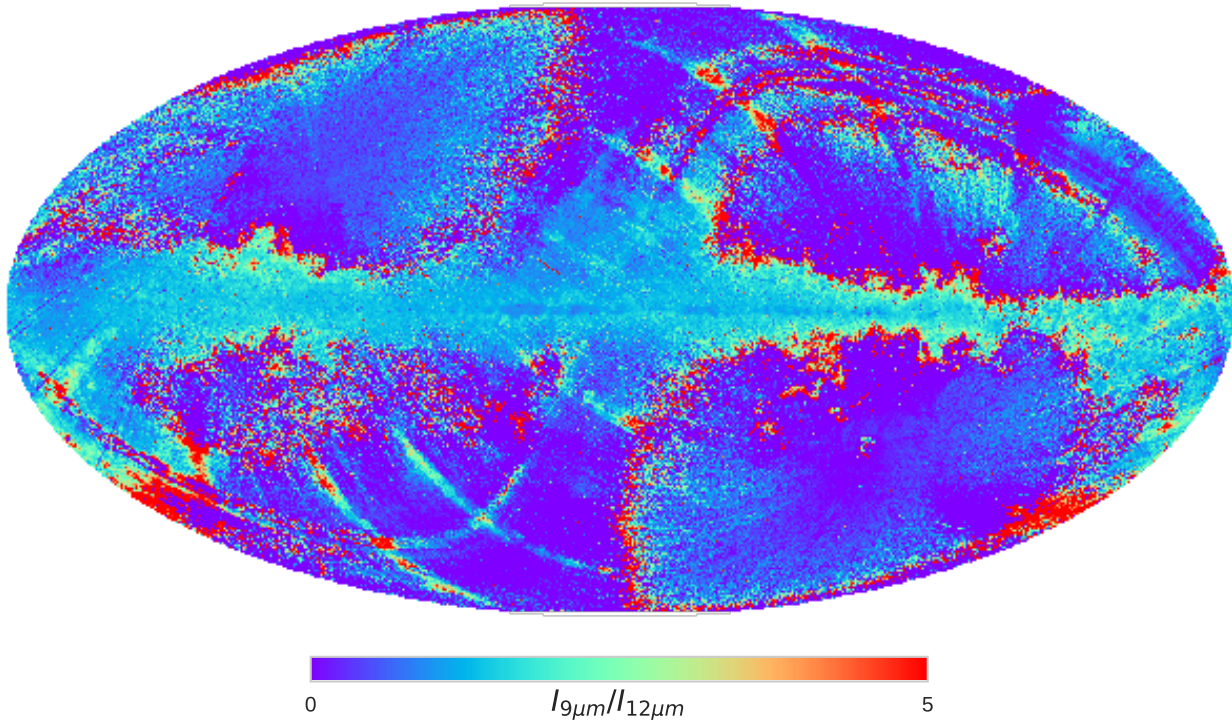
Figure 2.6: AKARI/IRC 9 μm to IRAS 12 μm intensity ratio.

Ch. 3, in looking at the PAH distribution within λ Orionis.

2.2.2 The AKARI Far Infrared Surveyor (FIS)

FIS gives us photometric data around the peak of the typical thermal dust SED. FIS was equipped with four wavebands: two narrow bands centered at 65 μm and at 160 μm, and two wide bands at 90 μm and at 140 μm. An all-sky survey was carried out at each band (Kawada et al. 2007a), and the processed maps have been publicly released (Doi et al. 2015).

2.2.3 Planck Observatory High Frequency Instrument (HFI)

The HFI all-sky maps, spanning 100 to 857 GHz (Planck Collaboration et al. 2014b) help constrain the far IR dust emissivity. This study utilizes the 857 GHz (345 μm) and 545 GHz (550 μm) bands.
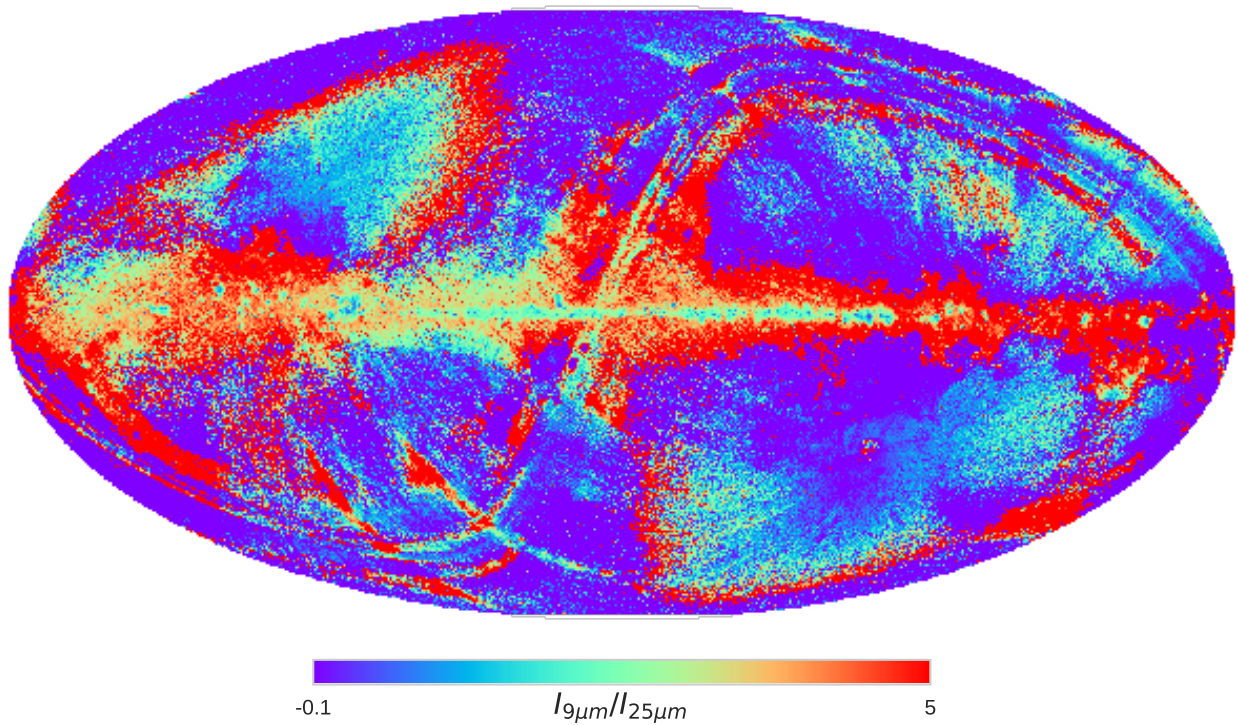
Figure 2.7: AKARI/IRC 9 μm to IRAS 25 μm intensity ratio.

2.3   Infrared Astronomical Satellite (IRAS)

Data from the IRAS (Neugebauer et al. 1984) all-sky surveys are used to supplement the similarly-centered AKARI photometric bands. The IRAS 12 μm band is similar to the IRC 9 μm band in terms of the sky coverage, central wavelength, and especially in that both surveys are heavily dominated by zodiacal light. We use the Improved Reprocessing of the IRAS Surveys (IRIS) (Miville-Deschênes & Lagache 2005), which have undergone a zodiacal-light removal. The zodiacal light model, however differs between the two bands. The IRAS zodi-subtraction is primarily based on the Kelsall et al. (1998) model, while IRC employs a modified version of this model (Kondo et al. 2016). Although WISE provides higher resolution than IRAS, we do not utilize the WISE data because we found the WISE all-sky 12 μm product to essentially trace the Planck HFI 857 GHz map, at 1° angular resolution. Hensley et al. (2016) had noted that this scaling of the WISE map may artificially suppress actual PAH-related variations at low resolution. Moreover, since we are conducting our analysis at 1° resolution in order to match the AME data, the higher resolution offered by WISE is not a significant advantage.

2.4   Planck COMMANDER Parameter Maps

We utilize the COMMANDER-Ruler astrophysical component separation maps (Planck Collaboration et al. 2014c), from the Planck Collaboration's Public Data Release 2 (hereafter, PR2)(Planck Collaboration et al. 2016a). These contain estimates of known microwave foreground components (free-free, synchrotron, thermal dust emission contributions to the Planck photometric bands. Fig. 2.8 demonstrates the correlatedness of these component maps, taken as provided in the PR2 archive. To construct the cross-correlation matrix, we use the entire maps as provided by PR2, at HEALPix NSIDE 256. This corresponds to a pixel scale of approximately 0.25°. The effective beam size of these maps is given by PR2 as 1°. We do not mask any additional pixels, or provide any data smoothing. Without considering noise levels or variations of scale, we see evidence these major components are correlated with one another. In the case of free-free emission, von Hausegger & Liu (2015) found that by taking S/N ratios into account, the correlation between COMMANDER free-free and AME components turns negative. More generally they suggest that the intercorrelations betwen these products varies with scale. We will first describe the 'non-AME' components, so as to not give any indiciation that their estimation is trival.

2.4.1   Synchrotron

While the Planck observations themselves do limit our resolution when assessing the AME - it is the primary constraint on synchrotron emission, 408 MHz map by Haslam et al. (1982) that is the major resolution limiting factor. While an impressive early effort to reveal the low-frequency sky, (Haslam et al. 1982) is limited to an approximately 1° resolution. The map also contains many artifacts. For the time being however, it is still the most synchrotron-dominated all-sky map available, and for this reason PC15X included it in their COMMANDER component separation. Enhanced synchrotron mapping efforts are currently in progress by the 'The final synchrotron product produced by COMMANDER (hereafter, PCSync) highly resembles the Haslam et al. (1982) map, however it is also demonstrated PCSync does not fully capture the synchrotron signal. Hensley et al. (2016) further note that the PCAME:PCdust ratio map can be described as containing synchrotron emission patterns at high latitudes.

Figure 2.8: r_s cross correlation matrix of the PCCS maps: temperature T, emissivity index β, and amplitude at 545 GHz $I_{dust}(545)$ of thermal dust; intensity of free-free emission ff at ; intensity of synchrotron emisison at 4 MHz $Sync$; intensity of the AME var. freq. component AME at 22.8 GHz.

2.4.2 Free-free emission

Unlike the PCSync component, the fitting of the Planck COMMANDER free-free component map (hereafter, PCff) does not employ any free-free dominated emisison map, even though an earlier Planck AME paper (Planck Collaboration et al. 2014d) had employed the $H\alpha$ map by Finkbeiner (2003). Uncertainties in this map arise from uncertainties in the gas temperature, and the Gaunt factor. This emission source is the dominant source of confusion with AME, especially for HII regions (Planck Collaboration et al. 2014d,c; Paladini et al. 2015).

2.4.3 Thermal dust emission

"Thermal dust emission" in the COMMANDER context refers to dust emission in the Rayleigh Jeans-regime, as the COMMANDER fitting includes neither photometric constraints on the thermal emission peak, nor on Wiens-regime emission from small grains. This component essentially involves the fitting of a modified blackbody curve (Eq. **??**.) to the Planck Photometry. This approach however results in an apparent anti-correlation between β and T (Fig. 2.8). Whether or not this anti-correltion is genuine is still unsettled in the literature (Galliano et al. 2011; Juvela & Ysard 2012). In any case, we do not utilize the β and T, only the dust intensity at 545 GHz (I_d) parameter map.

2.4.4 AME data

The COMMANDER map release also provides an "AME component map", which presumes that AME originates from spinning dust. While acknowledging that such a decomposition lacks a strong physical interpretation, Planck Collaboration et al. (2016b) break the AME into two components: a spatially varying peak frequency component, AME_{var}, and a spatially constant peak frequency component, AME_{fix}. As seen in Fig. 2.9, virtually all of the fitted peak frequncies for AME_{var} are beyond the reach of WMAP and Planck. Only the fitted global frequency, 33.5 GHz for the spatially constant component, is covered. However they note that the combined components, per pixel, would have an average peak at least within the WMAP coverage range. In any case, we stress that while this is the most careful all-sky attempt to isolate the AME to date, the constraints of the the frequency peak are still heavily lacking. In general, AME_{var} is the dominant component, accounting for approximately 90% of the total
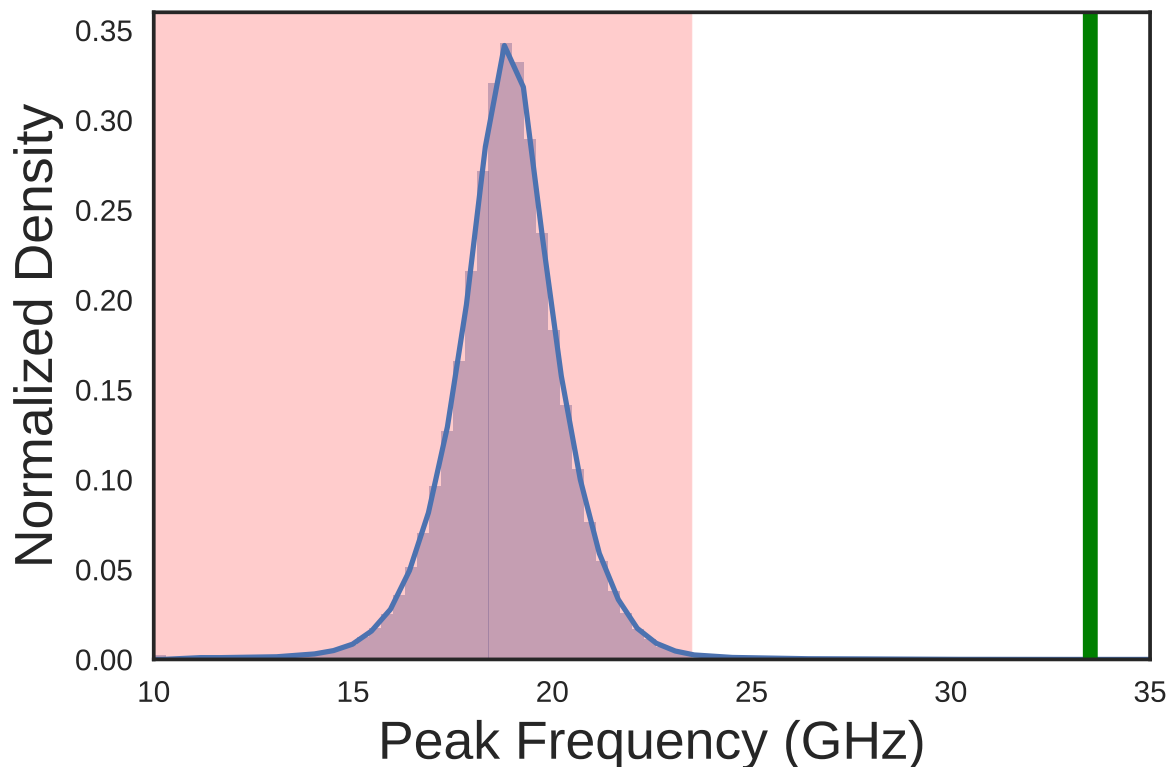
Figure 2.9: The peak frequencies of the varying component AME_{var}. The pink shaded region indicates frequencies not covered by either WMAP or Planck The green line at 33.5 GHz indicates the peak frequency of AME_{fix}.
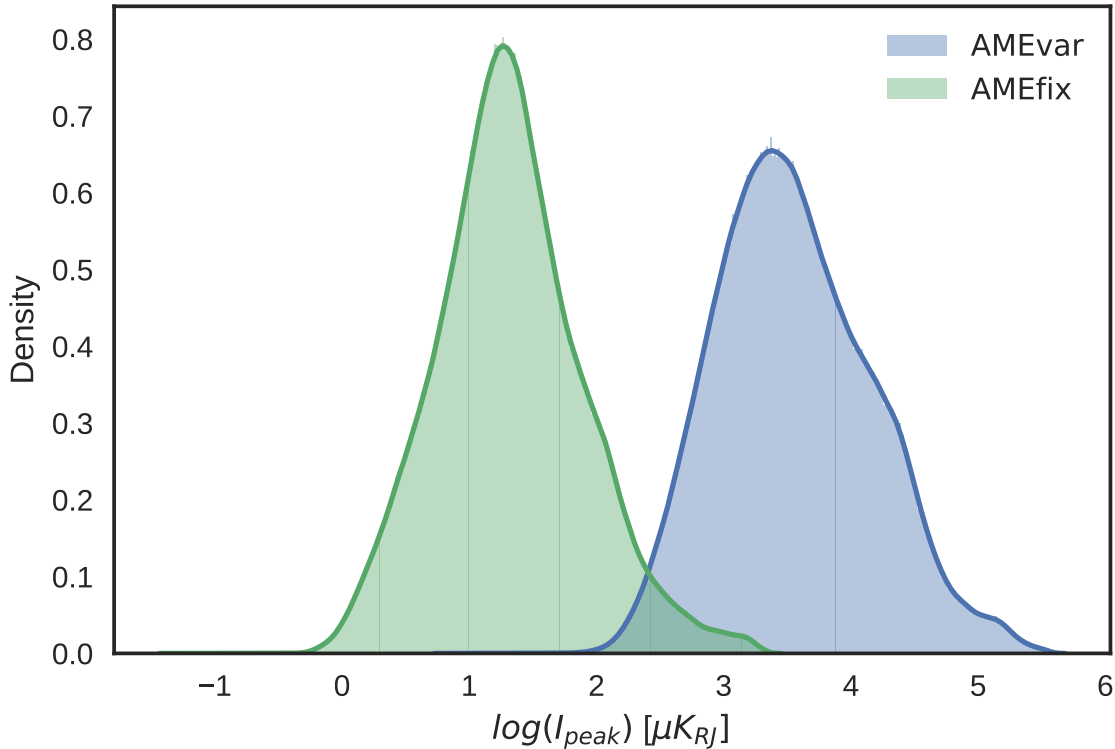
Figure 2.10: Histograms of the peak intensity AME maps calculated from the original COMMANDER-AME reference frequency maps. The dominant component, AME_{var} is indicated in blue, for all pixels in the map, with their spinning dust intensities evaluated their peak frequencies (see Fig. 2.9.) AME_{fix} gives the peak intensity of the spatially-constant frequency component, indicating it is essentially always the weaker component.

fitted AME intensity between 20 and 40 GHz, indicated by the full-sky histograms in Fig. 2.10. The intensities given by PC are evaluated at reference frequencies: 22.8 GHz for AME_{var}, 41 GHz for AME_{fix} (for convenient comparison to the WMAP total intensity maps at those frequencies). They are not fitted peak intensities of the spinning dust SED model.

While acknowledging that the frequency constraints are lacking, we choose to use these parameters maps in a self-consistent way, by taking the intensities and frequencies given by PC, and calculating the implied peak intensity. In any case, we find that this conversion does not have a significant effect on the results in the chapters to follow, except in the case of some outlying pixels with very low peak frequencies, easily seen in the map of the fitted frequencies in Fig. 2.11. These low frequency pixels result in very high AME peak intensities. On comparison to point source masks by Planck, we find that these outliers correspond to intensity outliers in the LFI 30 GHz map.
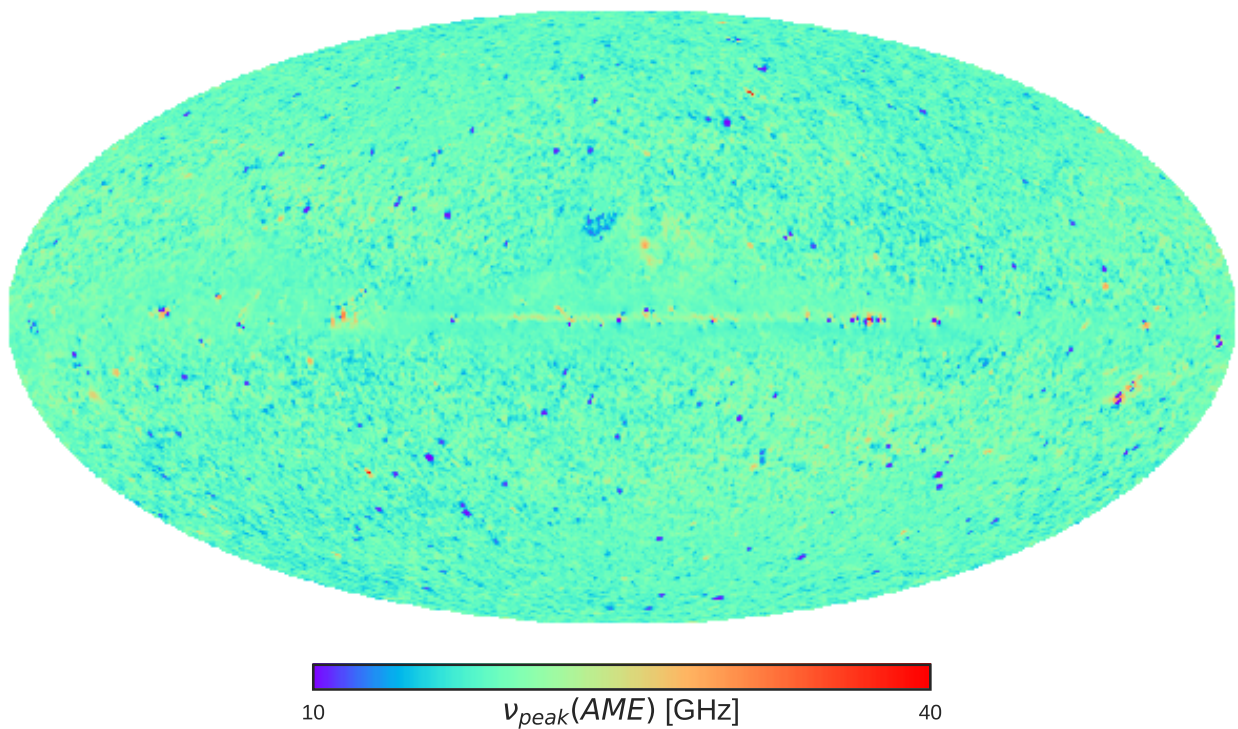
Figure 2.11: All-sky map of the peak frequencies of the varying component AME_{var}, corresponding to Fig. 2.9. Virtually all of the purple regions of the map correspond to pixels flagged for point sources in the LFI data. There are very few notable structures in the frequency map overall, other than the galactic plane itself, ρ Ophiuchus, and Perseus.
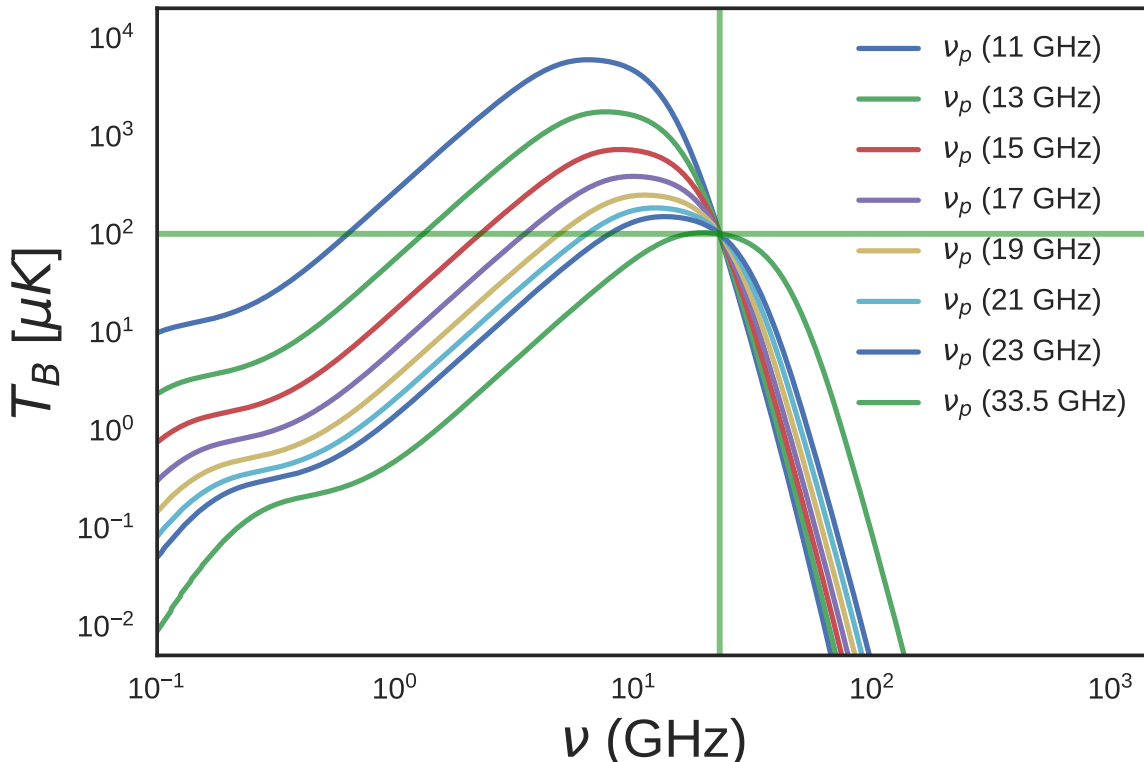
Figure 2.12: Spdust template spinning dust profiles fitted by PC15X when calculating AME_{var}. The reference frequency, 22.8 GHz is indicated by the vertical green line. Each template has the same AME_{var} amplitude of 100 μK, indicated by the horizontal green line, plotted to highlight the potential deviation between AME_{var} and the actual peak intensity.

Spinning dust fitting

The actual spinning dust SED template used by PC15X to fit the AME is indicated by Fig. 2.12, which we have reproduced from the original template provided in Ali-Haïmoud et al. (2009). PC15X fit the AME by applying a frequency shift and intensity shift parameter to this template. The physical parameters of the `spdust` model itself are not directly varied in PC15X. In any case, the spinning dust model SED shape does not show significant variation from environment to environment (Ali-Haïmoud et al. 2009). Because of the phenenological approach of the AME fitting method, the PC15X authors themselves suggest caution in deriving conclusions from comparisons with the COMMANDE AME map. However it is the most thorough all-sky component separation currently available, and has not been well analyzed relative to the full wavelength range of available IR all-sky maps. Improving on the COMMANDER AME map will likely require lower frequency constraints (in the red-shaded portion of Fig. 2.9) and/or higher resolution observations of not only the AME itself but the contribution from synchrotron and free-free emisson. This way some of the inherent degeneracies between free-free, synchrotron,

thermal dust, and AME parameters may be able to be broken.

2.5 All-sky Data Processing

The HFI, FIS, and IRIS maps used here are downloaded from their respective online repositories, as all-sky HEALPix[13] maps (Górski et al. 2005). NSIDE 2048 maps. In the case of the IRC maps, we first create HEALPix maps from the 4,857 all-sky survey tiles using the Aladin all-sky data visualization platform (Bonnarel et al. 2000). NSIDE 2048 implies an average pixel spacing of 1.7′. The maps are then degraded to NSIDE 1024 before carrying out a Gaussian-beam smoothing to a 1° FWHM. Map smoothing itself is done in spherical harmonic space, before the maps and transformed back to position space. These steps are handled by the smoothing function contained in the `healpy` python package. Following the smoothing process, the maps are degraded once more to NSIDE 256, or 15′ pixel-width [14]. The value of each of the larger NSIDE 256 pixels, comes from the mean of its parent NSIDE 1024 pixels. The purpose of this processing is to ensure that all of the maps have the same resolution as the PR2 AME map.

---

[13]HEALPix core software is described at `http://healpix.sourceforge.net`. The HEALPIx python package `healpy` used in this work is available at: `https://github.com/healpy/healpy`

[14]HEALPix pixel scale rebinning carried out with `healpy.ud_grade`

Chapter 3

Analysis of an interesting AME region: λ Orionis

This chapter is an analysis of the AME and how it relates to the dust emisison, in the λ Orionis region. This has been an ongoing collaboration with F. Galliano, an expert in dust SED fitting and developer of a dust SED framework presented in Galliano (2018). This work has been enabled by mutual collaboration vists by myself and F. Galliano, funded in part by a joint JSPS-CNRS international collaboration grant. The results described here are intended to form the core of a journal publication, to be submitted in the coming months.

3.1   An interesting AME region

The λ Orionis molecular ring, also known as the Meissa Ring is a massive stucture surrounding the λ Orionis O-type star. The ring contains an HII region, ionized by λOri itself and its OB associates (Murdin & Penston 1977). What had been thought of as a starforming region of missing molecular gas. At the time Murdin & Penston (1977) even speculated that this could be evidence of an alternate starformation pathway, writing: "Notably we need to know if λOri is an example of a different mode of star formation or [...] simply a case in which the progenitor molecular cloud was exhausted within the last one or two million years."

Maddalena (1986); Maddalena & Morris (1987). (and references therein) noted a ring of material likely being pushed out by the central, historically well-known λ Orionis Association of B-type stars and surrounding HII reigon.

Cunha & Smith (1996) argued that the ring shape around λ Orionis may have resulted from a supernova explosion, further speculating that λOri may have been a companion of the progenitor. λ Orionis is a known binary system, however its current companion is a B-type star. (Murdin & Penston 1977) . The central region is heated by the λ Orionis star itself, and the Orion OB association it belongs to (Ochsendorf et al. 2015). The region is known to host several young stellar and protostellar objects (Koenig et al. 2015).

At approx. 10° wide, we can see the outline of the structure even in the low (1° FWHM) resolution PCAME map. The ring shape itself is thought to originate from a supernova, or perhaps combined effects of the entire star formation history of the λ Orionis Association, including the formation of its surrounding HII region (Aran 2009).

Although the λ Orionis region has been a popular target for study since approximately the 1980s. Duerr et al. (1982) wrote of the relative lack of work on the overall region: "Surprisingly, this interesting complex has been little studied". While this seems surprising given the numbe of works on the region in the literature now, it is really the advent of all-sky missions that have driven more recent interest. The large angular size is such that all-sky surveys were a natural boon for study of such extended structures. WISE especially was a huge source of insight (Koenig et al. 2015). More recently, Planck Collaboration et al. (2016c) strongly highlighted the region as a strong candidate for further AME investigation.

3.2 Investigative approach

We have carried out an initial comparison of the AME of this region with its mid to far-IR dust emission. The region is shown in Fig. 3.1 as it appears in 1°-smoothed A9 data. The ring structure itself indicates excess microwave emission attributed to AME, from the dominant variable frequency component AME_{var} (see Ch. 2). The central region is dominated by free-free emission (Aran 2009; Koenig et al. 2015). Free-free emisison coming from the Hii phase surrounding the λ Orionis association dominates the region's morphology in Low Frequency Instrument (LFI) images. (Planck Collaboration et al. 2016c). Taking the hint from Planck Collaboration et al. (2016c) that this may be among the more reliably component separated regions, we evaluate if there is any preferential relationship between any parameter of dust emission and the AME. Fig. 3.2 shows the expected distribution of free-free emission in the
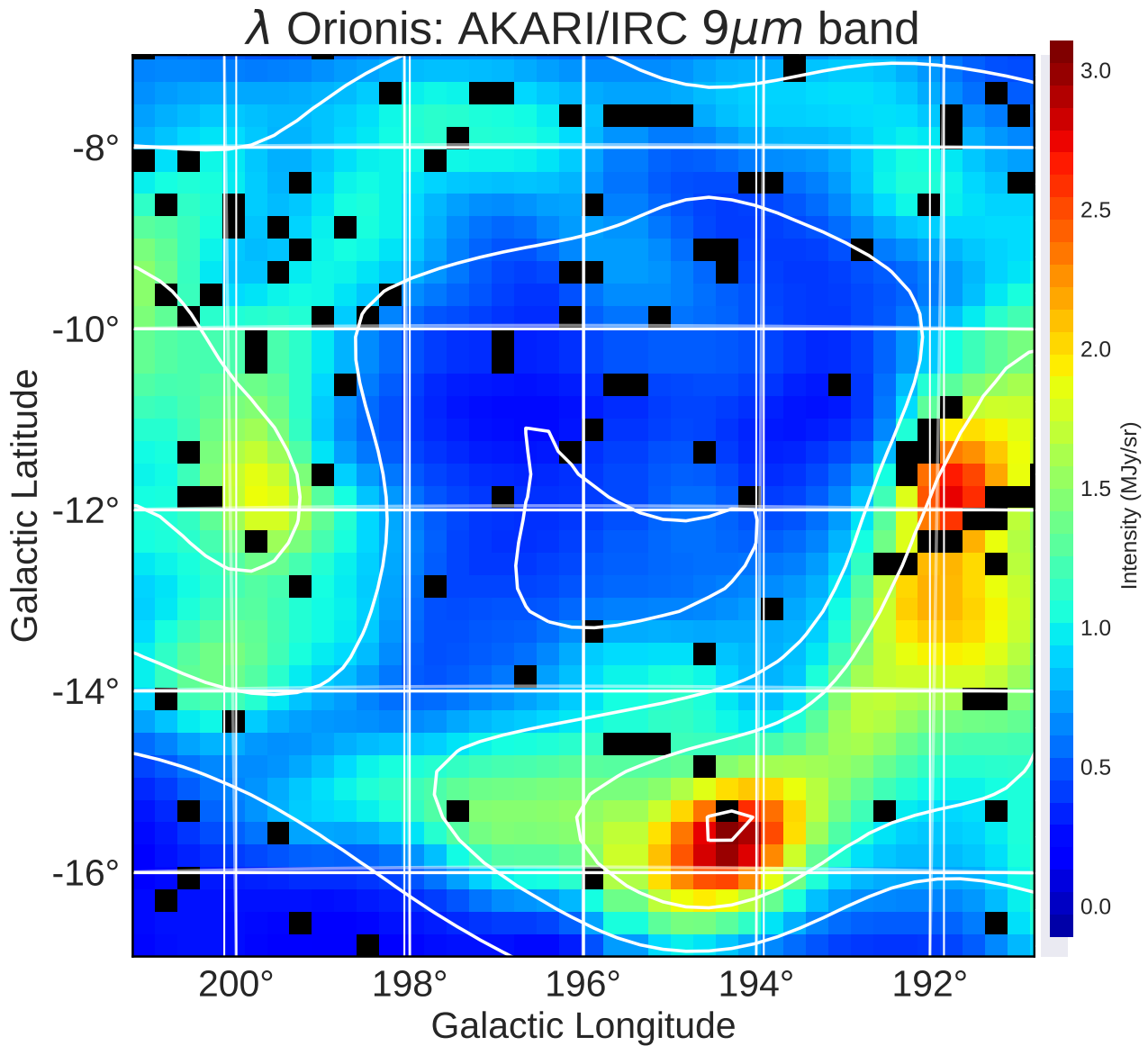
Figure 3.1: λ Orionis as it appears in the AKARI 9 μm data. Contours indicate the AME, as given by the Planck PR2 AME map. The image is smoothed to a 1° PSF (much larger than the original 10 arcsec map). The λ Orionis star itself is approximately located at the center of the image.
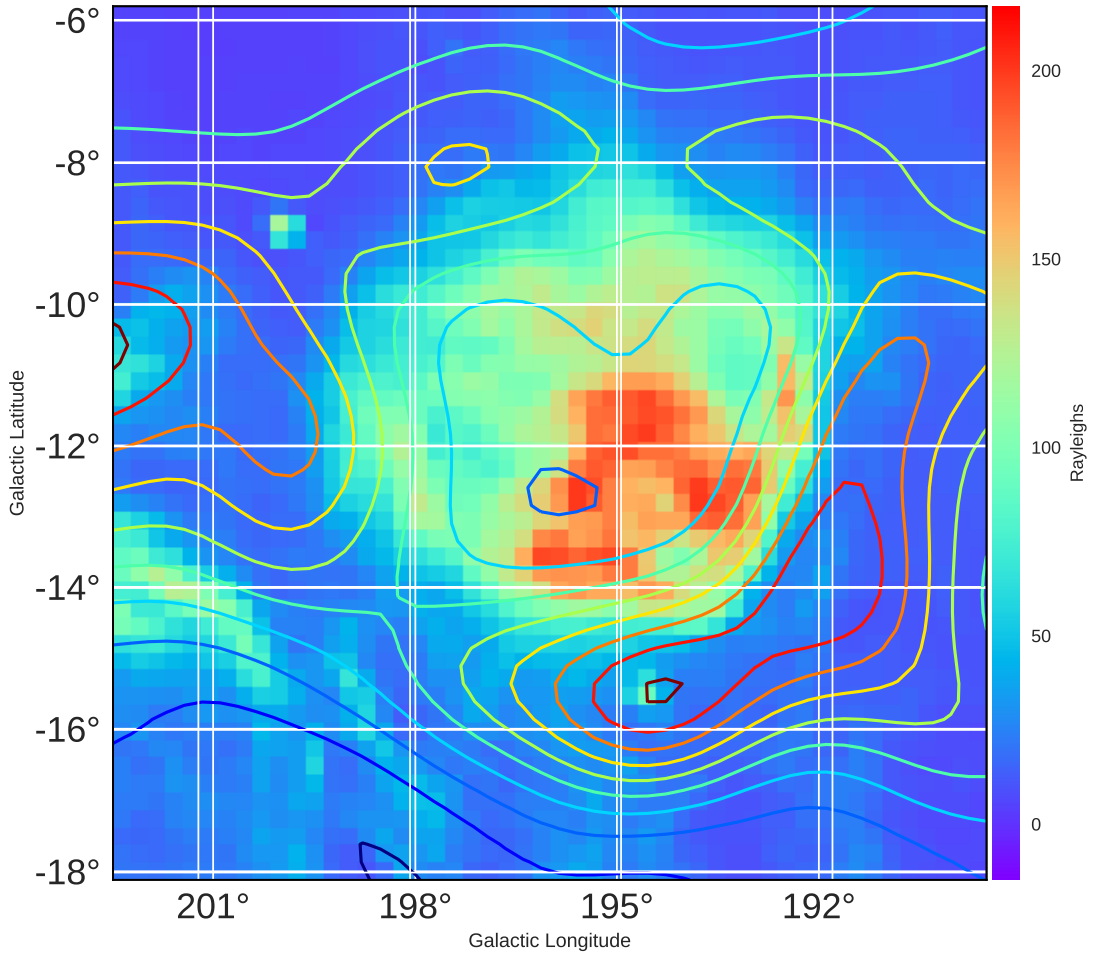
Figure 3.2: λ Orionis as it appears in H-alpha emission by Finkbeiner (2003). Contours indicate AME emission, from the variable frequency component. The colorbar indicates $H\alpha$ emission in Rayleighs. The field of view is slightly larger than that used for the final processed IR comparison (Fig. 3.6).

region, assuming that $H\alpha$ line emission is a tracer of microwave free-free. This indicates that free-free is strong within the central region, where radiation fields are more intense, and AME is minimal. The strongest AME follows the ring-shaped morphology outside the central bubble of free-free emission. We will first show a model-independent analysis, comparing IR photometric intensities from the mid to far-IR to the AME. After comparing all of these intensities, we describe which wavelength shows the best intensity correlation. The core results however will be based on a dust SED model-dependent analysis, which takes into consideration all of the photometric intensities to fit the total abundance of dust, PAH abundance, PAH ionization fraction, and ISRF strength, U, accross the λ Orionis region. We will then discuss the core

result, suggesting that PAH mass has a stronger relationship with AME than the total dust mass does, representing the first time such a result has been found for a specific AME-prominent region.

3.3 Data preparation

As indicated in Ch. 2, we use 12 photometric all-sky maps. For the IRC data (A9 and A18), we produce mosiacs of λ Orionis from the latest version of the individual tiles provided internal all-sky archive. A9 and A18 images are produced by regridding the images with the `Montage` software by NASA/Infrared Processing and Analysis Center (IPAC). Figs. 3.4 and 3.5 show high resolution mosaics of the A9 and A18 data before processing. [1] For the other sources, HEALPix all-sky maps are available publicly, at sufficient resolution relative to their native resolutions[2]. [3][4]

Other data were obtained from publically archived HEALPix maps. This includes data from IRAS, Planck, DIRBE, and AKARI/FIS. For For these data, we employ the `healpix2wcs` functionality provided in the `gnomdrizz` python package[5][6] When the extraction and regridding are finished, all of the images — those extracted from Hierarchical Equal Area Iso Latitude Pixelation of the Sphere (HEALPix) maps, as well as the IRC data — share a common FITS header having a pixel grid spacing equal to the average pixel width in the NSIDE 256 HEALPix scheme, or about ~0.25°. After PSF smoothing, described in detail below, the data also have a common ~1° FWHM effective PSF. Although this means that the grid is oversampled, we choose this approach to preserve as much of the structure of the region as possible, even after masking bad pixels. Another option would be to interpolate the bad pixels, and degrade the pixel scale to the PSF size. However we choose the former method due to the relative large number of bad pixels, especially around the regions affected by missing stripes. This means that in the analyses that follow, what is important is the relative trends between correlation coefficients, rather than their absolute values.

---

[1]IRC all-sky data is still in the proprietary phase at the time of this writing, but should be public by April 2018.

[2]Planck data was retreived from the NASA IPAC online archive at `http://irsa.ipac.caltech.edu/data/Planck/release_2/all-sky-maps/`

[3]AKARI/FIS data

[4]IRAS/IRIS data

[5]Available at `http://cade.irap.omp.eu/dokuwiki/doku.php?id=software`

[6]"drizzlib" 1.2.2 and earlier were not able to correctly access HEALPix files with multiple fields/columns. See appendix for our recommended workaround.
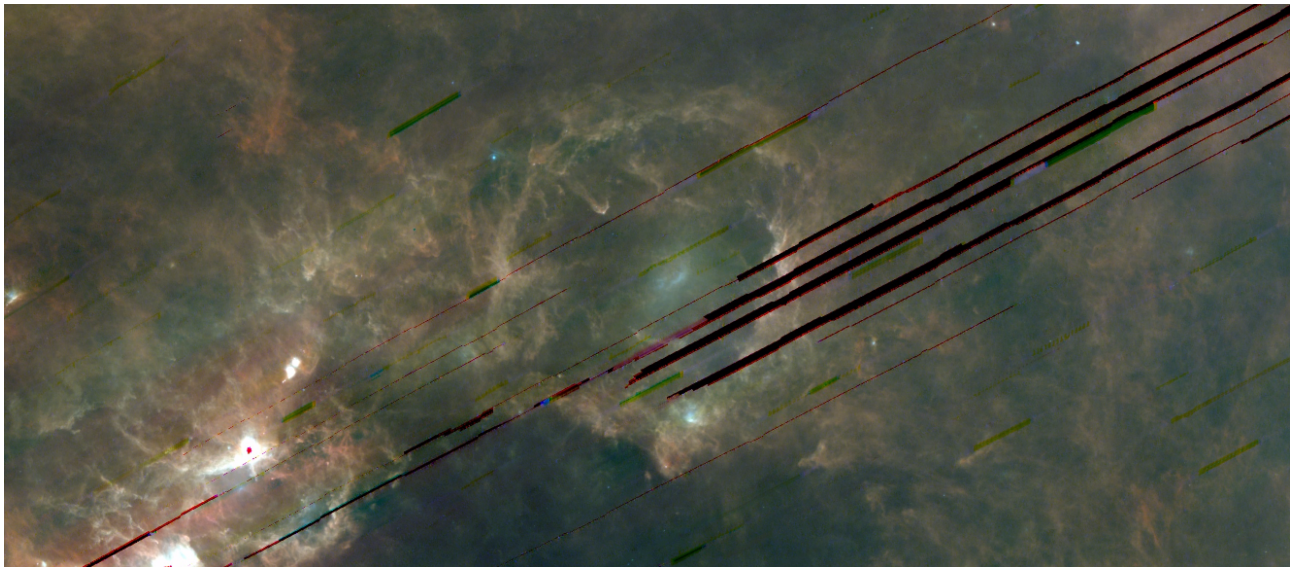
Figure 3.3: The λ Orionis region and its surroundings in AKARI FIS data, where A65 is blue, A90 is green, and A140 is red. The missing stripe patterns are visible, and affect all 3 bands shown here as well as the A160 data.

3.3.1 Point-source and artifact masking

Missing stripes   The AKARI all-sky survey suffers from a few missing stripe errors throughout the IRC and FIS maps (Ishihara et al. 2010; Doi et al. 2015). This is a more serious issue for FIS. Unfortunately for the present work, some of these stripes pass directly through the λ Orionis region. Figs. 3.3, 3.4 and 3.5 display the data at near-native resolution, demonstrating where these patterns occur. Additionally there are some saturated pixels in both IRC and FIS data.

Point sources   A caveat that comes with added ionized PAH feature coverage of the A9 band, is that the shorter central wavelength placement allows more contamination from point sources. We identify point sources with a moving-window approach provided in the astropy Python package, flagging pixels which have higher than 5σ intensity among the surrounding 100 pixel window. We then place a mask at the center of the flagged point-sources. The masks are propogated through the regridding step, such that the low-resolution pixels having more than 50% of their area masked in the high resolution tiles, also become masked. Such pixels appear black in Fig. 3.1. The same process is applied to the A18 data. For other maps, which we extract from HEALPix data, we first regrid from HEALPix to rectangular grids, and then apply the point-source search and masking as above. For the I12 and I25 images, the rejected pixels were fewer than with A9, but positions overlapped with those already masked in A9.
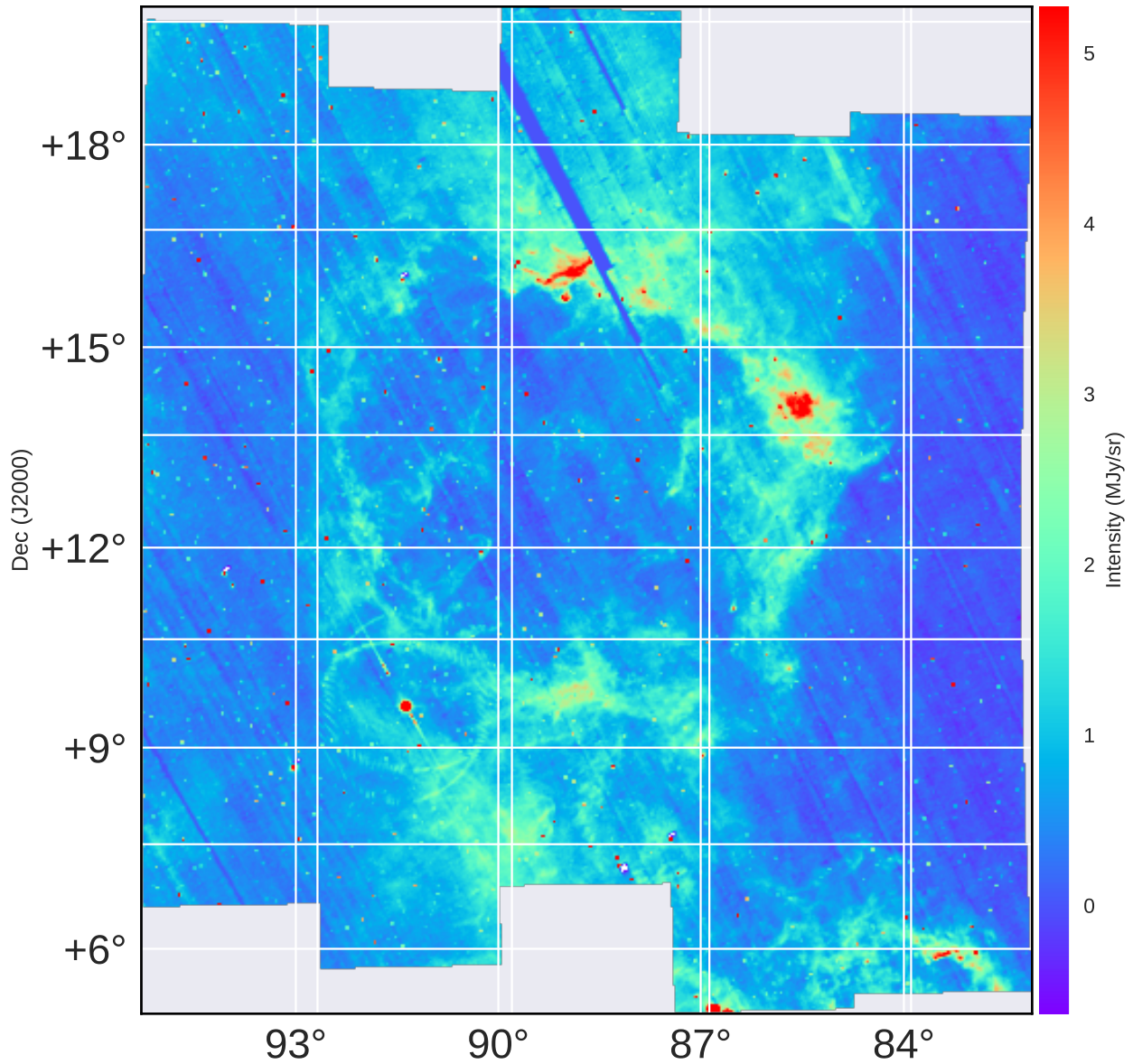
Figure 3.4: The λ Orionis region in the A9 band at near-native resolution. This is a mosiac created from the 3x3 degree all-sky survey tiles by Ishirara et al. (in prep.) Missing stripes are less of a problem than with the A18 band (Fig. 3.5), but point sources are more pronounced. Around Betelgeuse, in the lower left of the image, we can see an artifact caused by scattered light..
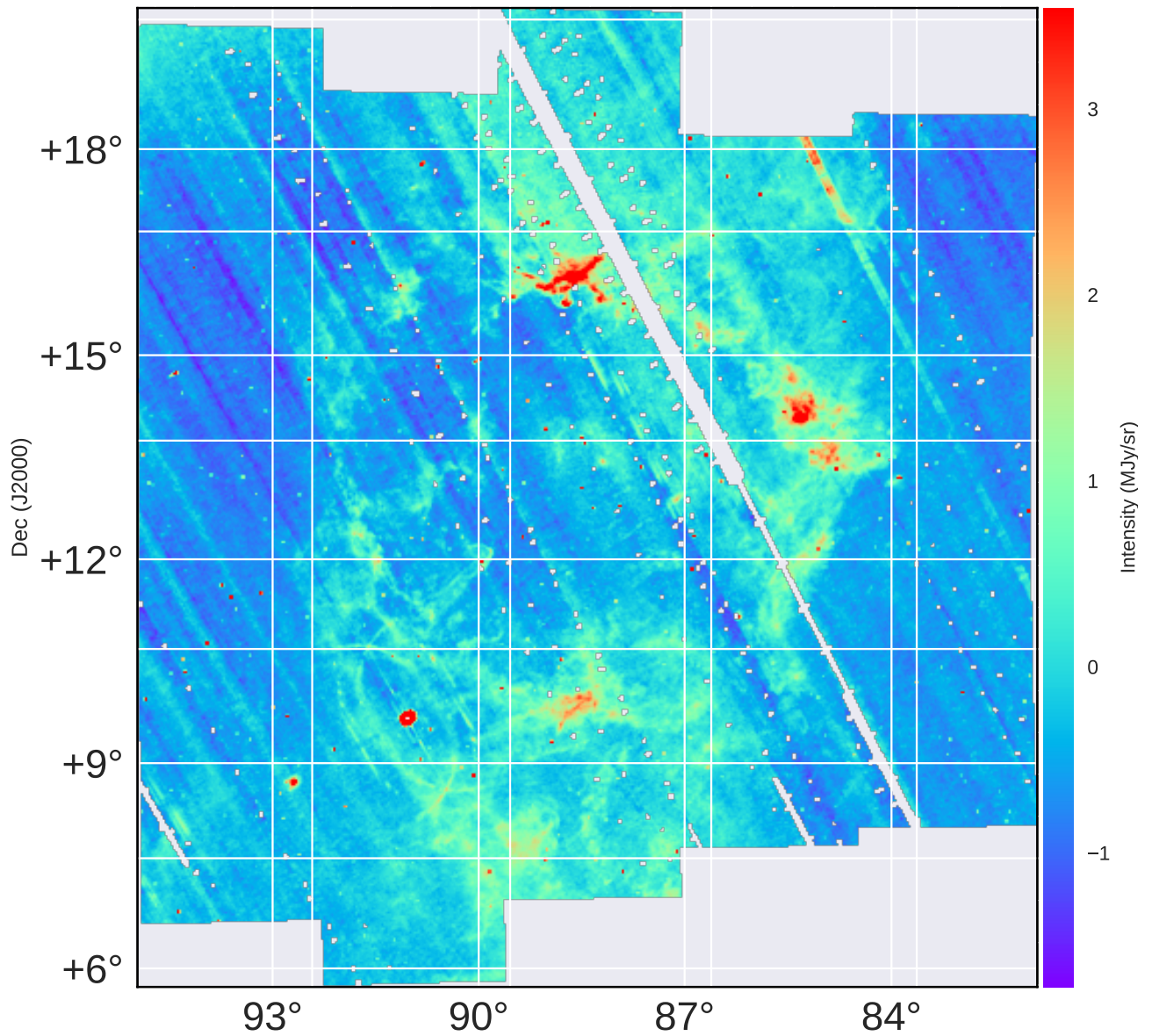
Figure 3.5: The λ Orionis region in the A18 band at near-native resolution, demonstrating the regions affected by missing stripe errors, but less affected by point-sources than A9 (Fig. 3.4).

For bands longer than I25, this process did not result in rejected pixels. For the D12 and D25 bands, which are natively at a much lower resolution than AKARI or DIRBE, point-sources present more of a challenge. For these images, we visually inspect and mask 3 regions with bright point source contamination consistent with the DIRBE beamsize and with point-sources identified in IRAS and IRC images. Pixel positions masked in any single image, are masked in all of the images before the finaly analysis.

3.3.2   PSF Smoothing

We smooth the pixels in the spatial domain, to have a 1° FWHM PSF, in order to have a resolution approximating that of the Planck Collaboration (PC) AME data. The smoothing process relies on the `convolution` module provided in the `astropy` package. We assume simple circular gaussian kernel for the smoothing process. While they may be asymmetries in the effective beam shapes of the IR bands used, the target resolution of the AME data is large enough relative to the native resolution of the input IR data (especially A9 and A18, see Fig. 2.1) as to render the beam shapes and positional variations negligible. Finally, we mask pixels along the edge of the FOV where the convolution process produces artifacts.

3.3.3   Background subtraction

We estimate an average, flat background level for this region. The background level is determined the mean of pixels in an 'OFF' zone. The final images are shown in Fig. 3.6, with the full mask applied (masked pixels are indicated in white), and with the OFF zone indicated by the red rectangle on each frame. We do not expect simple band-by-band intensity correlation tests with the AME to be sensitive to background and foreground emission along the line of sight towards the λ Orionis region. However analyses such as dust SED fitting, to determine the relative abundances of different dust components, may be effected by the background level. The general morphology as seen in the high resolution AKARI data (Figs. 3.3, 3.4 and 3.5) remains well pronounced in the final, low resolution images.
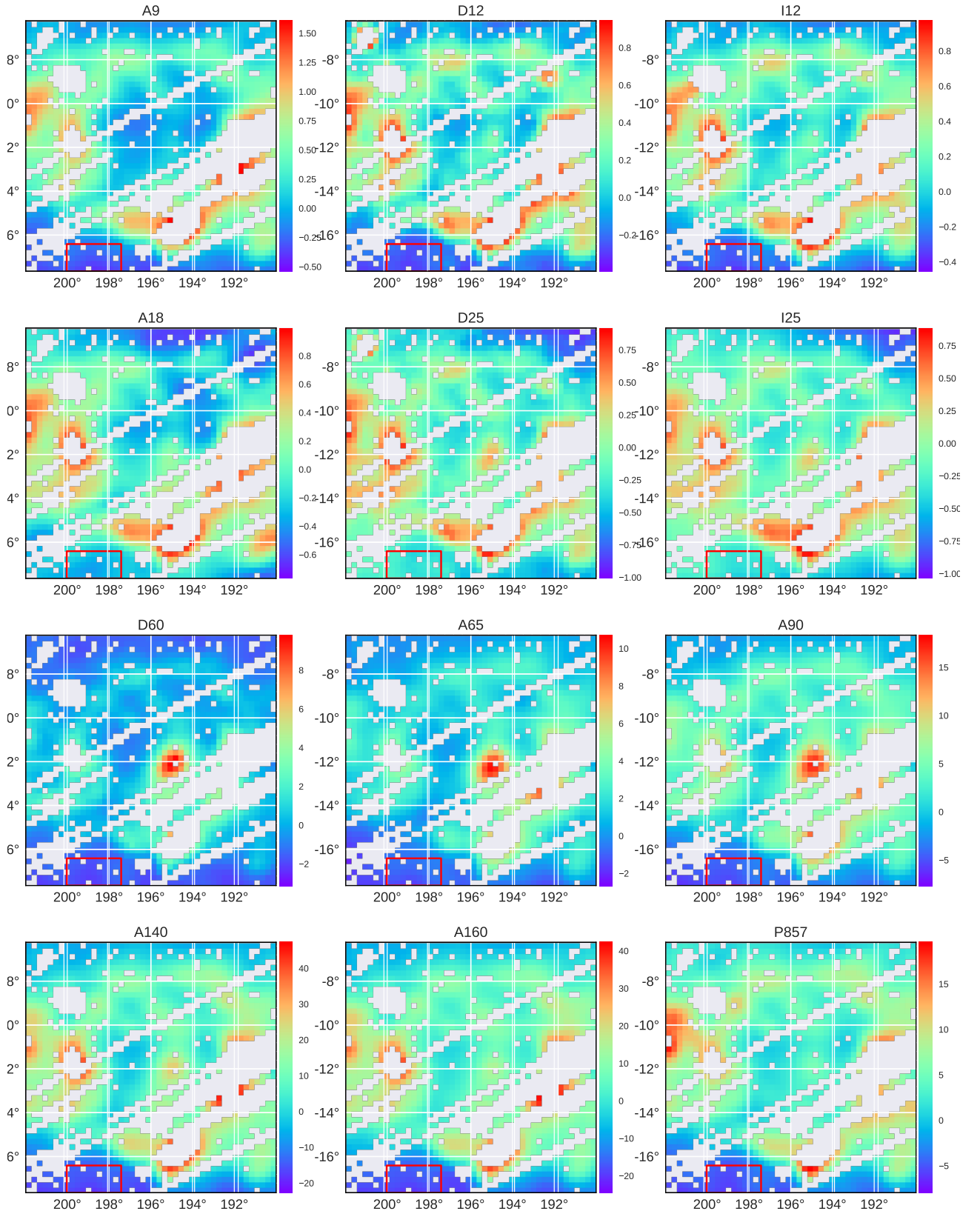
Figure 3.6: Processed data at each wavelength for λ Orionis. A flat background has been subtracted from each frame based on the mean of pixels within the red rectangle. The pixel width is 0.25°, with the data PSF smoothed to 1° spatial resolution. Masked pixels (point sources, stripe errors, convolution artifacts) are shown as white. The frames share the same FOV and GAL-TAN projection. Colorbars indicate the intensity in MJy/sr.

3.4 Multi-wavelength characterization

The correlation matrix results corresponding to data shown in Fig. 3.6, are shown in Fig. 3.7. This immediately confirms a correlation between the IR and AME, however this was readily visibly from the spatial morphology of the region. Interestingly though, the correlation strengths with AME_{var} show a pattern from short to long wavelengths: A9, P857, and P545 show the strongest correlations, with the correlation weaking from A18 to A90, and again strengthening at longer wavelengths. The fixed peak frequency AME_{fix}, which is the much fainter component, shows the strongest correlation with A90- though all of the IR correlations relative to AME_{fix} are weaker than those for AME_{var}. The overall pattern is for bands dominated by PAH emission (as discussed in Ch. 2), and those which trace Rayleigh-Jeans thermal dust emission are equally good predictors of the AME. Bands dominated by a mixture of VSGs, and warm dust emission, show a weaker correlation. For the next stages of analysis, we will consider only the dominant component AME_{var}. We found that combining the components does affect the results here.

Comparing the images in Fig. 3.6, most of the variation in the correlation scores appears to come from the central region of λ Orionis. Because of the known heating present within the ring, from the λ Orionis association, and given the brightening of bands between A18 and A90, this variation appears to be due to a temperature increase.

3.4.1 Bootstrap analysis

To assess the robustness of the correlation scores, we employ the Bootstrap re-sampling approach. We carry out bootstrap correlation tests for each IR band's intensity vs. AME_{var}. The data are resampled 10,000 times for each correlation test, a sufficient resampling given the unmasked pixel count of ~1400 pixels, and considering that the effective beams are somewhat undersampled. The distributions of the boostrap resamplings are shown in in Fig. 3.8. For both test cases, the best correlations are the longest and shortest wavelength bands, consistent with the straight-forward r_s scores shown in Fig. 3.7.

Figure 3.7: r_s correlation matrix for all of the data used in the λ Orionis analysis, similar to that presented for the Planck Commander component maps in Fig. 2.8. The shade and annotation for each cell indicates the r_s score, where r_s of 1 indicates a monotonically increasing relationship for a given pair of images. The two AME components, as described in Ch. 2, are listed separately: AME_{var} for the frequency-varying component, and AME_{fix} for the constant frequency component.
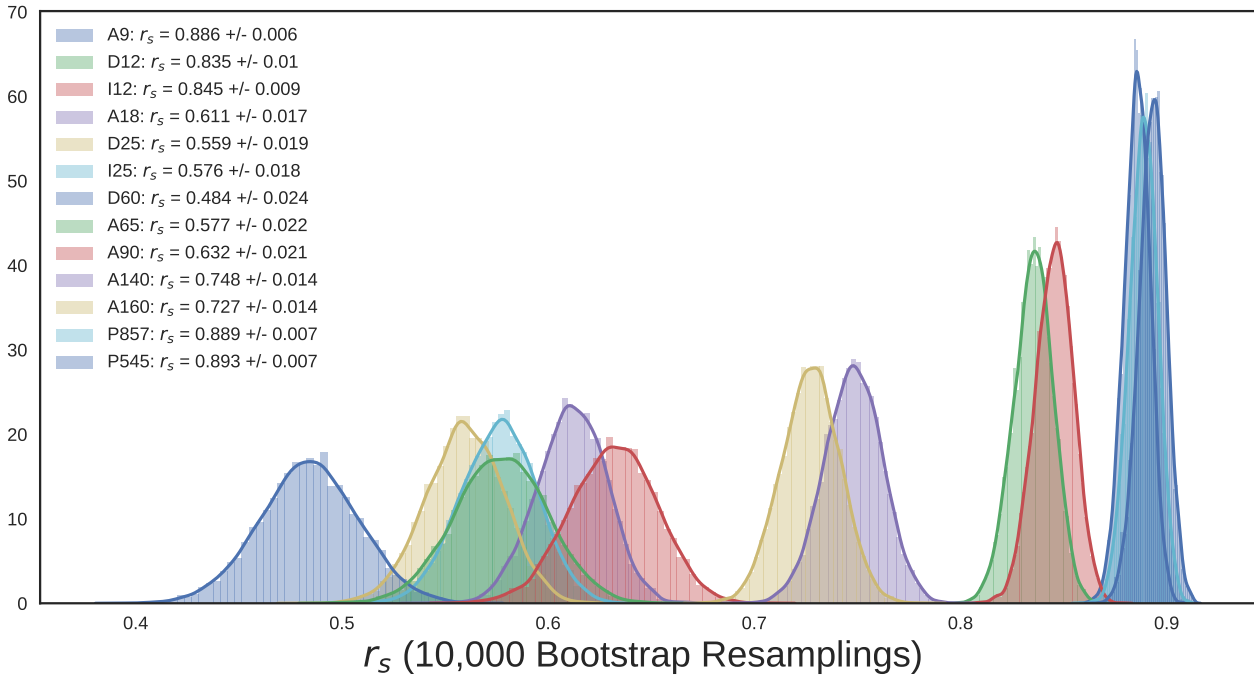
Figure 3.8: Re-sampled (Bootstrap) correlation tests for IR emission in λ Orionis vs. AME. Each band's r_s distribution is shown in a different color (the same color scheme for both plots). The width of the distribution indicates the error for the given data in the correlation coefficient. The mean and standard deviation of the scores are given in the legend of each plot. The plot ranges only show positive values, since no negative scores were produced.

3.5 Comparison with SED Fitting

We performed a full dust SED fitting on the λ Orionis photometry, according to the dust model by Galliano et al. (2011), and the hierarchical Bayesian SED fitting framework by Galliano (2018). There are 4 free paremeters: total dust mass M_{dust}, fraction of dust mass as PAHs q_{PAH}, the fraction of PAHs that are ionized, and the average strength of the ISRF U. As indicated in Ch. 1, we implement such an analysis here primarily because it allows a more careful propgation of the observational errors. We utilize both the HB approach and a least-squares analysis. The HB approach allows us to accurately propogate errors in the data (including calibration uncertainties) through the SED fitting process, as well as the correlation test thereafter. Compared to the ubiquitous LSM In traditional SED fitting we often assume only Gaussian uncorrelated noise. Even if this were a valid assumption for the raw data, processing steps may induce correlations or skew noise. Induced correlations may also appear in the parameters fit via standard approaches, when environments are mixed along the line-of-sight (Shetty et al. 2009).

We used a mixture of silicate and carbonaceous dust, silicate dust, the two dominant cate-

gories of interstellar dust as described in Ch. 1. However, instead of the graphite-based carbon dust invoked by the canonical Draine & Li (2007b) model (DL07), we assume amorphous carbon. This is an attempt to account for an excessive dust-gas-ratio, reported by Israel et al. (2010); Bot et al. (2010) in the Large Megellanic Cloud (LMC), which was found by Galliano et al. (2011) to violate elemental depletion constraints. The increased opacity of amorphous carbon (a factor of 2-3 more than DL07) allows a better fit to Herschel observations of the LMC (Galliano et al. 2011), and Planck observations of the Milky Way (Planck Collaboration et al. 2016d). We assume that the radiation field heating this dust mixture takes the profile of the typical Galactic ISRF in Mathis et al. (1983).

We only carry out the fitting for unmasked pixels. We are primarily interested in which of the corrleations M_{dust} vs. I_{AME} or M_{PAH} vs. I_{AME} is stronger.

Two sample SED fitting results are shown in Figs. 3.9, and 3.10. Performing such fits for all of the pixels, we are able to see how I_{AME} varies with the dust properties of the region. Fig. 3.11 shows the fitted dust mass per pixel, relative to the AME intensity. AME intensity is scaled by the ISRF intensity U. Although spinning dust emission is not predicted to vary directly with U, we consider that the ISRF may serve as a diagnostic of environmental conditions in the ISM. In any case, we find that performing such a scaling improves the correlations with dust mass. Figs. 3.12 and 3.13 describe the variation with M_{PAH} and M_{PAH+}. Based on the dust properties derived from these SED fits, we investigate whether any fitted parameter shows a preferential relation with the AME. Figs. 3.11-3.13 reveal a very similar trend between the AME and the parameters M_{PAH}, M_{PAH+}, and M_{dust}. There is a slightly improved correlation between M_{dust} and M_{PAH} (0.857 vs 0.867). This is consistent with the intensity cross correlations in Fig. 3.7. These corrleations are discussed further in Sec. 3.6 and Fig. 3.14.

3.5.1 Comparing the Correlation Strengths

In addition to probability distribution functions of the fitted parameters, HB allows us to plot the final PDFs of the correlation coefficients themselves. This is a more robust way of comparing the correlation strengths than simply bootstrapping the correlations. Fig. 3.14 shows the r_s PDFs for the 3 major correlations of interest: $r_s(I_{AME}, M_{dust})$, $r_s(I_{AME}, M_{PAH})$, and $r_s(I_{AME}, M_{PAH+})$. To assess the effect of the morphology of λ Orionis on these results, we show the same PDFs but omitting the central region of λ Orionis. This is shown in Fig. 3.15.
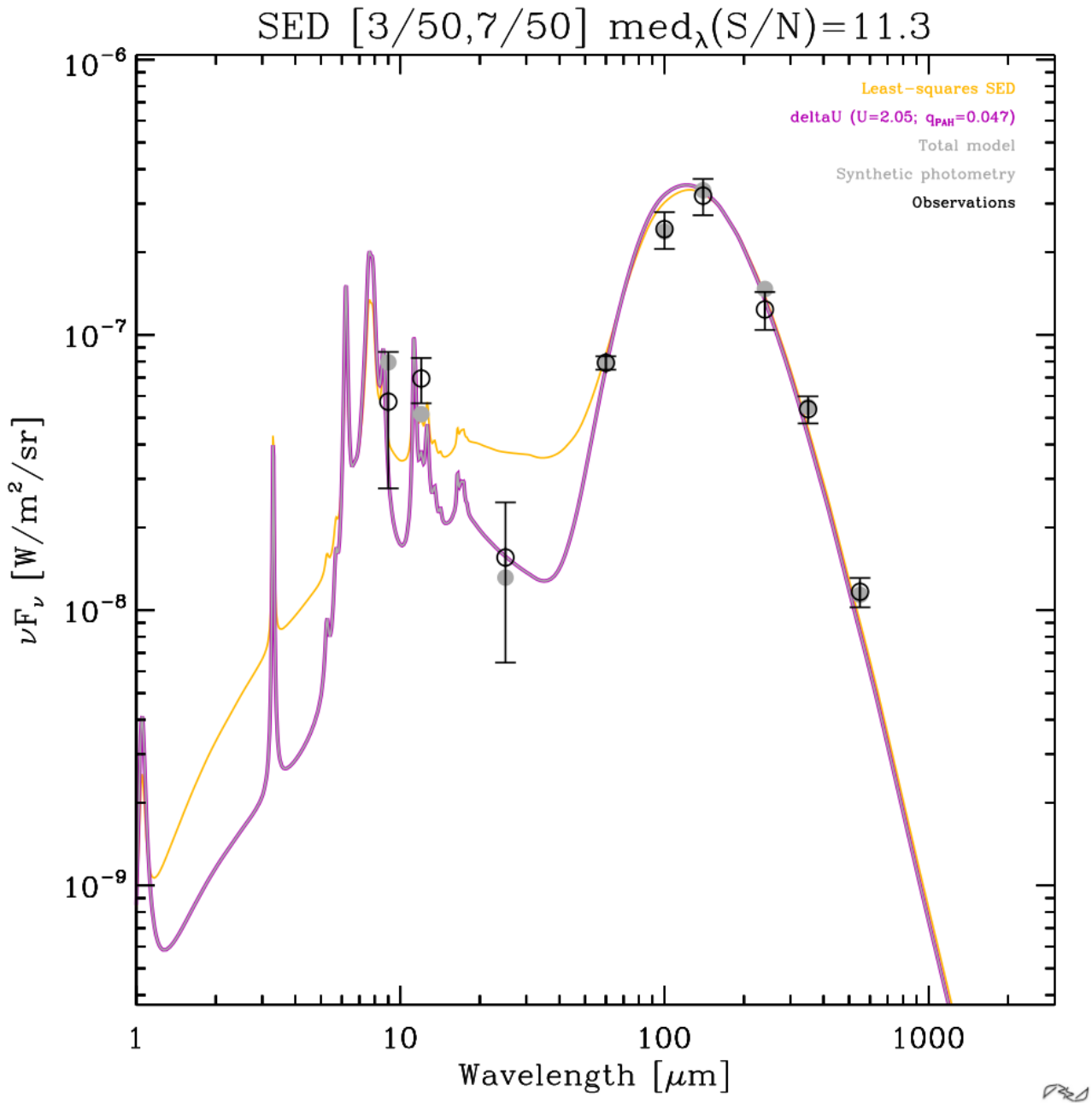
Figure 3.9: Observed (black circles and errors) and synthetic photometry (gray dots) SED of a pixel within λ Orionis, along with the dust SED model fit results. Two SED fits are shown: on for the Bayesian fitting (magenta), and another showing the standard least-squares result for comparison (yellow). The fitted ISRF strength U, and fraction of mass in PAHs, q_{PAH} are also given.
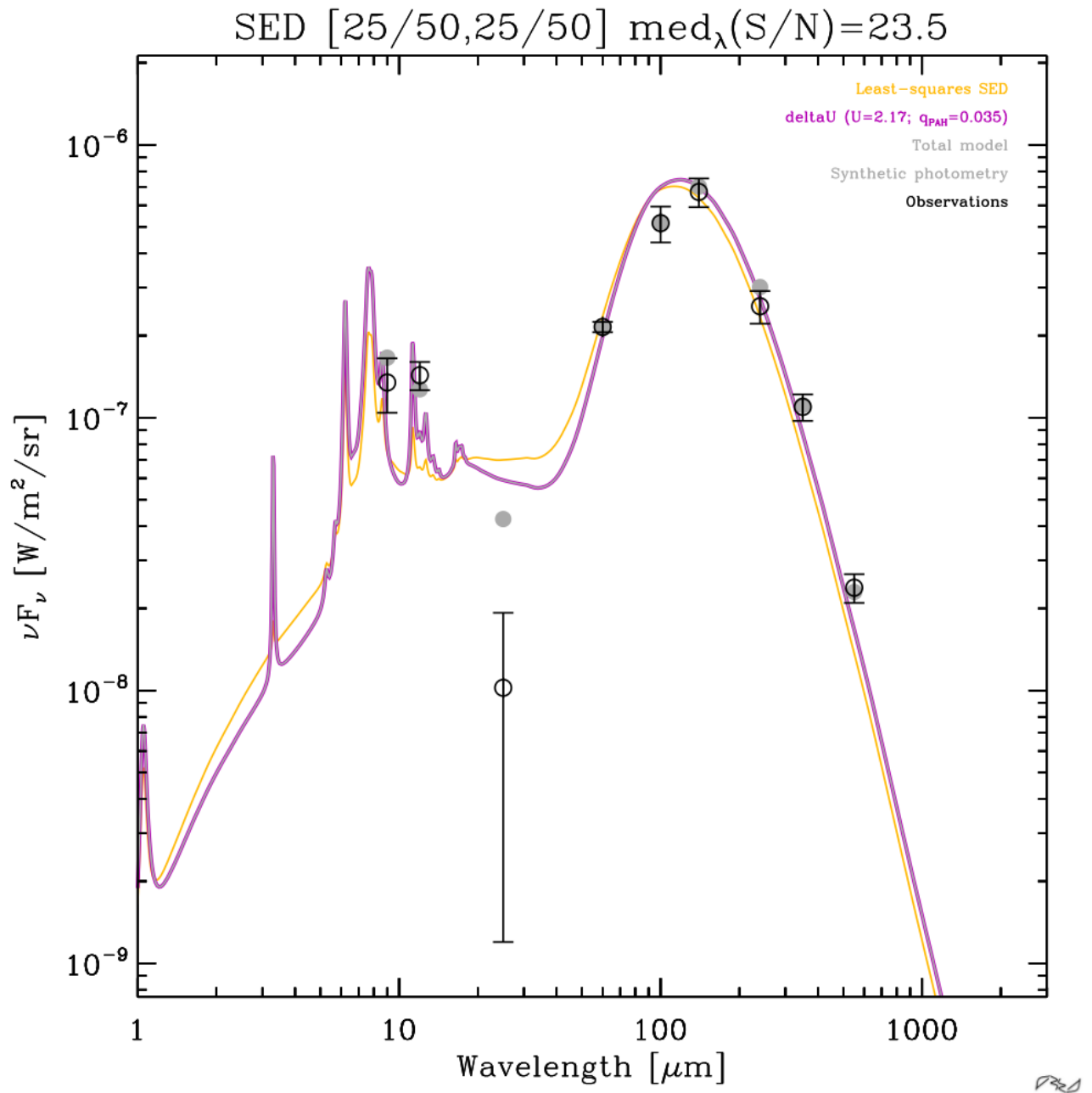
Figure 3.10: The same as Fig. 3.9, but for a different pixel position.
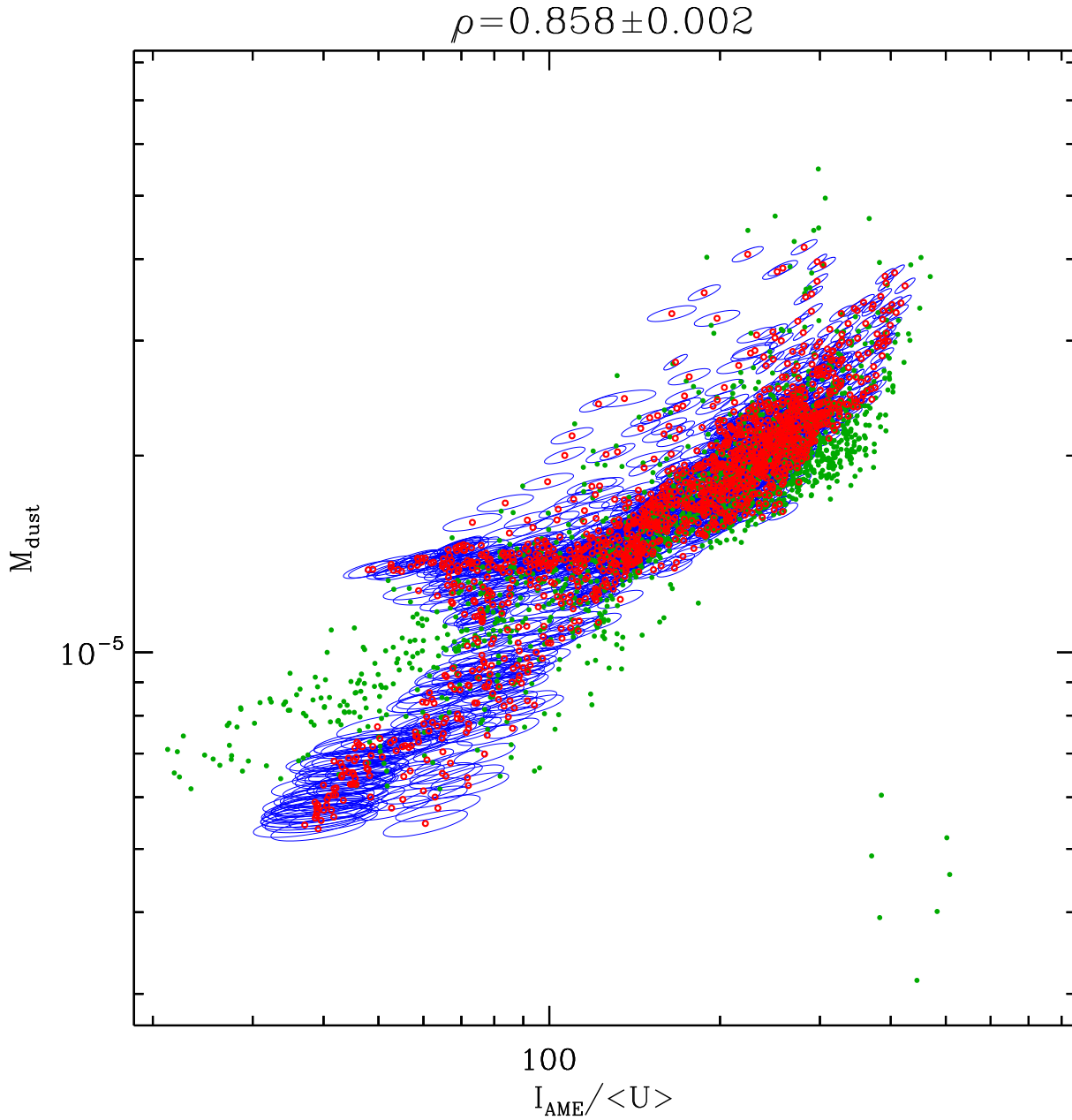
Figure 3.11: Scatter plot with the bivariate error elipses generated through the HB SED fitting, of total dust mass M_{dust} vs. I_{AME} scaled by U. Green dots indicate the results when using a simple least-squares method fit, for comparison with the HB method.
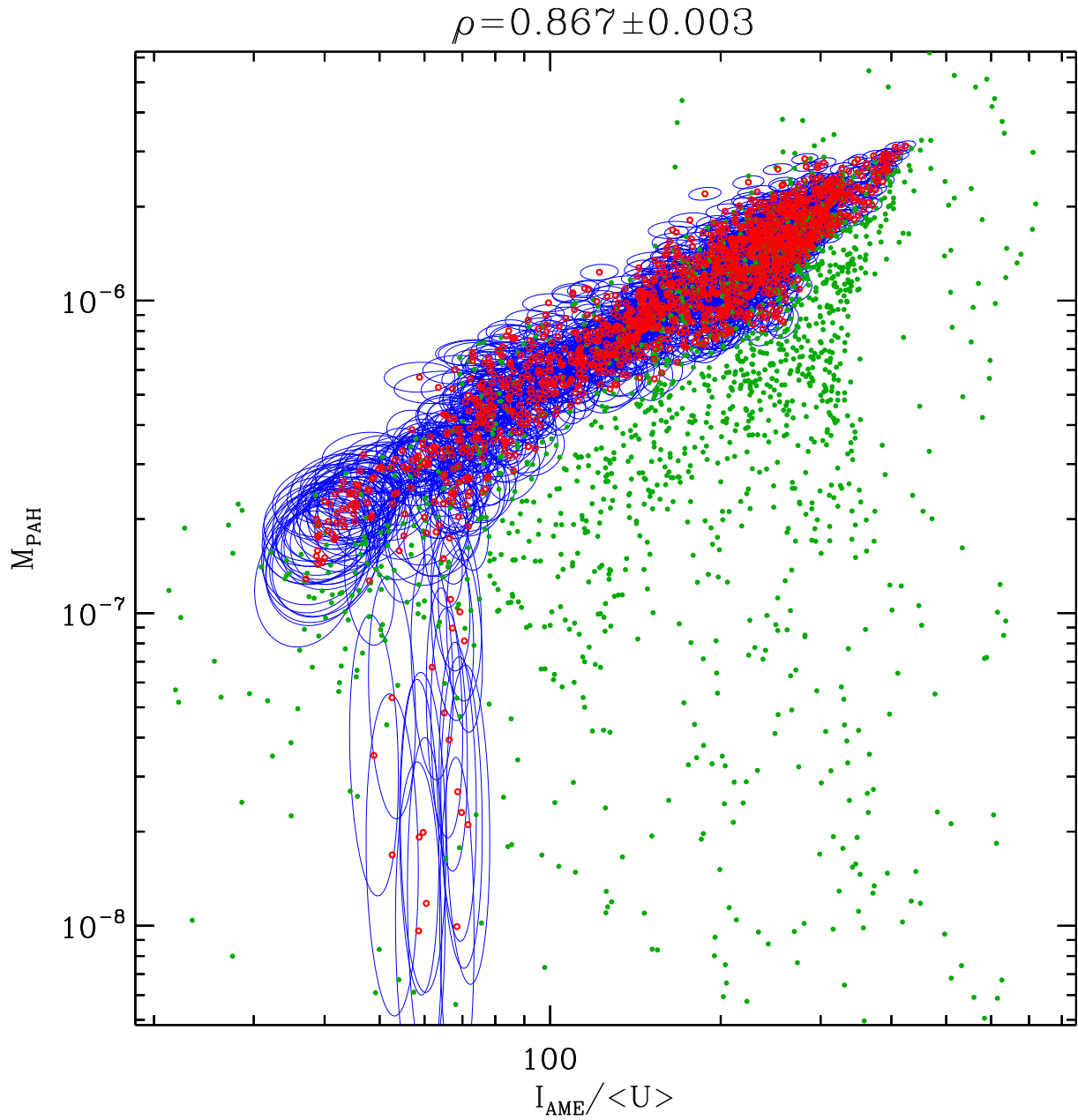
Figure 3.12: The same comparison is given by 3.11, but showing total mass of PAHs (M_{PAH}) rather than total dust mass on the y-axis.
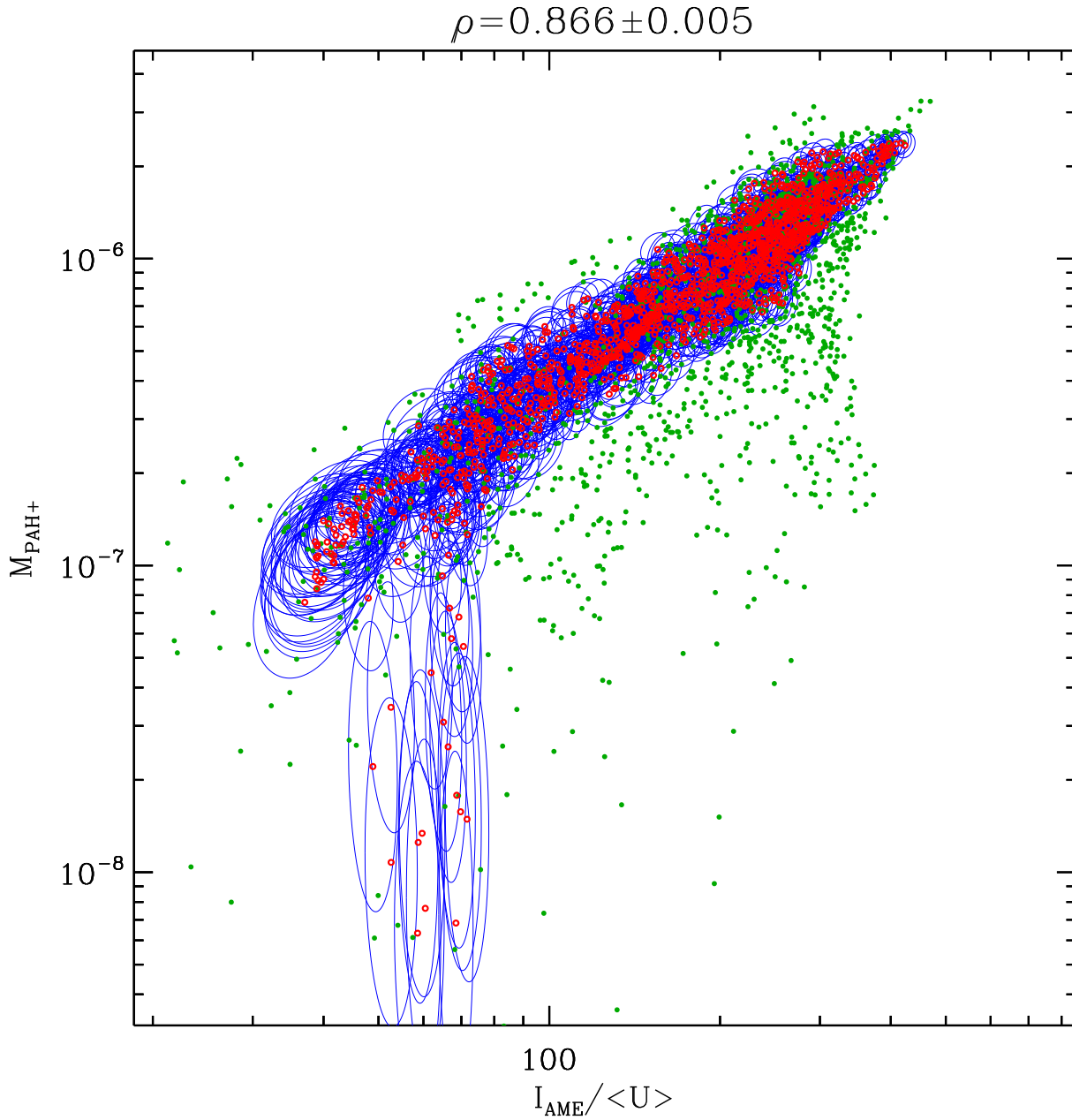
Figure 3.13: The same as in Figs. 3.11 and 3.12, but specifically comparing an estimate of the charged component of PAH mass M_{PAH+}. This includes anions and cations, since we cannot distinguish between these two spectroscopically.
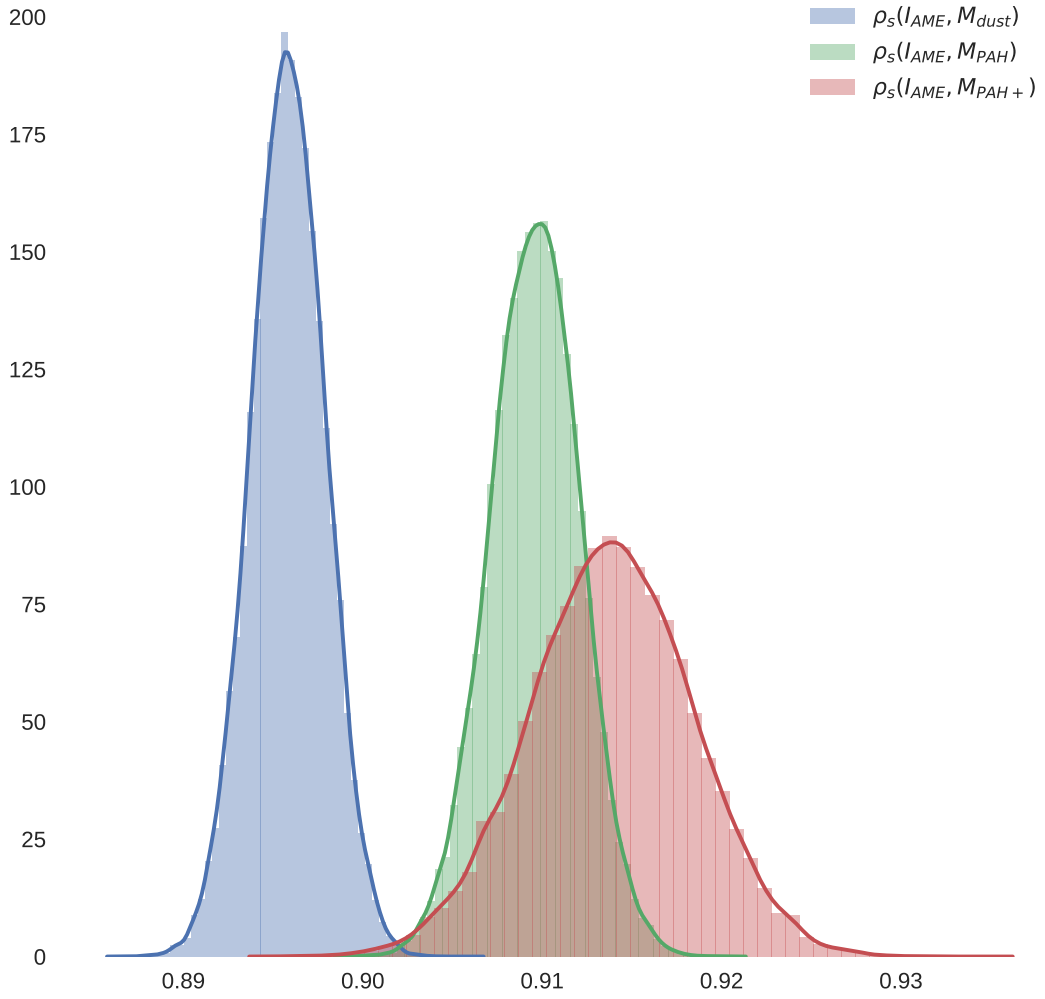
Figure 3.14: The hierarchical Bayesian correlation probablity distributions of r_s) for the three physical parameters vs. the AME intensity: total dust mass, $r_s(dust)$ (blue); total PAH mass $r_s(PAH)$ (green); and only the ionized PAH mass $r_s(PAH+)$ (red). Also given are the probabilities of either PAH component being better correlated with AME than dust mass, as well as the probability that ionized PAH mass correlates better than total PAH.

The extent of the mask is indicated in Fig 3.16.

3.6   Discussion

In λ Orionis we found that accross the whole region, A9 emission and P545 emission were the most strongly correlated with AME. This is apparent both in the photometric band analysis, and in the dust SED fitting. The fact that the correlation strengths of PAH-tracing mission and sub-mm emission are similar is in-line with what we have seen in Ysard et al. (2010) and Hensley et al. (2016). In those works, the two relationships (MIR vs. AME and FIR vs. AME) are very close, although these two papers are odds as to which relationship is stronger, and thus in their final interpretation. With the present data and analysis of λ Orionis, we fail to rule out PAHs as carriers of the AME. In fact, our primary result, shown in Fig. 3.14 indicates that PAH mass is a stronger predictor of the AME, compared to the total dust mass. This is the first time such a significant result has been found, in support of the PAH hypothesis for a particular region. This core result is unchanged even when we examine the outer ring structure separately from the central region, as shown in Fig. 3.15.

The results are consistent with a scenario in which PAH mass, cold dust, and the AME are tightly correlated. A correlation between cold dust and PAHs is observed in extragalactic targets (Haas et al. 2002), and may be inferred from the correlation between unidentified Infrared bands (UIR) and FIR emission reported in diffuse galactic ISM (Onaka et al. 1996). In the case that AME emanenates from spinning PAHs, it is not surprising that cold dust would also correlate with the AME. Weaker correlation from 25 to 70 μm may indicate that AME is weaker in regions of warmer dust and stronger radiation fields. Such an anti-correlation with harsher radiation are consistent with the carriers of AME being destroyed in the central region of λ Orionis, thus leading to substantially decreased spinning dust emission.

3.6.1   Performance of the Hierarchical Bayesian Fitting

Indicated in Figs. 3.11, 3.12, and3.13, the trends described in this chapter between dust mass and PAH mass, and the AME intensity were revealed through the HB analysis. The increased scatter of best-fit points, produced by the least-squares analysis, obviously obscures the intrinsic relationships. With only LSM results, the dust SED fitting comparison would have been
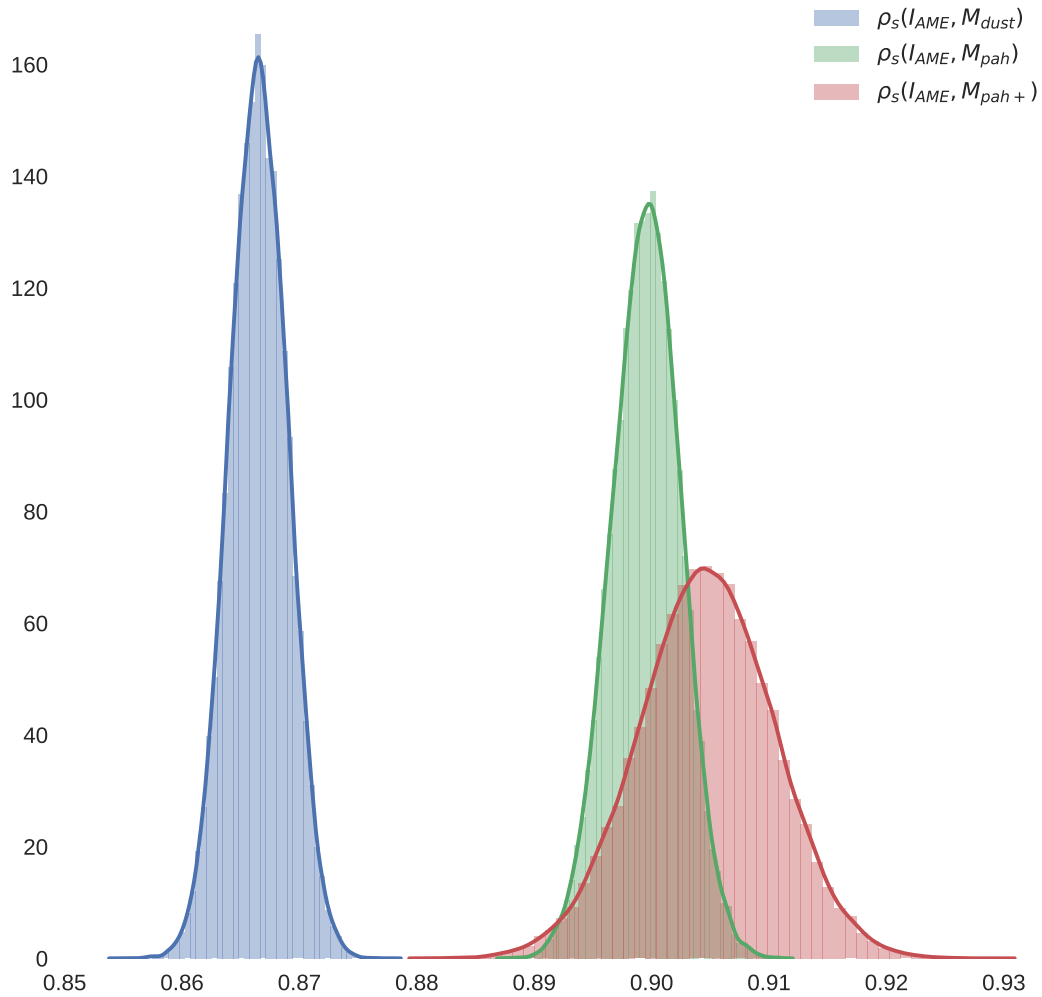
Figure 3.15: The hierarchical Bayesian correlation coefficent (r_s as shown in PDFs as shown in Fig. 3.14, but with the central region of λ Orionis masked, according to Fig. 3.16.
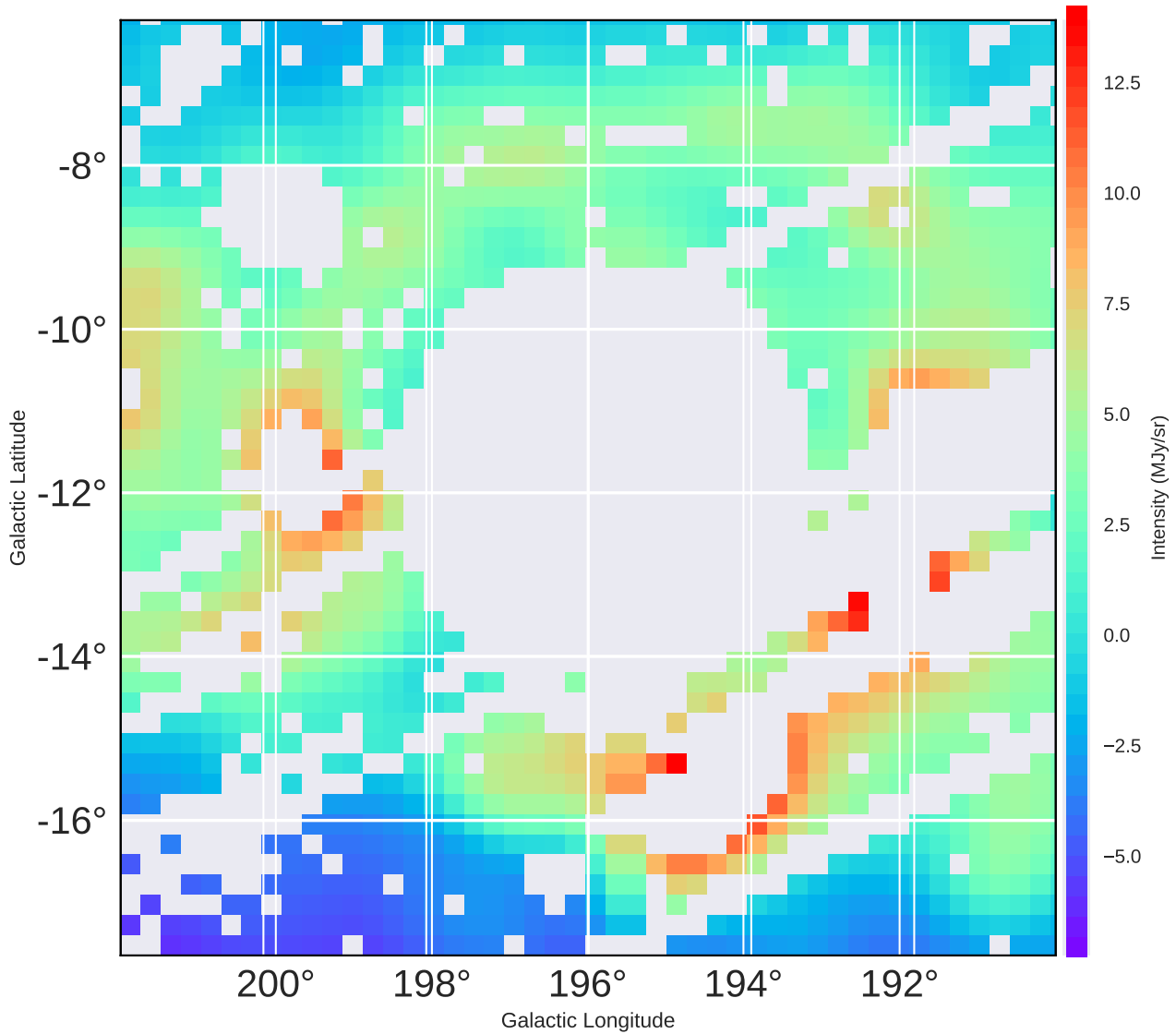
Figure 3.16: The A90 image of λ Orionis shown to demonstrate the mask applied to the central region, in order to produce the PDFs in Fig. 3.15. The region showing an apparent dust temperature peak, which was most prominent in the A90 image and the major point of variation accross all the wavelengths, is thus omitted.

inconclusive. To our knowledge, this is the first case of the HB approach being applied to a localized investigation of AME, and certainly the first time that the dust SED of λ Orionis region has been investigated in such a way. This raises questions about the future of LSM-based analysis in dust SED studies, and highlights the potential this HB framework developed by Galliano (2018).

3.6.2 PAH Ionization fraction

As described in Ch.2 it is expected that relative variations between the A9 and I12 intensities could be explained by the fraction of PAHs that are charged, $fPAH+$. Spectroscopically, we cannot distinguish between PAH anions or cations. However if spinning dust emission arises from anions, a better correlation with the mass of charged PAHs M_{PAH+} is expected. However if the PAHs are positively charged, a stronger correlation with M_{PAH+} is not expected. This is due to the rotational excitability of the PAHs: anions are more succeptable to rotational excitation by H^+ and C^+ collisions(Ali-Haimoud 2010).

Examining λ Orionis in intensity, we find that the A9 intensity correlates more strongly with AME than I12 or D12. In the r_p case, A9 correlates more strongly with AME than any other band. This is consistent with the spinning PAH hypothesis, and taken alone may indicate that the 6.2 μm feature emission from charged PAHs, may be a better predictor of AME intensity.

As shown by the dust SED fitting however, the probability distributions (Fig. 3.14) of $r_p(M_{PAH+} : I_{AME})$ do not indicate that ionized PAH mass correlates better with the total PAH mass. Attempts to estimate the M_{PAH+} based on the available data appear to only add noise relative to $r_p(M_{PAH} : I_{AME})$. The means of the two distrubtions $r_p(M_{PAH+} : I_{AME})$ and $r_p(M_{PAH} : I_{AME})$ are similar and $r_p(M_{PAH+} : I_{AME})$ shows a wider distribution. Thus the question of whether or not AME comes predominantly from charged PAHs remains open.

The fact that A9 correlates more strongly than the 12 μm bands, at least suggests that this topic is worth further investigation. What is clear from the MIR and AME morphology however, is that there is a transition from a relatively PAH depleted, warmer, stronger ISRF in the centerand warm dust in the center to a PAH-supporting region in the ring. Along this transition, there must be a decreasing radiation field with distance from dimnant heating sources, in λ Orionis association. Andrews et al. (2016) predict a transition of PAH species along such a radiation field gradient, from complete PAH destruction in harsh environments,

to survival of (sufficiently large) PAH anions near the surface of molecular clouds. Thus if our stronger correlation with A9 indicates charged PAHs, this could be consistent with PAH anions surviving in the portions of λ Orionis which are emitting the strongest AME. Future wide-area spectral mapping of the λ Orionis region may be able to conclusively test for increased $fPAH+$ in regions with stronger AME. This would also help us to understand the extent to which [NeII] emission may contribute to the I12 emission, and if this may lead to a relatively improved correlation between AME and A9. Such studies would be strongly aided by higher resolution probing of spatial variations the AME spectral profile.

Chapter 4

All-sky Analysis

What we present here is a test of the generalizability of results from Ch.3, which focused on a particular structure on the sky, λ Orionis. We first would like to note that "all-sky analysis" can be a bit misleading. The term tends to lead readers to the idea of a definitive study, answering a particular question for any given position on the sky. While a truly all-sky analysis would be ideal, signal-to-noise constraints (mainly at high galactic latitudes), as well as confusion along the line of sight (mainly in the galactic plane), make a uniformly powerful study of the whole sky very challenging. Here we will indeed show results for the entire sky as a benchmark analysis, but for the core analysis we must mask certain regions dominated by systematic effects in order to minimize biases for particular wavelenghts.

4.1 Resolution matching

Smoothing

As in Ch. 3, this approach applies to a spatial resolution of approximately ~1°. The resolution limimtation is imposed by the PC microwave component maps, which list an effective resolution of 60′ (Planck Collaboration et al. 2016b). Thus we must apply a smoothing to most of our input datasets, which have native resolutions of a much finer scale (see Tab. 2.1 and Fig. 1.2). The data also come in a wide range of beam shapes with their own degrees of uncertainty, thus we conservatively smooth all of the data in the same way, using a circular Gaussian beam, to have ~1° FWHM resolution. We start with an all-sky AME to IR comparison, looking for global patterns among all pixels.

Table 4.1: Monopole values subtracted from all-sky HEALPix maps

Map	Monopole [MJy/sr]
A9	2.27
A18	5.10
A65	1.96
A90	3.13
A140	4.64
A160	4.65
I12	1.00
I25	1.79
I60	0.77
I100	3.04
P857	1.92
P545	0.68

Offset correction

In Ch. 3, we utilized the latest available version of the AKARI/IRC data. However, the latest version is still undergoing final processing for some parts of the sky, at the time of this analysis. Thus we must use a previous version for this all-sky analysis. The major difference between the previous version, and that used in Ch. 3, is an apparent all-sky positive offset of ~2 MJy/sr for A9 and ~5 MJy/sr for A18. We assess this offset first by finding the mode of each of the 4,737 3° × 3° tiles of the IRC survey, for each band, and then taking the mode of that distribution. This distribution of tile modes is shown in Fig. 4.1. We then compare this result with a monopole offset fit to the all-sky HEALPix map of the IRC surveys, built from these tiles. Monopole fitting is handled by the `healpy.fit_monopole` function. The monopole values subtracted from each map shown in Tab. 4.1.

We find the values produced by these two methods to be consistent. We found offsets also in the IRAS, FIS, and HFI bands, thus we apply the same monopole fitting and subtraction to all of the all-sky maps. We do not find the correlation analysis presented in later sections to be sensitive to this offset correction.

4.2   All-sky cross correlations

In order to look more closely at how the AME to IR relationship varies with wavelength, we first do a comparison without applying any pixel mask, as a benchmark. Fig. 4.2 shows the pixel-
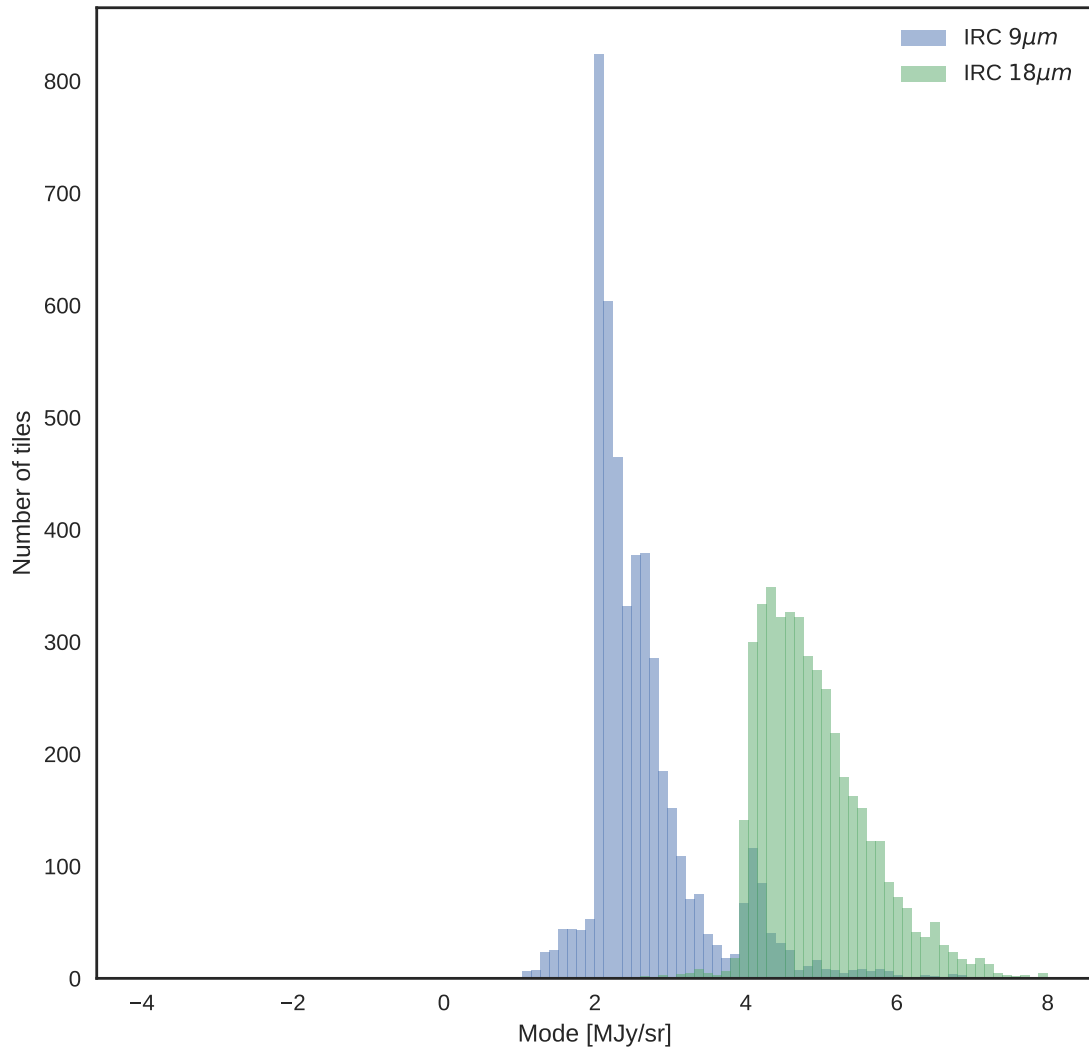
Figure 4.1: Distributions of the modal values for each of the 4,737 survey tiles for the A9 band, and for the A18 band.
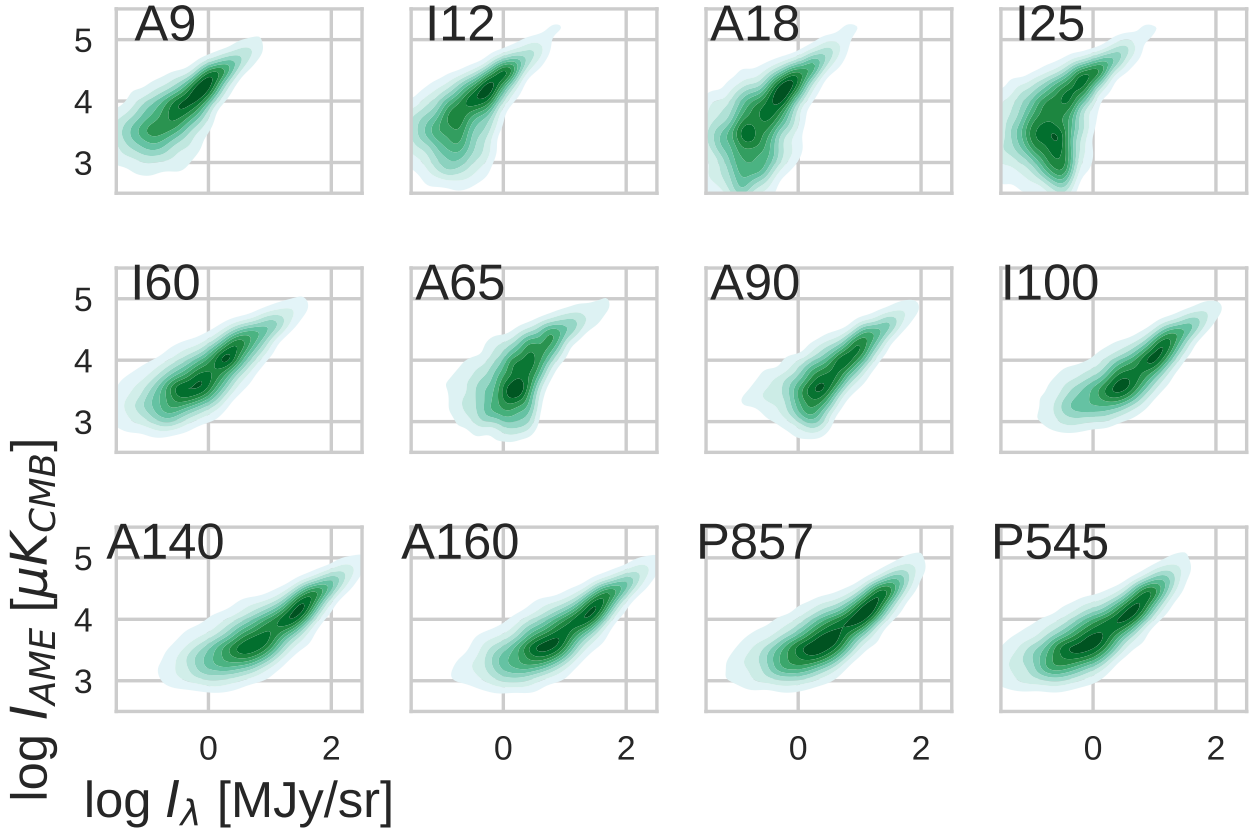
Figure 4.2: Point-density distributions of the log AME_{var} intensity (Y-axis) vs. log IR bands' intensities. In this case no pixel mask is applied, in order to show overall trend of the full data-set. However a random sampling is used due to computational contraints. The plots show a random set of 20% of the full-sky data. Darker shaded regions indicate a higher density of pixels.

density plots of AME vs. the IR bands' intensities. Darker regions show higher pixel densities, unshaded or more lightly shaded regions show low or zero pixel densities. An intial analysis, considering only the interreations of the PC parameter maps, was presented in Sec. 2.4, wherein correlations between the major microwave component maps (synchrotron, free-free, AME, and dust emisison) are demonstrated (Fig. 2.8). This section extends that analysis, considering the full range of IR maps described in Tab. 2.1.

We see immediately that each band shows evidence of a positive trend with AME intensity. For the MIR bands, at lower IR intensities we see the effects of detector noise become dominant, turning into a more defined positive trend with increasing IR intensity. This effect is less pronounced in the FIR. The trend is similar to that found in Ch. 3, and Fig. 3.7. We consider that the IR maps used must not only be compared to the AME, but to each other, to assess multi-wavelength patterns. We also compare the AME and IR maps to ancilliary maps, as described in Ch. 2 and Tab. 2.2. Fig. 4.3 confirms the weaker trend in the MIR vs. AME, via
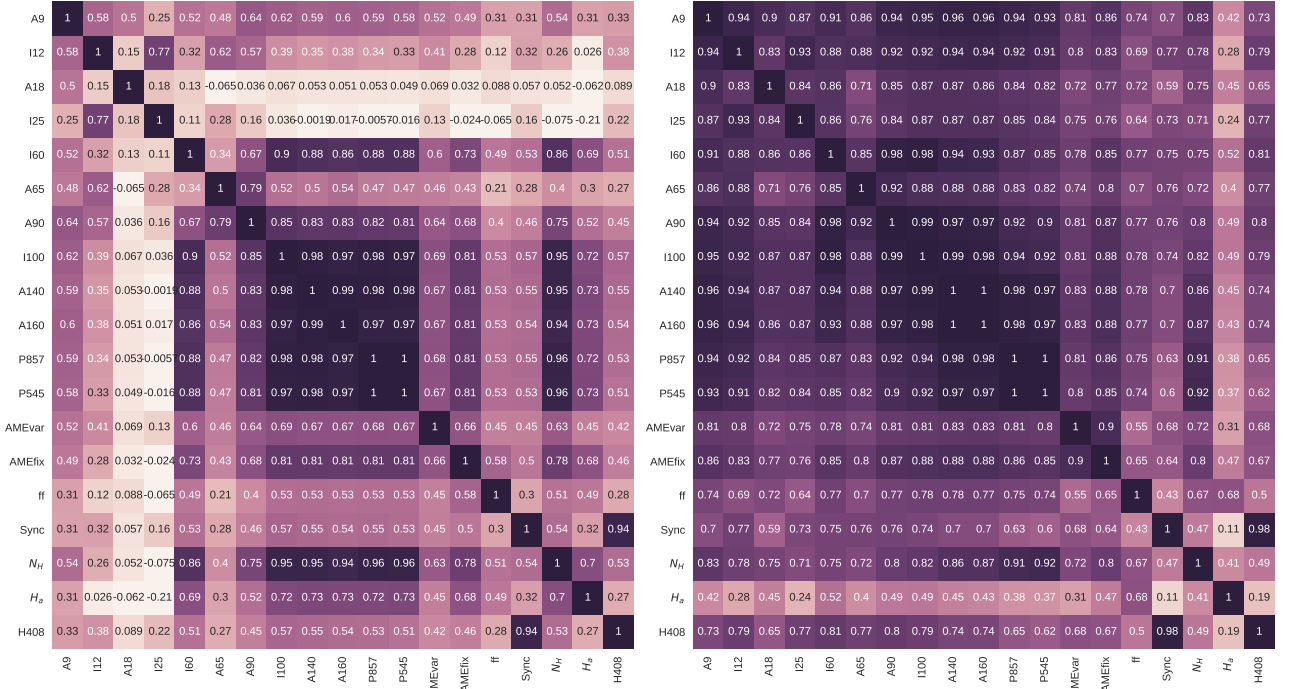
Figure 4.3: ALL-SKY cross-correlation matrix for the 12 infrared bands sampled, as well as the PC component maps described in Ch. 2: the two AME components evaluated at their peak frequencies AME_{var}, AME_{fix}; Syncrotron, and free-free), and ancilliary maps of N_H, $H\alpha$ emission, and 408 MHz emission Haslam et al. (1982). The color-scale indicates (r_S). Results are based on the unmasked sky, but are split by Galactic latitude: pixels with $|\beta| > 15°$ (left) and $|\beta| < 15°$ (right). The color and annotations indicate r_s as in Fig. 3.7.

a cross-correlation matrix, similar to that used in Ch. 3 and Fig. 3.7. This is reflected in the comparison between high and low latitude plots: for pixels $|\beta| > 15°$, we see a dramatic effect. In the most extreme case r_s of A18 to AME_{var} drops from 0.72 at lower latitudes, to 0.02 at higher latitudes. $r_s(A9 : AME_{var})$ drops from 0.79 to 0.42. Correlations between the MIR bands and FIR bands also weaken. Only the the interrelations between the FIR bands from I60 to P545 remain essentially latitude independent (with the exception of A65, which has an especially high noise level.)

In the lower latitudes, with $|\beta| < 15°$, bright emission in and around the galactic plane seems to homogenize the bands. We see little change from band to band both in terms of the relationship with AME or with other IR bands. Thus the increase of S/N with decreasing brightness at higher latitudes has a strong effect on such intensity correlation tests. Bands tracing bright thermal dust emission at higher latitudes are more robust against this effect. The only case where the trend is reversed, is with the maps of $N(H)$ and $H\alpha$. Both of these maps show higher r_s when compared to high latitude FIR emission, possibly due to optical effects. The next section descibes a pixel-masking strategy designed to mitigate both r_s suppressing
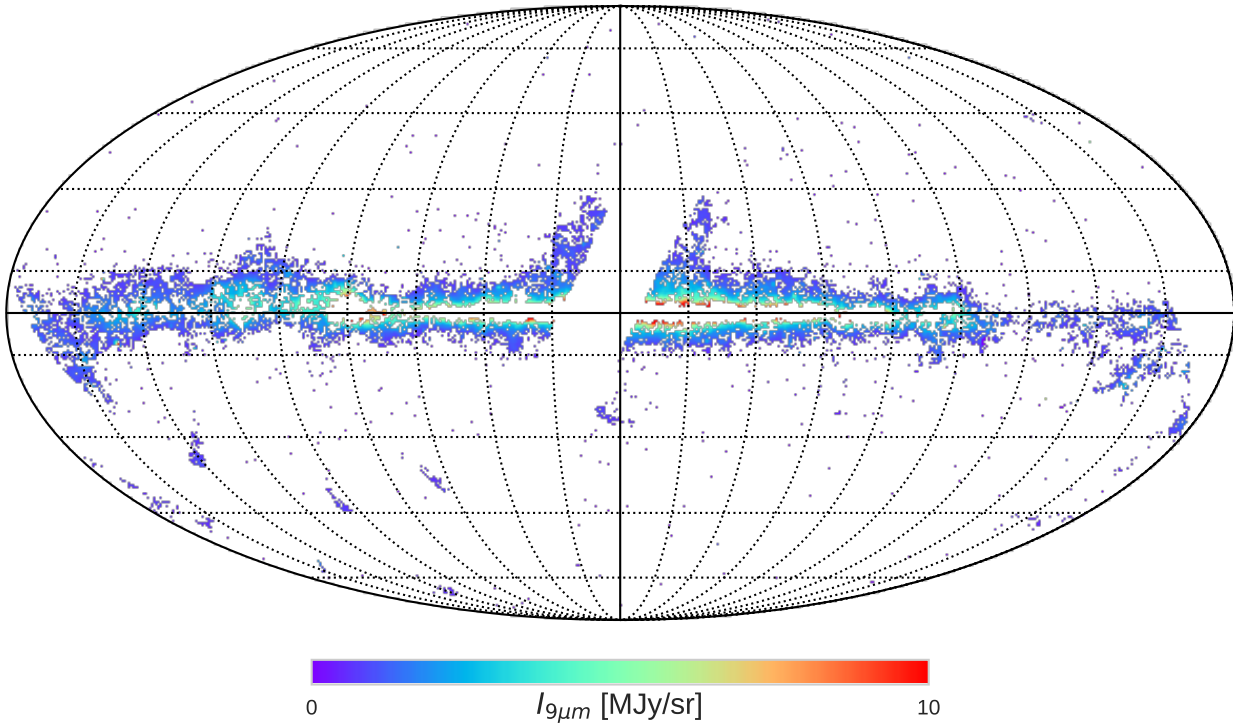
Figure 4.4: All-sky map in A9 emission after applying the combined masks: ecliptic plane, galactic plane, point sources, and pixels with S/N < 3. This mask essentially outlines the galaxy, except for the most confused regions. Diffuse galactic emission is essentially removed by the mask due to low S/N in the MIR bands. In the full sky map of ~700,000 pixels, there are ~50,000 unmasked pixels remaining.

effects from band-to-band S/N variations, and r_s enhancing effects from confusion near the galactic plane.

4.3   Masked Comparison

For the reasons described in the previous section, we consider that an exhaustive comparsion of the AME with IR requires the use of a pixel mask. In this section we describe the various masks applied to the full dataset. We then repeat both the comparisons above (as in Figs. 4.2 and 4.3) for the masked dataset, and present additional analyses. The full mask, superimposed on A9 map, is shown in Fig. 4.4, with the details of the mask layers desribed in the next subsection. The mask most heavily affects high galactic latitudes, and the galactic plane. The same mask is applied to all of the maps.

4.3.1 Pixel mask

Galactic plane   The galactic plane tends to be a challenge in any comparison, but especially with low resolutions studies such as the present work. Complicated structures along the line of sight, smoothed to 1° resolution, means that emisison within any given pixel is an average of many different environments (evidenced by the homogenizing of the correlations between bands at low latitudes in Fig. 4.3.) Thus we exclude the brightest emission of the galactic plane, according to the mask prepared by the Planck Collaboration.

Zodiacal light   To minimize the effects of residual zodiacal light, we exclude pixels within 10° of the ecliptic plane. Even though we use the Zodi-subtracted maps (Kelsall et al. 1998; Kondo et al. 2016; Ootsubo et al. 2016), the Zodi residuals are still problematic (especially in the MIR.) This corresponds to regions with the heaviest contamination from Zodiacal light, where Zodi residuals are apparent even with visual inspection for all of the MIR bands used in this study. In Ch. 2, Figs. 2.6, and 2.6 clearly display these residual patterns.

Signal to noise   Some of the bands used lack sufficient sensitivity to trace fainter emisison, especially at higher galactic latitudes. This is mainly an issue for the mid-infrared bands. As such, we enforce a 3σ threshold for all of the maps— adding to the mask any pixel that has lower than 3σ detection in any of the maps. This removes nearly all pixels beyond approximately 15° from the galactic plane, with the pronounced exception of regions affected by stray moonlight. The extent of this particular mask is primarily defined by the IRC A9 and A18 maps, which have the highest noise levels.

Point Sources   The Planck Collaboration provides masks of the pixels they find to include point sources. We mask pixels which are flagged as being point-source contaminated, in the most heavily affected maps: Planck/HFI 857 GHz and Planck/LFI 30 GHz.

PC Component Separation Errors   As noted in Planck Collaboration et al. (2016b); Hensley et al. (2016), there are fluctuations in the PC maps wherein AME emission appears to correspond to fluctuations in the synchrotron map. While a mask of all but the most reliably component separated pixels would be ideal, the construction of such a mask with the current data would require us to use a rather artificial threshold. While PC does provide error maps for
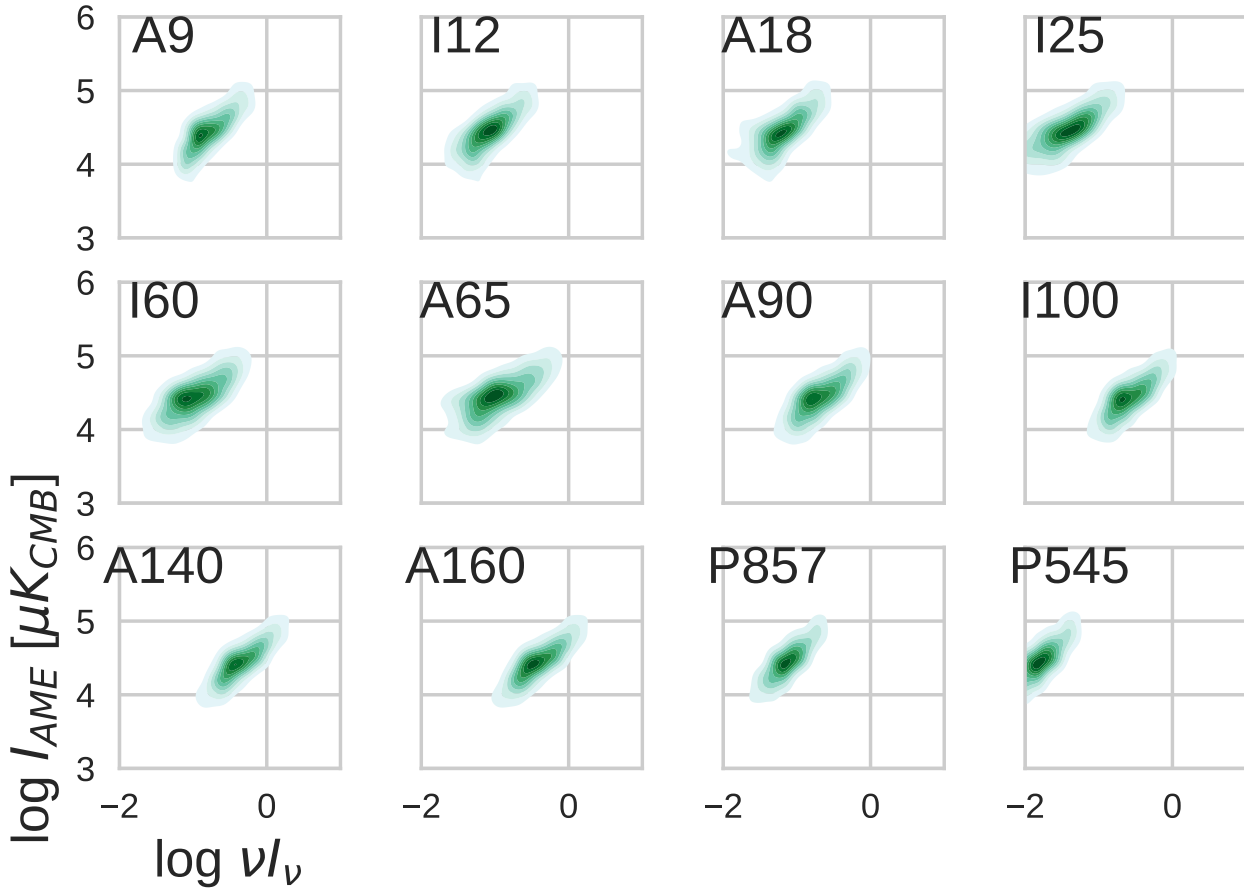
Figure 4.5: The same comparison as shown for Fig. 4.2, but with the mask applied as in Fig. 4.4.

each of the components, these are not necessarily an indication of how confident the component separation process itself is at a given pixel. We prefer not to apply any additional masks tailored to the PC maps, and instead present and discuss the results with the possibility of component separation artifacts in mind. However we do note that applying the LFI point source mask and galactic plane masks serves also to mask most pixels with AME peak frequency outliers.

4.3.2 Effect of mask application

Fig. 4.5 shows point-density plots for AME_{var} vs. each of the IR bands, after applying the mask described above. This reduces the number of pixels from ~780,000 to ~50,000, with about 7% of the sky remaining. As expected with such a drastic reduction of the number of noise-dominated points, the scatter, especially for the MIR bands, is reduced. This can be seen by comparing Fig. 4.5 to the unmasked distributions vs. AME in Fig. 4.2. Otherwise the applicaiton of the mask does not bring about any special distinction among the bands when compared to the AME. What is notable however is that the persistent weakening of trend of

I25 vs. AME, relative to A9 and the FIR bands. This is seen also when looking at the full set of interrelations via the cross-correlation matrix in Fig. 4.6.

Normalizing by radiation field U Following the logic that the PAH-tracing bands intensity is essentially a product U and the column density of PAHs σ_{PAH} (as explained in Ch. 2), we redraw the comparison after scaling the MIR bands by U. We determine U by taking the 1°-smoothed, degraded PR1 dust radiance map (also used in (Hensley et al. 2016)), and its corresponding τ_{353} map. We approximate $U \propto R/\tau_{353}$. In the case of U-normalized intensities correlation plots, we only include the MIR bands. While I_{MIR}/U is thought to trace column density of the band carriers (PAHs, or VSGs), there is a less definite interpretation of I_{FIR}/U (since the profile of FIR dust emission depends on the dust temperature.) Thus for this particular comparison, we represent the FIR with τ_{353}. The U-normalized correlation matrix is given by Fig 4.7. In this comparison, we see that all of the correlations of the MIR bands vs. AME weaken slightly when we scale the MIR bands by U. However if we consider that U may also affect the AME intensity, it may make sense to show a comparison where the MIR bands and AME intensities are all scaled by U. The result of this is shown on the right panel of Fig. 4.7. Indeed the correlations improve slightly, between MIR/U and AME/U. However we cannot rule out a spurious improvement of the correlations, induced by the common division by noise in the parameter U.

R-normalized comparison For completeness we perform a comparison similar to that provided in Hensley et al. (2016), wherein they compared the ratio I_{AME}/R (a sum of AME_{var} and AME_{fix}) to the fraction of dust in PAHs, $fPAH$. In our analysis, the ratios of $A9/R$ and $I12/R$, considering that A9 and I12 are dominated by PAH emission, would be comparable to the Hensley et al. (2016) parameter of $fPAH$. As with the result in Hensley et al. (2016), these data do not reveal any correlation between PAH fraction and I_{AME}/R, or with any of the MIR/R ratios and I_{AME}/R. Interestingly, there is evidence of a marginal positive trend with synchrotron, and a negative trend with free-free emission.

Bootstrap test In addition, for the masked comparison, we carry out a boostrap analysis, using the same method explained in Ch. 1 and implemented in Ch. 3. The Spearman rank correlation coefficents r_S of all of the bands, in intensity, vs. the AME_{var} component are

	A9	I12	A18	I25	I60	A65	A90	I100	A140	A160	P857	P545	AMEvar	AMEfix	ff	Sync	N_H	H_a	H408
A9	1	0.91	0.92	0.89	0.86	0.85	0.89	0.91	0.93	0.93	0.87	0.84	0.77	0.83	0.67	0.62	0.71	0.41	0.64
I12	0.91	1	0.81	0.95	0.81	0.86	0.85	0.86	0.89	0.9	0.86	0.83	0.76	0.8	0.62	0.69	0.63	0.26	0.71
A18	0.92	0.81	1	0.85	0.82	0.74	0.84	0.85	0.86	0.86	0.8	0.77	0.69	0.76	0.63	0.55	0.69	0.41	0.58
I25	0.89	0.95	0.85	1	0.83	0.81	0.85	0.88	0.9	0.91	0.88	0.85	0.75	0.79	0.61	0.67	0.66	0.25	0.69
I60	0.86	0.81	0.82	0.83	1	0.92	0.99	0.99	0.93	0.92	0.78	0.73	0.73	0.83	0.7	0.75	0.63	0.56	0.79
A65	0.85	0.86	0.74	0.81	0.92	1	0.94	0.92	0.9	0.89	0.77	0.73	0.72	0.81	0.69	0.75	0.58	0.47	0.78
A90	0.89	0.85	0.84	0.85	0.99	0.94	1	1	0.96	0.95	0.83	0.79	0.77	0.86	0.71	0.74	0.66	0.53	0.78
I100	0.91	0.86	0.85	0.88	0.99	0.92	1	1	0.97	0.96	0.85	0.81	0.78	0.87	0.71	0.74	0.68	0.51	0.78
A140	0.93	0.89	0.86	0.9	0.93	0.9	0.96	0.97	1	1	0.93	0.9	0.81	0.89	0.71	0.68	0.76	0.46	0.7
A160	0.93	0.9	0.86	0.91	0.92	0.89	0.95	0.96	1	1	0.94	0.91	0.81	0.88	0.71	0.68	0.76	0.43	0.7
P857	0.87	0.86	0.8	0.88	0.78	0.77	0.83	0.85	0.93	0.94	1	1	0.79	0.84	0.68	0.53	0.85	0.32	0.55
P545	0.84	0.83	0.77	0.85	0.73	0.73	0.79	0.81	0.9	0.91	1	1	0.76	0.82	0.67	0.49	0.87	0.31	0.5
AMEvar	0.77	0.76	0.69	0.75	0.73	0.72	0.77	0.78	0.81	0.81	0.79	0.76	1	0.9	0.45	0.61	0.65	0.3	0.62
AMEfix	0.83	0.8	0.76	0.79	0.83	0.81	0.86	0.87	0.89	0.88	0.84	0.82	0.9	1	0.6	0.59	0.73	0.48	0.62
ff	0.67	0.62	0.63	0.61	0.7	0.69	0.71	0.71	0.71	0.71	0.68	0.67	0.45	0.6	1	0.34	0.58	0.7	0.4
Sync	0.62	0.69	0.55	0.67	0.75	0.75	0.74	0.74	0.68	0.68	0.53	0.49	0.61	0.59	0.34	1	0.33	0.13	0.99
N_H	0.71	0.63	0.69	0.66	0.63	0.58	0.66	0.68	0.76	0.76	0.85	0.87	0.65	0.73	0.58	0.33	1	0.4	0.33
H_a	0.41	0.26	0.41	0.25	0.56	0.47	0.53	0.51	0.46	0.43	0.32	0.31	0.3	0.48	0.7	0.13	0.4	1	0.2
H408	0.64	0.71	0.58	0.69	0.79	0.78	0.78	0.78	0.7	0.7	0.55	0.5	0.62	0.62	0.4	0.99	0.33	0.2	1

Figure 4.6: Cross-correlation (r_s matrix for the IR intensities (unscaled) vs. each other, esssentially the same comparison as in Fig. 4.3, except that the pixel mask is applied, and we do not perform a split by Galactic latitude— after the mask is applied, over 90% of pixels are within 10° of the galactic plane.
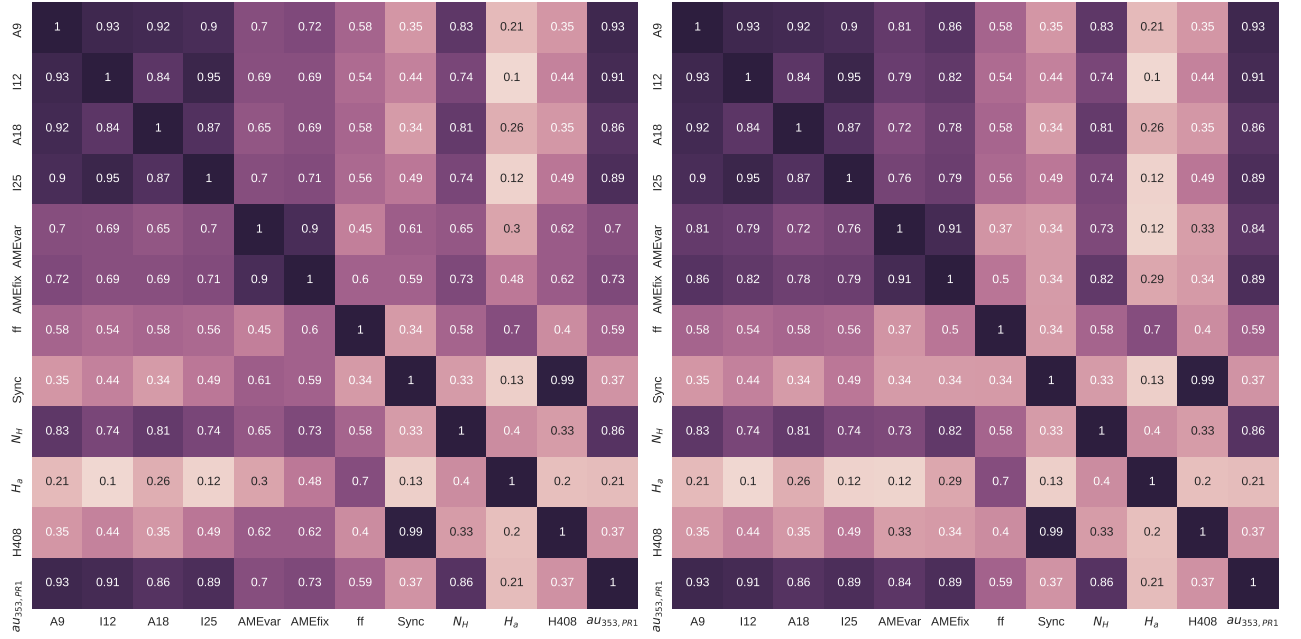
Figure 4.7: Cross-correlation (r_s matrix for the U-normalized IR intensities vs. each other, and also against the AME components, other PC products, and ancilliary data. In the left panel, only the IR maps are divided by U- other data is unchanged from. In the panel at right, both the the AME and IR intensities are divided by U. Fig. 4.6)
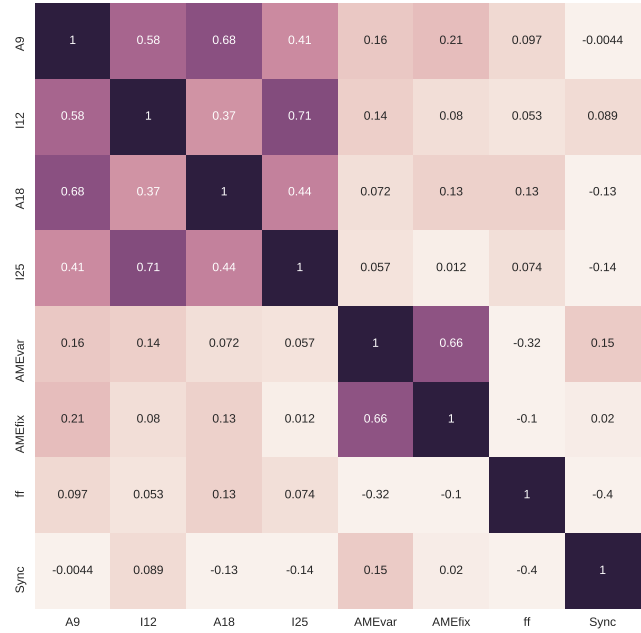
Figure 4.8: Cross-correlation (r_s matrix for the residual correlations between IR intensities, AME, and other microwave components. All of the maps in this case are normalized by R.)
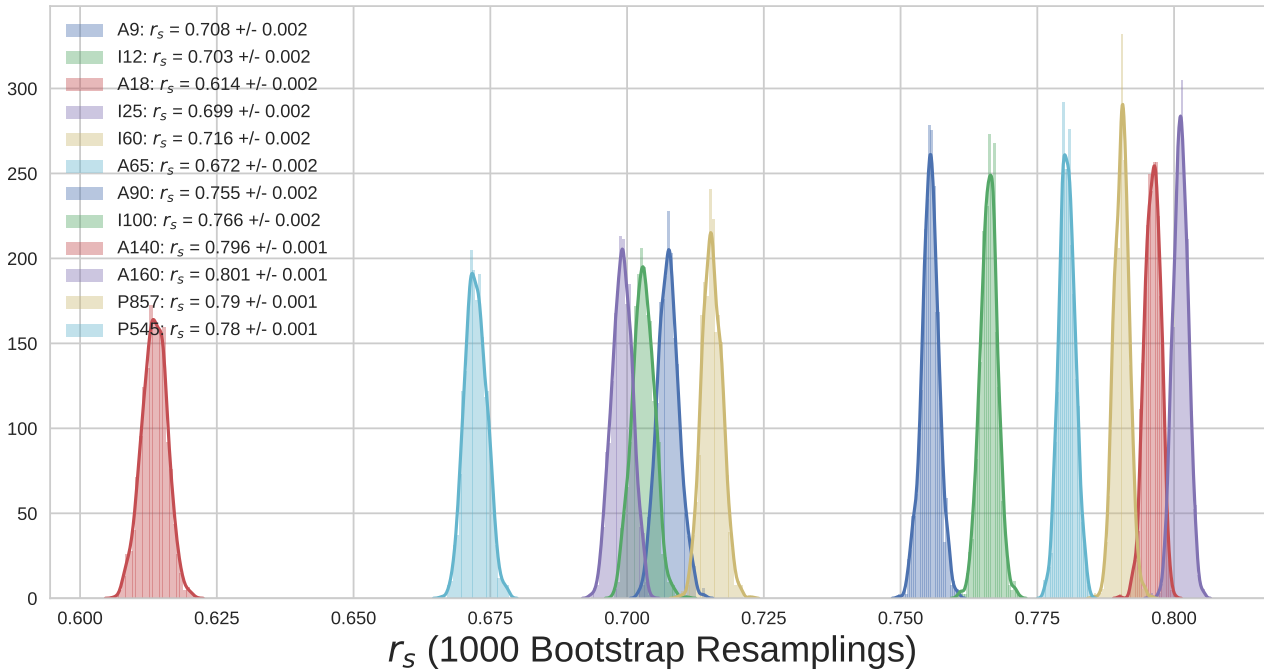
Figure 4.9: Re-sampled (Bootstrap) correlation tests for IR emission vs. AME, performed on the masked all-sky maps. Each band's r_s distribution is shown in a different color. The width of the distribution indicates the error for the given data in the correlation coefficient. The mean and standard deviation of the scores are given in the legend of each plot. The plot ranges only show positive values, since no negative scores were produced.

shown. This is done only for the masked case, due to the computational challeneges presented by a well-sampled bootstrap of all ~780,000 pixels in the full sky. Because the mask applied here leaves us with approximately 7% the sky, a bootstrap with $N_{iterations} > N_{pix}$ becomes tractable. We show the comparison only for the AME_{var} component also due to computational constraints. The r_s distributions for each IR band vs. AME are shown in Fig. 4.9. The calculations are performed in the same way as with Fig. 3.8 for λ Orionis. Consistent with the other correlation analyses already shown in this chapter, there is a stronger correlation in the FIR, especially A160. Considering the MIR range, and as with λ Orionis, A9 emission correlates better than I12. The worst correlation is seen with the A18 and I25 bands.

4.4 Spatial variation of correlations

To understand how these trends may vary across the sky, independent from the choice of pixel masl, we produce an all-sky maps of r_s for AME vs. IR emission. From the NSIDE 256 input maps of AME and 4 IR wavelength maps, we produce NSIDE 8 maps of r_s. These maps are shown in Figs. 4.10-4.13
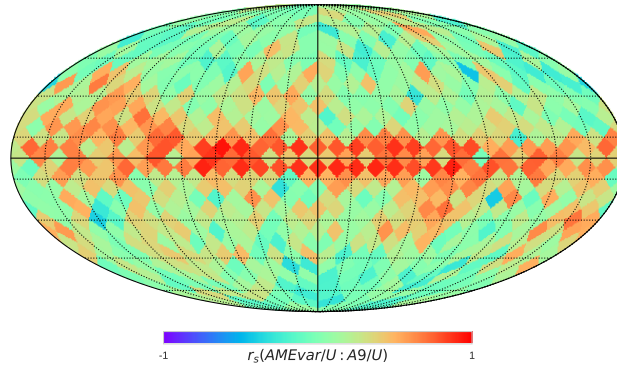
Figure 4.10: Spatial map of r_s between the AME:U and A9:U, a tracer of the column density of PAHs emitting within the A9 filter. r_s is calculated for all NSIDE 256 pixels within each NSIDE 8 pixel-sized bin. The correlation score is calculated with the unmasked maps. The colorbar indicates r_s, ranging from -1 (negative monotonic relationship) to +1 (positive monotonic relationship).
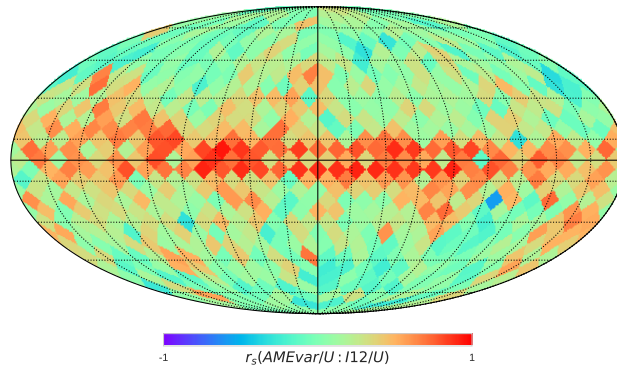
Figure 4.11: Spatial map of r_s between the AME:U and I12:U
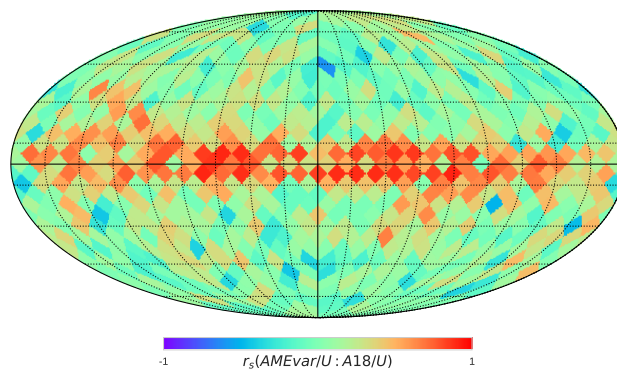
Figure 4.12: Spatial map of r_s between the AME:U and A18:U
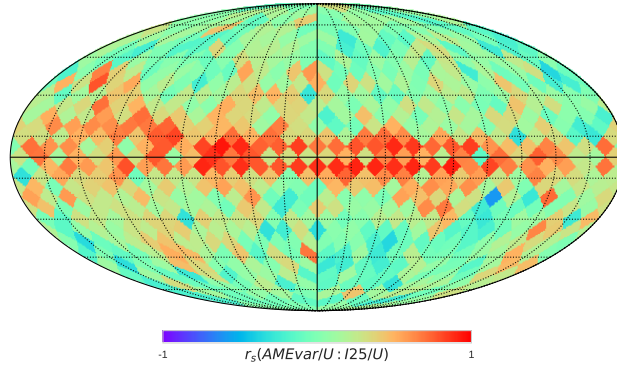
Figure 4.13: Spatial map of r_s between the AME:U and I25:U

The most important feature of these maps is that they look very similar, confirming in a spatial context that there is very little difference overall, when comparing AME to IR in intensity, accross multiple wavelengths. The correlations weaken for the MIR bands at higher latitudes, as expected. Thus the question of which band correlates better depends on exactly where we look.

4.5 Discussion

As noted in Ch. 1, previous studies found that the AME generally correlates at dust-related IR wavelengths (Ysard et al. 2010; Planck Collaboration et al. 2014d; Hensley et al. 2016). We see the same overall pattern in the present study. We also corroborate that the FIR emission shows the tightest correlation with the AME intensity, for large portion of the sky in a de-localized fashion (Figs. 4.3 and 4.6). In testing for a second-order correlation, we divided the IR intensities and AME intensity by U, and again performed the band-by-band all-sky comparison. There is evidence of a residual correlation between I_{MIR}/U and I_{AME}/U (Figs. 4.7, and 4.10-4.13).

The closeness of the correlation coefficients found here is consistent with the results of the IRAS vs. AME correlation test result from Planck Collaboration et al. (2014d). They found that the correlation coefficient among the four IRAS bands (12, 25, 60, and 100 μm) differ from one another only by about 5%, across their whole set of 98 regions. They had also indicated that many of the regions sampled were HII regions, and that free-free emission may not have been completely separated from the AME. We consider that a similar phenomenon may be happening in the PCAME map we explore here. The trend of AKARI MIR and FIR data

vs. the AME does not disagree with their IRAS comparison. This work adds that individual band intensities longer than IRAS 100 μm also correlate strongly with AME, especially the two Planck/HFI bands used.

4.5.1 AME and interstellar radiation fields

In our masked analysis, we were unable to replicate with the PC data a result by Ysard et al. (2010) wherein scaling the MIR bands by U improves the correlation of MIR vs. AME. Instead we found that the best correlation between the MIR bands and AME is found after scaling both by U. There is a chance that this improvement is induced by the common division of noise-terms in U, but if this correlation increase is real it may indicate that the AME intensity is somewhat dependent on U. While it is expected that AME intensity depends both on the abundance of carriers, and various excitation terms, it is not predicted that U directly influences spinning dust excitation. However it may be an indirect tracer of galactic environments and various other spinning dust excitation factors. he slight improvement with division by U was also seen with our investigation of λ Orionis in Ch. 3.

According to spinning dust theory outlined in Draine & Lazarian (1998a) and in subsequent works by Ysard & Verstraete (2010), the AME profile and intensity will depend in part on the ISRF- but as is well-stated in Hensley & Draine (2017), exactly how the ISRF will affect the AME SED is a more complicated question. Absorbed starlight photons may be able to rotationally excite the carriers, but if an enhanced ISRF leads to increased dust heating, then the increased IR emission can rotationally de-excite the carriers. Moreover the ISRF affects not only the dust temperature but ionization of the carriers.

4.5.2 Microwave foreground component separation

There are known degeneracies between the foreground parameters of the COMMANDER maps (spinning-dust, and free-free, synchrotron components as described in Planck Collaboration et al. (2016b).) This can be demonstrated by examining the ratio map of the AME intensity to R, in comparison with the PC free-free and synchrotron maps. Figs. 4.14 and 4.15 show the AME_{var}/R and AME_{fix}/R ratio maps, with contours from the free-free and synchrotron maps. There are clearly regions where synchrotron emission correlates with AME excesses. Some of these appear as more large scale fluctuations, mainly at higher galactic latitude. Interestingly,
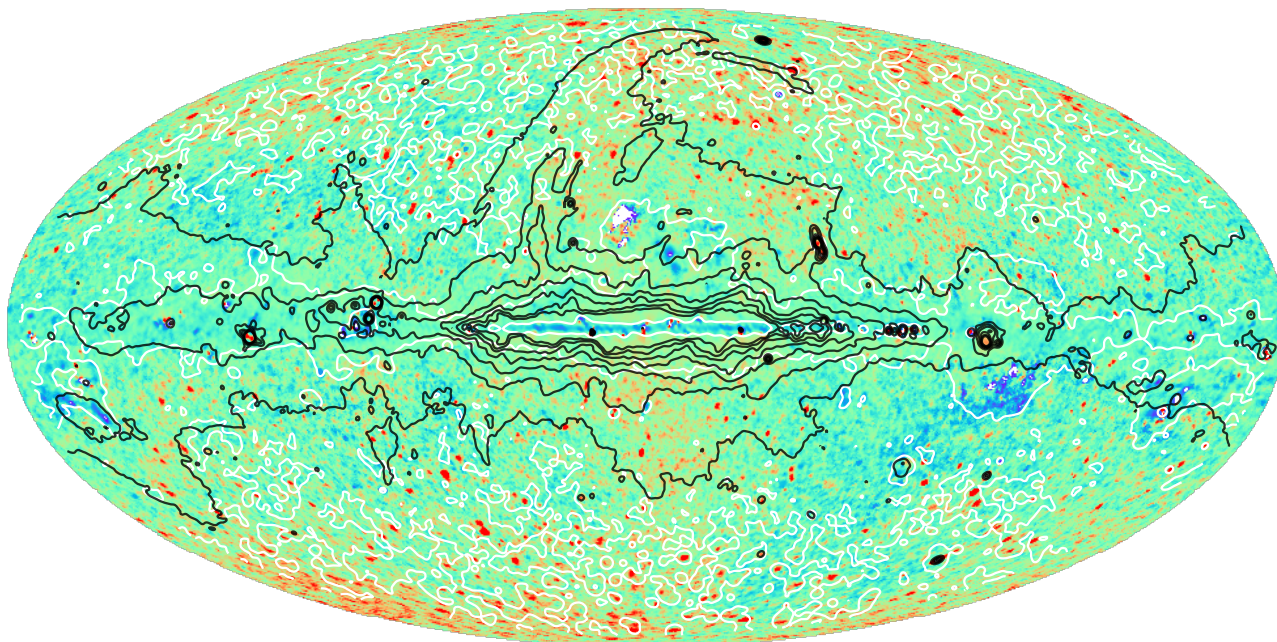
Figure 4.14: The ratio of AME_{var} and PC dust radiance R, tracing fluctuations in AME per thermal dust emission. The contours trace the PC synchrotron (black) and free-free (white) components, to highlight various correlations between these components and PC AME fluctuations. Both free-free and syhncrotron can be seen to correlate and anti-correlate with the AME to dust ratio.
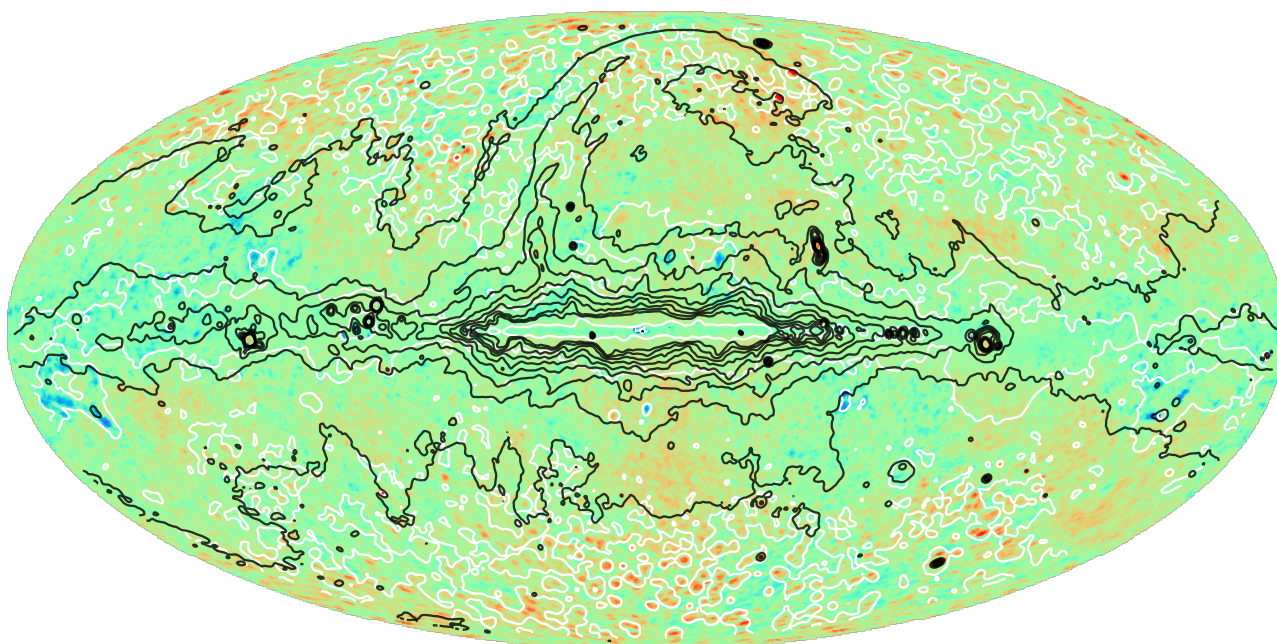

Figure 4.15: The same as Fig. 4.14, but with AME_{fix}/R as the all-sky image.

free-free shows agreement with both positive and negative fluctuations in both ratio maps. At high galactic latitude, free-free tends to be associated with positive fluctuations. This is supported by the fact that AME_{fix} shows an improved correlation with both the $H\alpha$ map and the PC free-free map, perhaps suggesting confusion between spinning dust and free-free components. Interestingly, the ring-structure of the λ Orionis region analyzed in Ch. 3, does not have any apparent conterpart in the AME/R ratio maps in Figs. 4.15 and 4.14.

The results of the R normalized cross-correlation test show that free-free/R shows a negative correlation with AME/R. This may be furher indication that the AME map, even with the mask applied from Sec.4.3.1, may suffer from significant MW component confusion in some regions. It is difficult to quantify potential effects from component separation uncertainties relative to genuine correlations between microwave emission components, with the present data. However there remains the potential for such confusion to suppress evidence of any trend between AME and the actual value of $fPAH$. The anti-correlation here between free-free/R and AME/R may be consistent with findings in von Hausegger & Liu (2015) that free-free emission anti-correlates with AME, if pixels are weighted by S/N.

Even though A9/R and I12/R do not correlate with AME/R in our masked comparison, we do find some limited regions where these values correlate in our full spatial correlation mapping.

4.5.3   Optical depth

In the interpretation of results here, we have essentially operated under the assumption that MIR/PAH emisison, FIR emission, and the AME are all in the optically thin domain. This is supported by the strong agreement in r_s, accross all IR bands and the AME, as presented in the correlation matrices here. (With the exception of the high-latitude, unmasked case in Fig 4.3.) Conversely, the $H\alpha$ data — emission known to be absorbed by interstellar dust — is the only map lacking a correlation with the others at $|\beta| < 5°$. $N(H)$ also shows a weaker correlation nearer to the galactic plane, likely influenced by saturation and/or self-absorption effects.

However it has been demonstrated by Sakon et al. (2004) that the optically-thin assumption for PAH/UIR emission could lead to errors in the estimate of PAH abundance based on these emision features. Self-absorption for PAHs is another possibility.

We do not expect the analysis presented here to suffer from such effects significantly, as we

have masked the most confused lines of sight towards the galactic plane. However we cannot rule out the possibility that such optical depth effects, not only in PAH emisison but in the FIR or even AME, may weaken any potential relationship between the IR and microwave emisison from spinning grains.

4.5.4 Comparison of λ Orionis vs. All-sky results

Results presented here do not necessarily conflict with results from Ch. 3, except in that the findings from Fig. 3.8, wherein r_p of A9 emission correlates better with AME than P545 emission, do not generalize to the results of this chapter (either the masked or unmasked cases.) However, in the masked all-sky comparison as well as in λ Orionis, we find a better corrleation between A9 and AME than between I12 and AME when we subject the correlations to bootstrap resampling.

The different results between Ch. 3 and Ch. 4 may be explained by variations in the component separation reliability. It is apparent that with the presently available data, there are a very limited number of regions on the sky which do not show strong free-free or synchrotron emission (relative to AME), while also having enough S/N in the MIR to reliably probe a relationship between PAH abundance fluctuations and AME fluctuations. λ Orionis may be one of the exceptions, where the S/N is high enough, and we are in fact able to see an improved correlation between PAHs and AME, relative to the overall dust emission to AME connection.

We also disucssed in Ch. 4 the possibility that the PAH emission may not necessarily be optically thin. If this were true, it may explain discrepancies for our λ Orionis result and the results in this chapter. λ Orionis provides us a relatively clean line of sight compared to delocalized all-sky analysis.

The fact that we do not see a clear preferential relationship between AME and PAHs in the all-sky analysis, does not rule out a contribution by spinning PAHs to the AME. Likewise the fact that we do see a better correlation in λ Orionis does not rule out contributions from other proposals, such as that form non-PAH small grains, or nanosilicates.

4.5.5 Implications of an absent PAH-AME correlation

In the case that we are able to rule PAHs out as the AME carrier with confidence, this may imply some constraints on the PAH size distribution and dipole moment. As discussed in the

theoretical work by Draine & Lazarian (1998a); Ali-Haimoud (2010) and others, as well as the observational work by Hensley et al. (2016), if PAHs exist in the ISM, they are very likely to be spinning rapidly. Thus if we are able to confirm that they do not produce AME, this could tell us the morphology of ISM PAHs are not in an appropriate range to produce the observed AME. Spinning PAHs may be a reality even in the case that the AME comes from something else, if the PAHs are too large or lack appropriate electric dipoles.

4.6 Future Works

Because of the issues highlighted in previous sections (S/N, component separation, etc.), it is extremely difficult to draw a conclusion about the carrier of AME based on a general all-sky analysis such as that shown here. However there may be promise in studies of individual regions, where an attempt can be made at controlling for local environmental factors, or background/-foreground contamination. While it is true that previous studies of specific objects have also not been conclusive, such as the investigation of Perseus by Tibbs et al. (2011), there are still many other AME prominent regions which have not been probed in-depth, through a combination of microwave and PAH-range observations. Even the study of λ Orionis in Ch. 3 is not exhaustive, and this interesting region deserves further attention from targeted observations.

New tests of AME hypotheses should: push limitations in the available data and, focus on regions well-documented to show a spinning-dust-like AME spectrum. While a simple excess of microwave emission may be able to be fit by a spinning dust model SED, the spinning dust explanation is not testable unless the observed SED shows evidence of a low-frequency downturn.

There are two major boundaries that, based on results presented here, must be pushed. Spatial resolution and spectral coverage. Spatial resolution constraints are a critical issue in multiwavelength astornomy, especially in dust-related works. To explain why, simply consider the description of dust research from Ch. 1, and Tab. 2.1. The spatial resolution of available data has a wide discrepancy from the MIR to microwave: 10 arcseconds for AKARI 9 micron to at least a degree FWHM for the "effective resolution" of parameter maps. Likewise, if there are enivonmental diffrences only visible at sub-degree angular scales, we will have a hard time controlling for the excitation factors of spinning dust emission. Without separating excitation

factors from column density of the carriers. Pairing opportunities for resolution maximizing ground-based observations of very limited regions of the sky, utilizing facilities such as the Atacama Large Milimeter Array (ALMA) Band 1 (30-35 GHz, still in production, Huang et al. (2016).), with detailed assesment of tracers of small dust grains, will be helpful.

Future breakthroughs in the AME may be seen if we are able to increase the number of regions with a reliable AME estimation. This can be obtained through improved synchrotron emission constraints, at higher resolutions. C-Band All Sky Survey (CBASS) at 5 GHz will be helpful in this regard (Irfan et al. 2015). CBASS is expected to provide higher resolution low frequency constraints for the whole sky (48′ compared to 56′ for $H408$), with improved sensitivity (0.1 μK). In terms of localized studies, it may be fruitful to consider the physical environment of each region (i.e. ionization state, gas temperature and density, other conditions indicated in Draine & Lazarian (1998a); Ali-Haimoud (2010) to affect the SED shape) rather than relying of frequency-shifts to a template spectrum. More detailed exploration of PAH ionization, and other fluctuations between individual PAH features relative to variations in the AME spectral profile may also help us understand potential roles of PAHs in producing AME. However, even if we have excellent constraints on PAH emission features, synchrotron emission, free-free emission, and a powerful spinning dust SED model, the key data will be spectral coverage of the full AME profile. As noted in Ch. 2, the all-sky maps currently available, do not give constraints in the 10-20 GHz range. This means that lower frequency spinning dust peaks and emissivities are not well known. Improved understanding of AME and spinning dust therefore will require observations such as those being undertaken by the Q-U-I JOint Tenerife Experiment (QUIJOTE) project, which offers coverage between 10 and 20 GHz (Génova-Santos et al. 2015).

Chapter 5

Summary

In Ch. 1 we demonstrated both the mysteries and potential for answers revealed by all-sky observation and analysis. A paticular mystery, that of the Anomalous Microwave Emission (AME), and the popular but yet unproven hypothesis that this AME comes from rapidly spinning tiny dust grains, perhaps PAHs, was introduced. We explained the merit of testing a spinning PAH hypothesis, while noting that spinning nanosilicates, or even magnetic dipole emission from dust have also been put forth in the literature.

In Ch. 2, we overviewed a collection of infrared all-sky surveys that help us prove the dust SED from the UIR band range to the FIR, and discussed how these could help explore the AME question. We described also complimentary data and parameter maps from the Planck Collaboration that can be compared with the IR maps. Particular advantages of the PAH tracing bands, especially the A9 band, for covering not only neutral but potentially charged PAHs, were discussed in the context of AME investigation. Limitations were given for all of these data sets— most of these boiling-down to component separation either of the Zodiacal light from thermal dust emission, or to the latter from other microwave foregrounds and the CMB.

In Ch. 3 we combined and processed the data presented in Ch 2 to investigate a particular region of the sky with relatively high S/N in all of the data, and demonstrating strong AME. We evaluated the background, noise, and contamination from systematic errors and point sources in these data, and compared them on a common resolution and grid. All of the analyses from simple correlation plots, to bootstrap analysis, to dust SED fitting suggest that A9 emisison correlates with AME better than I12 or D12 — supporting PAH emisison as the source of AME, and suggesting the role of charged PAHs should be further explored. In addition we

find that the bands near the thermal dust emisison peak show a weaker correlation, perhaps suggesting that harsh radiation fields may be destroying PAHs, leading to weaker AME. We also cautioned that although PAH mass correlates better than dust mass, we still see a good correlation between FIR emisison and AME (P545, P857). This highlights the fact that AME, PAHs, and cold dust are all correlated.

In Ch. 4 we attempted to find evidence that the result from Ch. 2 applies even when looking at a less region-specific scale, using an all-sky analysis. However neither the full-sky unmasked case, or the case employing a mask of low S/N regions (mainly high galactic latitudes), point sources, and the galactic plane, showed a stronger correlation between PAH related emission and AME than that seen between FIR emission and the AME. We did however find that as in Ch. 3, A9 tends to correlate with AME better than I12 or D12. We discussed apparent systemtic issues with the AME data, such as the possibility for under or over subtraction of free-free or synchrotron emission, and how these could serve to weaken evidence of any PAH or small grain correlation wiht the AME. Scaling the infrared intensities by U does not change this result. We reproduce the result from Hensley et al. (2016) that there is not an overall correlation between PAH fraction and AME-per-dust-emisison, but expand this calculation showing that for a few limited regions on the sky there may be evidence of a correlation. We discuss how a potential variation on the optical thickness between UIR bands, FIR emisison, among other factors, could lead to a different result between λ Orionis and the all-sky analysis. We also discuss potential observional advances that could help explore the issue further, such as improved low frequency constraints,or detailed analysis of the spatial variation of PAH features paired with high resolution AME observation.

Overall, using the presently available data, it is difficult to isolate the PAH-dust relationship, from the dust-AME relationship. We find throughout this work that a PAH-emission to AME correlation is readily demonstable, in intensity. A test of whether a second-order relationship exists, such that PAH emission is a better predictor of the AME than thermal dust emission, was shown to be inconclusive. One exception is that of λ Orionis, where our results suggest that PAH mass correlates better with AME than does the total dust mass. Nevertheless we emphasize this point cautiously. We were not able to generalize it to a larger scale (all-sky data with, effectively, a mask on the galactic plane and high latitude emission.) We are not able to confirm or reject a "spinning PAH" hypothesis for the source of AME. However in λ Orionis,

and perhaps other regions yet to be examined in with dust SED fitting, we suggest that there is still ample reason to continue testing this hypothesis.

Acknowledgements

I would like to thank Professor Takashi Onaka firstly for guiding me since I first came to his laboratory as an undergraduate summer intern, in June 2012. I'm not sure if I've worked hard enough for the honor of being his last Ph.D. student, but its been a pleasure. I am extremely happy that I to complete my degree here. I wish him the happies of retirements, while sincerely doubting he will be able to stay away from research for long.

Onaka-sensei and the members of the Onaka-lab have literally helped me to survive here, assisting any time that I have had difficulty adjusting as a foreign student.

Itsuki Sakon has helped me greatly from the moment I arrived in Japan (literally.) It is also quite refreshing when his driving skills leave me at my destination much earlier than planned.

I have been very lucky to have helpful co-authors for the various posters and abstracts I have presented in the course of this thesis: Ho-Gyu Lee, Daisuke Ishihara, Yasuo Doi, Ho-Gyu Lee, Mark Hammonds, Fumihiko Usui, Takafumi Ootsubo, Ryou Ohsawa, Tamami Okada, Hidehiro Kaneda — especially, my international collaborators kind enough to host me over the years, Ronin Wu, Mridusmita Buragohain, Rupjyoti Gogoi, Frederic Galliano, Amit Pathak, Martin Giard, and Olivier Berne.

My undergraduate advisor, Steven Gibson, deserves a special thanks for continued kind encouragement and research advice even now that I have graduated from WKU.

Most personally, I must thank my mother, Catherine Marie Bell who has supported me more than seems possible for a single human being. The same goes to my younger siblings, Joseph, Emma, Caleb, and Noah who I have too few opportunities to help grow up. I thank also Deborah and Faithie ("Mama") Guffy, who have been like aunt and gradnmother to us all.

My day to day life in Japan has been brightened by partner of five years, Yuki Sugisawa (杉澤友紀). His family too, who have been an unofficial host-family over the years, Chikako (千賀子様),Hiromi (宏美様), Takeshi (剛様), and Chiri. Even his grandmother Junko and grandfather Sadao Masuda (桝田順子と定雄様) have shown me much kindness during my visits to Osaka.

A special note of thanks is owed to my friends who have inspired me and shared moral support, from back in the US, throughout my program: Alexandria Boswell, Hannah Kagan-Moore, Alexander Chen, George Johnson, Nicolas Tarantino, and John Max Wilson; as well as my classmates at U.Tokyo, Scarlet Elgueta, Jerome de Leon, Ryouta Kawamata, Takahiro Sudoh, Taku Okamura, John Livingston, Kyle Mede, Yuta Kato, and others.

This project could not have found its way to any assemblance of completion without kind and insightful discussions with Nathalie Ysard, Alessandra Candian, Chikako Yasui, Norita Kawanaka, Bruce Draine, Chris Tibbs, Francois Boulanger, Brandon Hensley, Clive Dickinson, Yasushi Suto, Othman Benomar, and Anthony Jones.

The staff of GRID, Inc., especially Mehdi Shibahara and Ying-Ming Chen, helped guide my career choices and advance my knowledge of machine learning besides being the best lunch pals.

I wish the best of luck to my kohais in Onaka-lab: Izumi Endo, Jin Zhang, Tomoyuki Kimura, Ayato Ikeuchi, and Mingie Jian in their continued studies and careers. I also want to express special thanks to the staff of the International Liaison Office, for advising me over the last five years, even since I was an undergraduate research internship student, in the UTRIP program of 2012.

References

Aitken, D. K. 1981, in IAU Symposium, Vol. 96, Infrared Astronomy, ed. C. G. Wynn-Williams & D. P. Cruikshank, 207–221

Ali-Haimoud, Y. 2010, SpDust/SpDust.2: Code to Calculate Spinning Dust Spectra, Astrophysics Source Code Library

Ali-Haïmoud, Y. 2014, MNRAS, 437, 2728

Ali-Haïmoud, Y., Hirata, C. M., & Dickinson, C. 2009, MNRAS, 395, 1055

Allain, T., Leach, S., & Sedlmayr, E. 1996a, A&A, 305, 602

—. 1996b, A&A, 305, 616

Allamandola, L. J., Tielens, A. G. G. M., & Barker, J. R. 1985, ApJ, 290, L25

AMI Consortium et al. 2012, MNRAS, 423, 1463

Andrews, H., Boersma, C., Werner, M. W., Livingston, J., Allamandola, L. J., & Tielens, A. G. G. M. 2015, ApJ, 807, 99

Andrews, H., Candian, A., & Tielens, A. G. G. M. 2016, A&A, 595, A23

Aran, A. B. 2009, PhD thesis, UNIVERSIDAD AUTONOMA DE MADRID

Atwood, W. B., et al. 2009, ApJ, 697, 1071

Bayes, M., & Price, M. 1763, Philosophical Transactions of the Royal Society of London Series I, 53, 370

Bennett, C. L., et al. 2003a, ApJS, 148, 97

—. 2003b, ApJS, 148, 1

BICEP2 Collaboration et al. 2014, Physical Review Letters, 112, 241101

Bocchio, M., Micelotta, E. R., Gautier, A.-L., & Jones, A. P. 2012, A&A, 545, A124

Boggess, N. W., et al. 1992, ApJ, 397, 420

Bonnarel, F., et al. 2000, A&AS, 143, 33

Bot, C., Ysard, N., Paradis, D., Bernard, J. P., Lagache, G., Israel, F. P., & Wall, W. F. 2010, A&A, 523, A20

Burke, J. R., & Hollenbach, D. J. 1983, ApJ, 265, 223

Carrasco, L., Strom, S. E., & Strom, K. M. 1973, ApJ, 182, 95

Compiègne, M., et al. 2011, A&A, 525, A103

Cunha, K., & Smith, V. V. 1996, A&A, 309, 892

Davis, Jr., L., & Greenstein, J. L. 1951, ApJ, 114, 206

de Oliveira-Costa, A., Kogut, A., Devlin, M. J., Netterfield, C. B., Page, L. A., & Wollack, E. J. 1997, ApJ, 482, L17

de Oliveira-Costa, A., et al. 2002, ApJ, 567, 363

Dickinson, C., Paladini, R., & Verstraete, L. 2013, Advances in Astronomy, 2013, 1

Dickinson, C., et al. 2018, ArXiv e-prints

Doi, Y., et al. 2015, PASJ, 67, 50

Draine, B. T. 2011, Physics of the Interstellar and Intergalactic Medium

Draine, B. T., & Hensley, B. 2013, ApJ, 765, 159

Draine, B. T., & Lazarian, A. 1998a, ApJ, 494, L19

—. 1998b, ApJ, 508, 157

—. 1999, ApJ, 512, 740

Draine, B. T., & Li, A. 2001, ApJ, 551, 807

—. 2007a, ApJ, 657, 810

—. 2007b, ApJ, 657, 810

Duerr, R., Imhoff, C. L., & Lada, C. J. 1982, ApJ, 261, 135

Dwek, E., et al. 1997, ApJ, 475, 565

Efron, B. 1979, Ann. Statist., 7, 1

Emerson, J. P., Jennings, R. E., & Moorwood, A. F. M. 1973, ApJ, 184, 401

Erickson, W. C. 1957, ApJ, 126, 480

Feigelson, E. D., & Babu, G. J. 2013, Statistical Methods for Astronomy, ed. T. D. Oswalt & H. E. Bond, 445

Ferrara, A., & Dettmar, R.-J. 1994, ApJ, 427, 155

Finkbeiner, D. P. 2003, ApJS, 146, 407

Finkbeiner, D. P., Schlegel, D. J., Frank, C., & Heiles, C. 2002, ApJ, 566, 898

Flauger, R., Hill, J. C., & Spergel, D. N. 2014, J. Cosmology Astropart. Phys., 8, 039

Galliano, F. 2018, MNRAS

Galliano, F., Dwek, E., & Chanial, P. 2008, ApJ, 672, 214

Galliano, F., et al. 2011, A&A, 536, A88

Génova-Santos, R., et al. 2015, MNRAS, 452, 4169

Ghesquière, P., Talbi, D., & Karton, A. 2014, Chemical Physics Letters, 595, 13

Giard, M., Lamarre, J. M., Pajot, F., & Serra, G. 1994, A&A, 286

Gillett, F. C., Forrest, W. J., & Merrill, K. M. 1973, ApJ, 183, 87

REFERENCES

Gillett, F. C., Forrest, W. J., Merrill, K. M., Soifer, B. T., & Capps, R. W. 1975, ApJ, 200, 609

Górski, K. M., Hivon, E., Banday, A. J., Wandelt, B. D., Hansen, F. K., Reinecke, M., & Bartelmann, M. 2005, ApJ, 622, 759

Haas, M., Klaas, U., & Bianchi, S. 2002, A&A, 385, L23

Habing, H. J. 1968, Bull. Astron. Inst. Netherlands, 19, 421

Hagen, W., Allamandola, L. J., & Greenberg, J. M. 1979, Ap&SS, 65, 215

Hammonds, M., Pathak, A., & Sarre, P. J. 2009, Physical Chemistry Chemical Physics (Incorporating Faraday Transactions), 11, 4458

Hanson, D., et al. 2013, Physical Review Letters, 111, 141301

Haslam, C. G. T., Salter, C. J., Stoffel, H., & Wilson, W. E. 1982, A&AS, 47, 1

Hensley, B. S., & Draine, B. T. 2017, ApJ, 836, 179

Hensley, B. S., Draine, B. T., & Meisner, A. M. 2016, The Astrophysical Journal, 827, 45

Hirata, S., Lee, T. J., & Head-Gordon, M. 1999, J. Chem. Phys., 111, 8904

Hoang, T., Vinh, N.-A., & Quynh Lan, N. 2016, ApJ, 824, 18

Hohenberg, P., & Kohn, W. 1964, Physical Review, 136, 864

Hony, S., Van Kerckhoven, C., Peeters, E., Tielens, A. G. G. M., Hudgins, D. M., & Allamandola, L. J. 2001, A&A, 370, 1030

Hoyle, F., & Wickramasinghe, N. C. 1970, Nature, 227, 473

Huang, Y. D. ., et al. 2016, in Proc. SPIE, Vol. 9911, Modeling, Systems Engineering, and Project Management for Astronomy VI, 99111V

Iglesias, E. 1977, ApJ, 218, 697

Irfan, M. O., et al. 2015, Monthly Notices of the Royal Astronomical Society, 448, 3572

Ishihara, D., et al. 2007, PASJ, 59, S443

—. 2010, A&A, 514, A1

Israel, F. P., Wall, W. F., Raban, D., Reach, W. T., Bot, C., Oonk, J. B. R., Ysard, N., & Bernard, J. P. 2010, A&A, 519, A67

Joblin, C., Berné, O., Simon, A., & Mulas, G. 2009, in Astronomical Society of the Pacific Conference Series, Vol. 414, Cosmic Dust - Near and Far, ed. T. Henning, E. Grün, & J. Steinacker, 383

Johnson, H. L. 1966, ARA&A, 4, 193

Jones, A. 2014, ArXiv e-prints

Jones, A. P. 2009, A&A, 506, 797

Jones, A. P., Fanciullo, L., Köhler, M., Verstraete, L., Guillet, V., Bocchio, M., & Ysard, N. 2013, A&A, 558, A62

Jones, A. P., Köhler, M., Ysard, N., Bocchio, M., & Verstraete, L. 2017, A&A, 602, A46

Juvela, M., & Ysard, N. 2012, A&A, 539, A71

Kalberla, P. M. W., Burton, W. B., Hartmann, Dap, Arnal, E. M., Bajaja, E., Morras, R., & Pöppel, W. G. L. 2005, A&A, 440, 775

Kawada, M., et al. 2007a, PASJ, 59, S389

—. 2007b, PASJ, 59, 389

Kelsall, T., et al. 1998, ApJ, 508, 44

Kessler, M. F., et al. 1996, A&A, 315, L27

Knacke, R. F., Gaustad, J. E., Gillett, F. C., & Stein, W. A. 1969, ApJ, 155, L189

Knapp, G. R., & Kerr, F. J. 1974, A&A, 35, 361

Koenig, X., Hillenbrand, L. A., Padgett, D. L., & DeFelippis, D. 2015, AJ, 150, 100

Kogut, A., Banday, A. J., Bennett, C. L., Gorski, K. M., Hinshaw, G., & Reach, W. T. 1996, ApJ, 460, 1

Kondo, T., et al. 2016, AJ, 151, 71

Lau, R. M., Herter, T. L., Morris, M. R., Li, Z., & Adams, J. D. 2015, Science, 348, 413

Leach, S. M., et al. 2008, A&A, 491, 597

Leitch, E. M., Readhead, A. C. S., Pearson, T. J., & Myers, S. T. 1997, ApJ, 486, L23

Li, A., Chen, J. H., Li, M. P., Shi, Q. J., & Wang, Y. J. 2008, MNRAS, 390, L39

Li, A., & Draine, B. T. 2001, ApJ, 554, 778

Lovas, F. J., McMahon, R. J., Grabow, J.-U., Schnell, M., Mack, J., Scott, L. T., & Kuczkowski, R. L. 2005, Journal of the American Chemical Society, 127, 4345, pMID: 15783216

Maddalena, R. J. 1986, PhD thesis, National Aeronautics and Space Administration. Goddard Inst. for Space Studies, New York, NY.

Maddalena, R. J., & Morris, M. 1987, ApJ, 323, 179

Martin, D. C., et al. 2005, ApJ, 619, L1

Mathis, J. S., Mezger, P. G., & Panagia, N. 1983, A&A, 128, 212

Mathis, J. S., Rumpl, W., & Nordsieck, K. H. 1977, ApJ, 217, 425

Mattila, K., Lemke, D., Haikala, L. K., Laureijs, R. J., Leger, A., Lehtinen, K., Leinert, C., & Mezger, P. G. 1996, A&A, 315, L353

Merrill, K. M., Soifer, B. T., & Russell, R. W. 1975, ApJ, 200, L37

Miville-Deschênes, M.-A., & Lagache, G. 2005, ApJS, 157, 302

Muehlner, D., & Weiss, R. 1970, Physical Review Letters, 24, 742

Murakami, H., et al. 1996, PASJ, 48, L41

—. 2007, PASJ, 59, 369

Murdin, P., & Penston, M. V. 1977, MNRAS, 181, 657

Neugebauer, G., et al. 1984, ApJ, 278, L1

Ochsendorf, B. B., Brown, A. G. A., Bally, J., & Tielens, A. G. G. M. 2015, ApJ, 808, 111

Olofsson, J., Juhász, A., Henning, T., Mutschke, H., Tamanai, A., Moór, A., & Ábrahám, P. 2012, A&A, 542, A90

Onaka, T. 2000, Advances in Space Research, 25, 2167

Onaka, T., Yamamura, I., Tanabe, T., Roellig, T. L., & Yuen, L. 1996, PASJ, 48, L59

Onaka, T., et al. 2007, PASJ, 59, 401

Ootsubo, T., et al. 2016, PASJ, 68, 35

Paladini, R., Ingallinera, A., Agliozzo, C., Tibbs, C. T., Noriega-Crespo, A., Umana, G., Dickinson, C., & Trigilio, C. 2015, ApJ, 813, 24

Pathak, A., & Rastogi, S. 2005, in IAU Symposium, Vol. 235, IAU Symposium, 72P

Pavlyuchenkov, Y. N., Kirsanova, M. S., & Wiebe, D. S. 2013, Astronomy Reports, 57, 573

Perrott, Y. C., et al. 2018, MNRAS, 473, 1157

Pettit, E., & Nicholson, S. B. 1922, ApJ, 56, 295

—. 1928, ApJ, 68

Pilbratt, G. L., et al. 2010, A&A, 518, L1

Pilleri, P., Montillaud, J., Berné, O., & Joblin, C. 2012, A&A, 542, A69

Planck Collaboration et al. 2011a, A&A, 536, A1

—. 2011b, A&A, 536, A20

—. 2014a, A&A, 571, A1

—. 2014b, A&A, 571, A8

—. 2014c, A&A, 571, A12

—. 2014d, A&A, 565, A103

—. 2016a, A&A, 594, A1

—. 2016b, A&A, 594, A10

—. 2016c, A&A, 594, A25

—. 2016d, A&A, 586, A132

—. 2017, A&A, 599, A51

Platt, J. R. 1956, ApJ, 123, 486

Puget, J. L., Leger, A., & Boulanger, F. 1985, A&A, 142, L19

Rastogi, S., Pathak, A., & Maurya, A. 2013, in American Institute of Physics Conference Series, Vol. 1543, American Institute of Physics Conference Series, ed. S. K. Chakrabarti, K. Acharyya, & A. Das, 49–63

Ricca, A., Bauschlicher, Jr., C. W., & Allamandola, L. J. 2011, ApJ, 729, 94

Russell, R. W., Soifer, B. T., & Willner, S. P. 1977, ApJ, 217, L149

Sakata, A., Wada, S., Tanabe, T., & Onaka, T. 1984, ApJ, 287, L51

Sakon, I., Onaka, T., Ishihara, D., Ootsubo, T., Yamamura, I., Tanabé, T., & Roellig, T. L. 2004, ApJ, 609, 203

Sellgren, K., Werner, M. W., & Dinerstein, H. L. 1983, ApJ, 271, L13

Sheehy, C., & Slosar, A. 2017, ArXiv e-prints

Shetty, R., Kauffmann, J., Schnee, S., Goodman, A. A., & Ercolano, B. 2009, ApJ, 696, 2234

Skrutskie, M. F., et al. 2006, AJ, 131, 1163

Sodroski, T. J., et al. 1994, ApJ, 428, 638

Soifer, B. T., Houck, J. R., & Harwit, M. 1971, ApJ, 168, L73

Takita, S., et al. 2015, PASJ, 67, 51

Thorwirth, S., Theulé, P., Gottlieb, C. A., McCarthy, M. C., & Thaddeus, P. 2007, ApJ, 662, 1309

Tibbs, C. T., et al. 2011, MNRAS, 418, 1889

Tielens, A. G. G. M. 2008, ARA&A, 46, 289

Tielens, A. G. G. M., & Allamandola, L. J. 1987, in Astrophysics and Space Science Library, Vol. 134, Interstellar Processes, ed. D. J. Hollenbach & H. A. Thronson, Jr., 397–469

Truemper, J. 1982, 2, 241

von Hausegger, S., & Liu, H. 2015, J. Cosmology Astropart. Phys., 8, 029

Weingartner, J. C., & Draine, B. T. 2001, ApJ, 548, 296

Werner, M. W., et al. 2004, ApJS, 154, 1

Wolstencroft, R. D., & Rose, L. J. 1967, ApJ, 147, 271

Wright, E. L., et al. 2010, AJ, 140, 1868

Young, E. T., et al. 2012, ApJ, 749, L17

Ysard, N., Juvela, M., & Verstraete, L. 2011, A&A, 535, A89

Ysard, N., Miville-Deschênes, M. A., & Verstraete, L. 2010, A&A, 509, L1

Ysard, N., & Verstraete, L. 2010, A&A, 509, A12

Yu, H.-G., & Nyman, G. 2012, ApJ, 751, 3

Zhang, Y., & Kwok, S. 2014, ArXiv e-prints

Zhou, Z., Sfeir, M. Y., Zhang, L., Hybertsen, M. S., Steigerwald, M., & Brus, L. 2006, ApJ, 638, L105

Acronyms

AME anomalous microwave emission. iii–vi, 4, 10–17, 20, 21, 23, 31–34, 36, 38–44, 48, 50–53, 59, 60, 63–66, 68–73, 75–84

BGs big grains. iii, 24

CBASS C-Band All Sky Survey. 84

CMB cosmic microwae background. 9

COBE Cosmic Background Explorer. 4, 6, 13

DIRBE Diffuse Infrared Background Experiment. 4, 6, 13, 21, 44, 48

ESA European Space Agency. 4

FIR far infrared. 3, 4, 13, 14, 60

FIS Far Infrared Surveyor. iv, 25, 45, 66

FTS Fourier Transform Spectrometer. 4

HB hierarchical Bayesian analysis. v, 17, 20, 52, 56, 60, 63

HEALPix Hierarchical Equal Area Iso Latitude Pixelation of the Sphere. 44, 45

Herschel Herschel Space Observatory. 4, 53

HFI High Frequency Instrument. 3, 66

IPAC Infrared Processing and Analysis Center. 44

IR infrared. 13, 66

IRAS Infrared Astronomical Satellite. 3, 4, 13, 16, 17, 21, 44, 66

IRC Infrared Camera. iii, 1, 3, 4, 10, 12, 20, 25, 44, 45, 66

IRTS Infrared Telescope in Space. 15

ISM interstellar medium. 3, 4, 6, 7, 9, 13, 15, 16, 21, 28, 53, 60, 83

ISRF interstellar radiation field. iv, 16, 52–54, 63

LFI Low Frequency Instrument. 41

LMC Large Megellanic Cloud. 53

LSM least-squares method. 19, 20, 52, 60, 63

MIR mid-infrared. v, 3, 60, 63, 68–73, 76, 78, 79, 82, 83

NASA National Aeronautics and Space Administration. 4, 44

PAH polycyclic aromatic hydrocarbon. i–vi, 5–7, 12–17, 20, 21, 24–31, 45, 50, 54, 57–60, 63, 64, 73, 77, 81–84

PC Planck Collaboration. 48, 65, 68, 79

S/N signal-to-noise ratio. v, 69, 70, 81, 82

SED spectral energy distribution. iii–v, 5, 7–9, 14, 15, 20, 22, 24, 28–30, 36, 38, 40, 48, 52–54, 56, 60, 63, 79, 83, 84

SST Spitzer Space Telescope. 4, 13

UIR unidentified Infrared bands. 60

VSGs very small grains. iii, 24

WISE Wide-field Infrared Survey Explorer. 17

WMAP Wilkinson Microwave Anisotropy Probe. 13, 14, 16